UNIVERSITY OF CALIFORNIA, IRVINE

Integration of a Solid Oxide Fuel Cell with an Organic Rankine Cycle and Absorption Chiller for Dynamic Generation of Power and Cooling for a Residential Application

THESIS

Submitted in partial satisfaction of the requirements for the degree of

MASTER OF SCIENCE

In Mechanical and Aerospace Engineering

By

Maryam Asghari

Thesis Committee:

Professor Jack Brouwer, Chair

Professor Scott Samuelsen

Professor Faryar Jabbari

DEDICATION

This work is dedicated to my parents, Masoumeh and Jafar, the reason for what I have become today. Thanks for all of your love and continued care. All these opportunities that I have today would have been impossible without your support. Thanks mom and dad for always believing in me and for encouraging me to strive for my dreams.

This work is also dedicated to my lovely husband, Alireza, who has offered unwavering support and encouragement throughout my academic journey. He has cheered me on when I was discouraged. I am so grateful to have you in my life.

TABLE OF CONTENTS

LIST OF FIGURES

LIST OF TABLES

ACKNOWLEDGMENTS

First, I would like to thank my advisor, Professor Jack Brouwer. Thanks for giving me the opportunity to join the lab and work under your supervision. I admire your great enthusiasm and leadership that continued to inspire me and guide me along the way. I also want to thank you for being not just an advisor but like a father, caring about wellbeing of your students. Thank you for all your supports.

My gratitude goes to Professor Scott Samuelsen who has been an inspiration to me through his example as a leader in alternative energy and his dedication to the field. Through his leadership, a very unique lab culture has cultivated at the National Fuel Cell Research Center.

Previous work by Dr. Dustin McLarty and Sarah Martz, was essential to me in understanding what needed to be done and for using the tools that would be so important for this work. Also, I would like to thank Alireza Saeedmanesh and Derek McVay to help me throughout this work.

Finally, I would like to acknowledge and thank my colleagues at the Advanced Power and Energy Program not only for collaboration in research but mostly for the friendship and positive experience that I have had over the past two years.

ABSTRACT OF THE THESIS

Integration of a Solid Oxide Fuel Cell with an Organic Rankine Cycle and Absorption Chiller for Dynamic Generation of Power and Cooling for a Residential Application

By

Maryam Asghari

Master of Science in Mechanical and Aerospace Engineering

University of California, Irvine, 2017

Professor Jacob Brouwer, Chair

The residential sector is responsible for 20% percent of total U.S. emissions. Emissions from the residential sectors can largely be traced to energy use in buildings. The demand for energy has been on a steady rise despite limited accessibility of non-renewable resources. Solid oxide fuel cells (SOFC) comprise an alternative technology which has high fuel to electricity efficiency, and can be powered by renewably sourced fuels. In this study, the waste heat from the fuel cell is captured and processed either through an Organic Rankine Cycle (ORC) to provide extra power or absorption chiller (AC) to provide cooling for meeting the power and cooling demand of a residence or community. A spatially resolved dynamic model was developed in Matlab/Simulink to study dynamic characteristics of an SOFC system based on a previous model developed at the National Fuel Cell Research Center. A dynamic model was developed for the ORC and AC in Matlab/Simulink to study the dynamic characteristics of the combined system. This model was then used to evaluate the performance of the system in terms of efficiency, capacity, and dispatchability, based upon measured load profiles of residential buildings. Dynamic data from a residential complex were used as an input to evaluate the dynamic system model. The SOFC was capable of following the highly dynamic load with an average electrical efficiency of 46%. Seven

present more power was produced through the ORC cycle with 10 % efficiency. The AC generated an average 125 kW of cooling with an average COP of 1.08.

1. INTRODUCTION

1.1. Overview

Resource availability and global warming are the two main concerns for the sustainability of energy conversion in the future. The demand for energy has been on a steady rise despite limited accessibility of non-renewable resources. For example, the world energy consumption is expected to increase by around 40% between 2006 and 2030 [1], while a remarkable increase in greenhouse gas emissions is also foreseen. For instance, from 1990 to 2007, the CO_2 equivalent emissions increased by 17% in USA [2]. Therefore, finding more efficient energy systems is becoming more vital than ever since the beginning of the industrial revolution. A high consumption of fossil fuels and environmental deterioration has drawn many researchers' attention to find more efficient methods of energy conversion, and reducing greenhouse gas emissions as well as pollutants [3]. Also, the recent downward trend in the price of natural gas in addition to legislation aimed at reducing greenhouse gas emissions have spurred increased interest in the development of distributed power generation schemes [4]. The efficiency of conventional power plants that are based on single conventional prime movers (e.g., combustion engines) is usually less than 39%. Thus, most of the fuel energy is converted to heat, which may not be utilized. Integrating subsystems into a conventional plant that captures and uses the exhaust heat for heating water, generating steam, or producing chilled water (referred to as CCHP for Combined, Cooling, Heat, and Power) could increase the plant efficiency to 80% [5][6].

Energy conversion systems in CCHP applications include internal combustion engines, external combustion engines (e.g., Stirling engines), steam turbines, gas turbines, micro-turbines and fuel cells. In other words, CCHP plants can be classified based upon the prime movers, heating

or cooling systems used, application type, or analysis type. However, what mainly distinguishes one CCHP plant from another is the prime mover of the plant. Wu and Wang [7] performed an extensive review of CCHP systems. This study shows that most CCHP systems use fossil fuel as the primary energy input.

Fuel cells and hybrid fuel cell systems have emerged as advanced thermodynamic systems with great promise in achieving high energy conversion efficiency with low environmental impacts. Pollutant and greenhouse gas (GHG) emissions are low to zero because they can convert the fuel's chemical energy directly into electricity without combustion. Fuel cell systems also have high energy conversion efficiency even at small distributed generation scales since energy conversion depends upon establishing a chemical potential difference rather than a temperature difference (e.g., combustion engines that are limited by the Carnot efficiency). There are five different types of fuel cells available in the market. Proton exchange membrane fuel cell (PEMFC) $(40-80℃)$, molten carbonate fuel cell (MCFC) $(650℃)$ and solid oxide fuel cell (SOFC) $(800-1000℃)$ are types of fuel cells that are targeted for commercialization in the residential (1–10kW), commercial (several MW) and power generation (25–250MW) end-use markets, system studies in this area are of great interest. Much research on fuel cells has focused on SOFC as an electrochemical reactor aimed at power and heat generation applications. SOFC is considered to be one of the most promising technologies for its high-efficiency and low emission compared with fossil power plants. SOFC is a highly efficient energy conversion device that transforms chemical energy to electrical energy and heat directly from fuels through electrochemical reactions at electrodes electrolyte interface. The fuel can be natural gas, carbon monoxide, methanol, ethanol and hydrocarbon compounds as well as hydrogen. The SOFC can be used with a variety of power generation systems; both stationary power generators and auxiliary

power sources in aircrafts or even in residential application. One cell consists of interconnected structures and a three-layered region composed of two ceramic electrodes (anode and cathode) separated by a dense ceramic electrolyte. SOFCs operate at high temperatures in range of $600-1000℃$. Oxygen ions formed at the cathode migrate through the ion-conducting electrolyte to the anode/electrolyte interface where they react with the fuel gases, producing water while releasing electrons that flow via an external circuit to the cathode/electrolyte interface. Unlike the low temperature polymer fuel cell, SOFC operates at temperatures high enough to enable the direct reformation of natural gas. Flexibility in fuel utilization is an advantage of SOFCs over other types of fuel cells. Hydrocarbon fuels can be supplied directly to SOFCs without the need for pre-reforming processing [8][9]. Large-scale, utility-based SOFC power generation systems have reached pilot-scale demonstration stages in the US, Europe, and in Japan. Small-scale SOFC systems are being developed for military, residential, industrial, and transportation applications [10]. There are several review papers involving the future aspects of power generation and challenges in the commercialization of SOFC system. A comprehensive study was carried out by Singhal [11] who investigated the advances in SOFC technology in the power generation sector. This study reviewed the material and fabrication methods used for the different cell components, and evaluated the performance of cells fabricated using these materials. Stambouli and Traversa [12] investigate the prospect of SOFC technology as an environmentally clean and efficient source of energy. Wachsman and Singhal [13] examined the commercialization, research and challenges of SOFC. Most of these review papers emphasize more on the research challenges for commercialization and development of SOFC technology. Very few papers have emphasized the research issues of the dynamic operation of SOFC CCHP technology for residential, marine, industrial, and transportation applications.

1.2. Goal

The goal of this study is to establish the performance characteristics of an integrated system of Organic Rankine Cycle with Solid Oxide Fuel Cell and absorption chiller for dynamic combined generation of power and cooling. Recovered SOFC exhaust heat is captured and used in the ORC as an energy source; therefore additional electrical power is obtained from ORC. Moreover, cooling is provided in this system using an absorption chiller. This combined, novel system is evaluated by the energetic performance in terms of efficiency and capacity. A dynamic model is developed and used to evaluate the performance of the system based upon measured load profiles of residential buildings.

1.3. Objectives

To meet the goal, the following objectives are achieved:

1. Develop a dynamic model for an Organic Rankine Cycle,
2. Verify the developed physical model of an ORC by comparing to literature data,
3. Build upon an existing dynamic Matlab/Simulink SOFC model to develop a dynamic system model that simulates the physical operation of the SOFC system,
4. Verify the developed physical models by comparison to experimental data.
5. Build upon an existing dynamic Matlab/Simulink Absorption Chiller model to develop a dynamic system model for integration with the SOFC model,
6. Simulate integrated system operation to meet the dynamics of actual buildings,
7. Determine and analyze steady state characteristics of the proposed system based upon targeted building demands, and
8. Evaluate the combined system efficiency, capacity, and dynamic operation.

2. BACKGROUND

2.1. Fuel Cell

Fuel cell devices are capable of converting fuel directly into electricity without the need of turbines or any major moving parts. The following section discusses how fuel cells work and some of the motivating principles behind their operation. Hydrogen is the most basic fuel used in the electrochemical reactions, but fuel cell systems can operate on a wide variety of fuels and they also require oxygen. The fuel and oxidant are separated by the membrane-electrode assembly. The membrane-electrode assembly is made up of anode and cathode electrodes and an electrolyte which is sandwiched between the two electrodes. The electrodes are permeable to gas so that the gases can make contact with the electrolyte. Points at which the gas, electrode, and electrolyte meet are points where an electrochemical reaction can occur which liberates an electron into or out of the electrode as an ion is transferred through the electrolyte. These points are called triple-phase boundaries (TPB). For example with hydrogen electrochemistry, the hydrogen splits, releasing two electrons into the anode while the hydrogen ions travel through the electrolyte. The ions then react with oxygen atoms and electrons in the cathode to form water. A voltage potential exists between the anode and cathode, this drives an electric current. The simplified reaction of the above combination of fuel and oxidant is as follows:

$$H_2 + \frac{1}{2}O_2 \rightarrow H_2O \tag{2-1}$$

Equation (2-1) is actually the overall reaction of the fuel cell and is made up of two half-reactions which occur at the anode and cathode TPBs.

Anode: $$H_2 \rightarrow 2H^+ + 2e^- \tag{2-2}$$

Cathode: $$\frac{1}{2}O_2 + 2H^+ + 2e^- \rightarrow H_2O \tag{2-3}$$

Equations (2-2) and (2-3) are the two half reactions which occur at the anode and cathode respectively. Fuel cells are often categorized by the type of electrolyte they have and their operating temperature. The various materials that are used to make up different electrolytes often require different electrochemical reactions to take place. However, the characteristics of these different fuel cells are governed by fundamental principles.

Analyzing from a thermodynamic point of view, the maximum work output obtained from the above reaction is related to the free-energy change of the reaction. The above reaction is spontaneous and thermodynamically favored because the free energy of the products is less than that of the reactants. The standard free energy change of the fuel cell reaction is indicated by the equation:

$$\Delta G = -nFE \tag{2-4}$$

Where ΔG is the free energy change, n is the number of moles of electrons involved, E is the reversible potential, and F is Faraday's constant. If the reactants and the products are in their standard states, the equation can be represented as

$$\Delta G_0 = -nFE_0 \tag{2-5}$$

The ideal performance of a fuel cell can be represented in different ways. The most commonly used practice is to define it by the Nernst potential represented as the cell voltage.

The Nernst equation is a representation of the relationship between the ideal standard potential "E_0" for the fuel cell reaction and the reversible potential "E" at other temperatures and pressures of reactants and products. Once the ideal potential at standard conditions is known, the ideal voltage can be determined at other temperatures and pressures through the use of these equations. According to the Nernst equation for hydrogen oxidation, the ideal cell potential at a given temperature can be increased by operating the cell at higher reactant pressures. Improvements in fuel cell performance have been observed at higher pressures and temperatures. The symbol E

represents the reversible potential, E_0 the standard potential, P the gas pressure, R the universal gas constant, F Faraday's constant and T the absolute temperature. Nernst voltage V_{Nernst} is defined:

$$V_{Nernst} = E_0 - \frac{RT}{zF} ln\left(\frac{\prod(a_{products})}{\prod(a_{reactants})}\right) \tag{2-6}$$

The minus sign is turned positive if the activity of the reactants and products are flipped in accordance with properties of logarithms. If water is assumed to be in the form of steam (vapor), the Nernst voltage for the equation (2.1) becomes

$$V_{Nernst} = E_0 - \frac{RT}{2F} ln\left(\frac{P_{H_2O}}{P_{H_2} P_{O_2}^{\frac{1}{2}}}\right) \tag{2-7}$$

The ideal and actual performance of a fuel cell is quite different, especially when one analyzes the potential current response of a fuel cell. Figure 2-1 displays the ideal and actual responses of a fuel cell. Electrical energy is obtained from a fuel cell when a current is drawn, but the actual cell potential is lowered from its equilibrium potential because of irreversible losses due to various reasons. Several factors contribute to the irreversible losses in a practical fuel cell. The losses, which are generally called polarization or over potential, originate primarily from activation polarization, ohmic polarization, and gas concentration polarization. These losses result in a cell potential for a fuel cell that is less than its ideal potential.

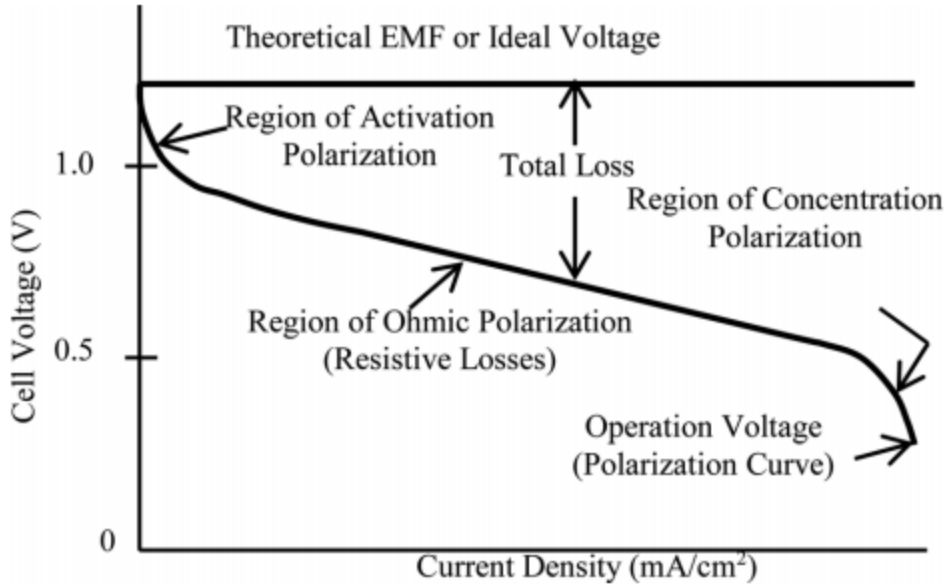

Figure 2-1: Ideal and Actual Voltage Current Density Curve of Fuel Cell [14]

The first of these three major polarizations is the activation loss, which is pronounced in the low current region. In this region electronic barriers must be overcome before the advent of current and ionic flow. The activation loss is directly proportional to the increase in current flow. The activation polarization can be represented as

$$\eta_{act} = \frac{RT}{\alpha nF} \ln\left(\frac{i}{i_0}\right) \tag{2-8}$$

Where η_{act} is the activation polarization, R the universal gas constant, T the temperature, α the charge transfer coefficient, n the number of electrons involved, F the Faraday constant, i the current density, and i_0 the exchange current density. Activation polarization is due to the slow electrochemical reactions at the electrode surface, where the species are oxidized or reduced in a fuel cell reaction. Activation polarization is directly related to the rate at which the fuel or the oxidant is oxidized or reduced. In the case of fuel cell reactions the activation barrier must be overcome by the reacting species.

The ohmic polarization varies proportionally to the increase in current and increases over the entire range of currents due to the constant nature of fuel cell resistance. The ohmic polarization can be represented as

$$\eta_{ohm} = iR_c \tag{2-9}$$

Where η_{ohm} is the ohmic polarization and R_c is the cell resistance.

The origin of ohmic polarization comes from the resistance to the flow of ions in the electrolyte and flow of electrons through the electrodes and the external by decreasing the electrode separation, enhancing the ionic conductivity of the electrolyte and by modification of the electrolyte properties.

The concentration losses occur over the entire range of current density, but these losses become prominent at high limiting currents where it becomes difficult for gas reactant flow to reach the fuel cell reaction sites. The concentration polarization can be represented as

$$\eta_{con} = \left(\frac{RT}{nF}\right) \ln\left(1 - \frac{i}{i_L}\right) \tag{2-10}$$

Where η_{con} is the concentration polarization, i_L is the limiting current density. As the reactant gas is consumed at the electrode through the electrochemical reaction, there will be a potential drop due to the drop in the initial concentration of the bulk of the fluid in the surroundings. This leads to the formation of a concentration gradient in the system. Several processes are responsible for the formation of the concentration polarization. These are (1) slow diffusion of the gas phase in the electrode pores, (2) solution of reactants into the electrolyte, (3) dissolution of products out of the system, and (4) diffusion of reactants and products, from the reaction sites, through the electrolyte. At practical current densities there is slow transport of reactants to the electrochemical reaction and slow removal of products from the reaction site, which is a major contributor to the concentration polarization.

2.2. Organic Rankine Cycle

The Rankine Cycle was named after William J. M. Rankine, a Scottish engineer and physicist who developed the theory of the steam engine in 1859. The steam production process for heating has been around for thousands of years, and in the 17th and 18th century, the development of the steam power cycle began. These developments lead to the steam engine and the Industrial Revolution, which vastly changed human life. A large amount of ORC power plants have been built, mainly for waste heat recovery and combined heat and power applications. This technology has some advantages over the traditional steam Rankine cycle, which makes it more profitable for power plants with a limited electrical output power, despite a lower efficiency. The optimization of the ORC is quite different from the traditional steam cycle, mainly because of the heat source temperature limitation, and also because there is usually no constraint regarding the vapor quality at the end of the expansion.

The Organic Rankine Cycle (ORC) is similar to a steam cycle, except that it uses an organic working fluid in place of water. This organic compound is typically a refrigerant, a hydrocarbon, a silicon oil, or a perfluorocarbon. Its boiling point is lower than water, which allows recovering heat at a lower temperature than in the traditional steam Rankine cycle. Organic Rankine Cycles have been studied both theoretically and experimentally with reported efficiencies usually below 10% for small-scale systems [15].

Organic Rankine Cycles have often been applied to relatively low temperature heat recovery processes that convert thermal energy into mechanical power. The process begins with an organic working fluid that is pumped through an evaporator, exposing it to a heat source. The heat then converts the fluid into a superheated vapor due to its low boiling point. The hot vapor is then expanded to produce electric power. The warm vapor exits the expander and enters the condenser,

which is then cooled back into a liquid. The cold liquid goes through the evaporator to repeat the closed-loop cycle to be reused or recycled. Figure 2-2 explains this process.

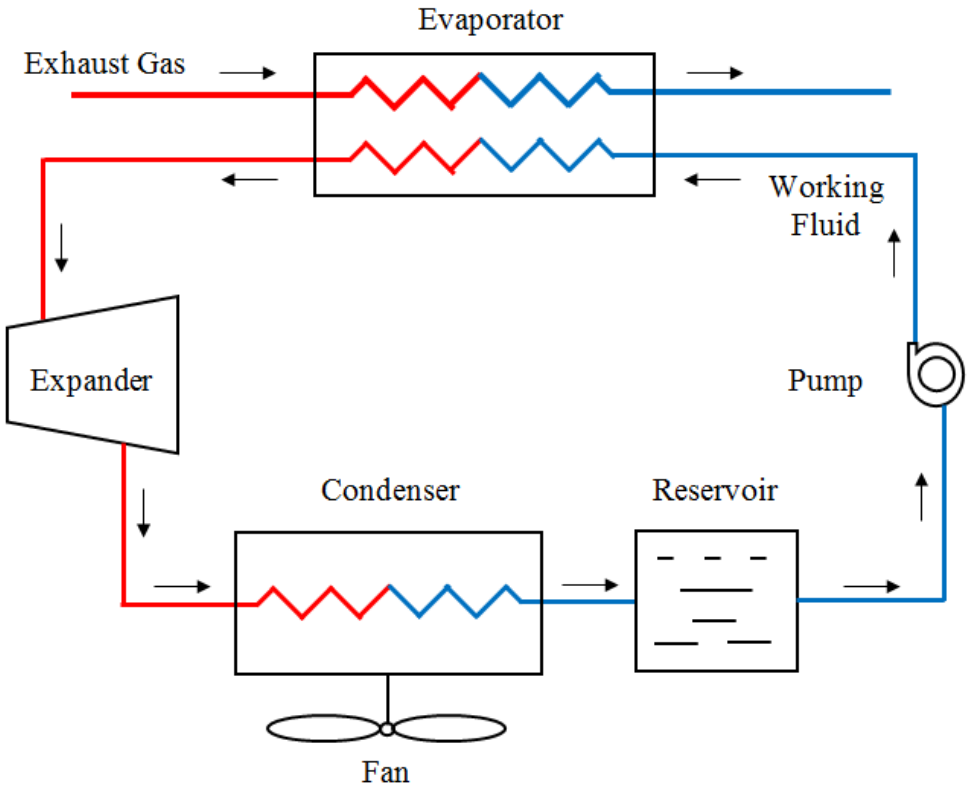

Figure 2-2: Schematic View of the ORC

Organic Rankine Cycle units are comprised of an expander, a pump, a condenser and an evaporator. The core of the ORC unit is the expander, where a hot vapor expands and spins the expander-generator, producing electricity. The pump, or working fluid pump, constantly regulates the working fluid based on heat source conditions to optimize system performance and generate maximum power. The evaporator uses a heat source to convert the working fluid into vapor form. From there the condenser cools vapor back to liquid form to continue the ORC cycle.

2.2.1. ORC Applications

2.2.1.1. Biomass Combined Heat and Power (CHP)

Biomass is widely available from several industrial and agricultural processes such as furniture industry or agricultural and forest residues. Biomass has great potential in providing combined

heat and power (CHP) simultaneously. Biomass can be transformed into heat using combustion and the heat can be converted to electricity using the ORC. Such systems have received growing attention especially for systems with low power capacity [16].

2.2.1.2. Solar Power Cycles

Solar energy is one of the most promising renewables as it is non-exhaustible, pollution-free and exploitable in most parts of the world. The intensity of sunlight reaching the earth is 1360W/m^2. Energy from the sun can be utilized in electricity generation directly (through PV cells) or indirectly (solar thermal). Solar thermal power generation using concentrating collectors is a mature technology. Collectors capture the sun radiation and concentrate it on either a focal line or focal point depending on the type of the collector. This radiant heat is used to heat up the heat transfer fluid that passes through the collectors. ORC is a reliable technology for utilizing such heat especially if it is generated as low to medium grade heat (80-350^{o}C) in small-scale systems for electricity generation

2.2.1.3. Geothermal Binary Power Cycles

The geothermal energy (earth's heat) that is naturally embedded in the deep layers of the earth is a renewable form of energy. This energy can be exploited by drilling deep wells and transferring the hot brine trapped in the sub-layers to the surface via the production well. Depending on the geographical location the brine temperature varies. However, the average geothermal gradient near the Earth's surface is about 300K/km [16]. The hot brine can transfer its heat to an organic fluid in the evaporator of an ORC system and then return to the injection well at a lower temperature. Geothermal heat sources are available over a broad range of temperatures, from 60°C up to 300°C [16]. The lower bound for power generation is about 80°C:

2.2.1.4. Internal Combustion Engines (ICE) Waste Heat Recovery

On average, two thirds of the fuel energy consumed by an ICE is wasted through the exhaust gases and the cooling liquid [16] . This waste heat from the engine (mainly from exhaust gas and cooling circuit) is large enough to allow efficient heat recovery with the ORC technology. The electricity generated from the on-board ORC can be used for supplying auxiliary units such as the air conditioning or recharging the batteries. One of the main issues with on-board ORC in ICEs is the typically highly dynamic operating behavior of the system which requires complex controlling schemes in order to maintain acceptable efficiency and performance levels in the ORC.

2.2.1.5. Gas and Steam Power Cycle Exhaust Heat Recovery

It is a common practice in large-scale power plants to recover the exhaust heat from gas turbines in a Brayton cycle to produce steam for driving steam Rankine cycle system. Usually the exhaust gas from the gas turbine is in the range of 500–600^{o}C which makes the steam Rankine cycle a more attractive option for waste heat recovery. However, with emergence of micro-gas turbines as remote power units and with power capacity of less than 500 kW and exhaust temperature of less than 400^{o}C, significant attention has been paid to the waste heat recovery of micro-gas turbines with ORC for small-scale applications in order to increase the overall efficiency.

2.2.1.6. High Temperature Fuel Cell

Although SOFC systems exhibit high electrical efficiency, in practical applications almost half of the fuel energy is converted to heat. The exhaust gas temperature of high temperature fuel cells which is usually less than 400^{o}C makes organic Rankine cycle an attractive candidate to be used as a bottoming cycle for an SOFC system.

2.3. Absorption Chiller

Chillers are machines that take energy from a low temperature reservoir and reject it to a higher temperature reservoir. Absorption chillers enable the usage of the exhaust heat for generating a cooling capacity which can be exported for local cooling or used within the system to improve efficiency.

The more common type of cooling, known as direct expansion or vapor compression cooling, relies on a compressor which is often driven by an electric motor. This compressor compresses a refrigerant vapor, raising its temperature and pressure before it goes into a condenser where it rejects heat into the environment. The fluid is then expanded through an expansion valve which lowers its boiling point; it is then passed into an evaporator where it vaporizes. The heat required for vaporization of the fluid results in a drop in temperature in the refrigerant which provides a usable cooling effect. The fluid then passes to the compressor and the cycle beings anew. A diagram for a vapor compression cycle is shown in Figure 2-3.

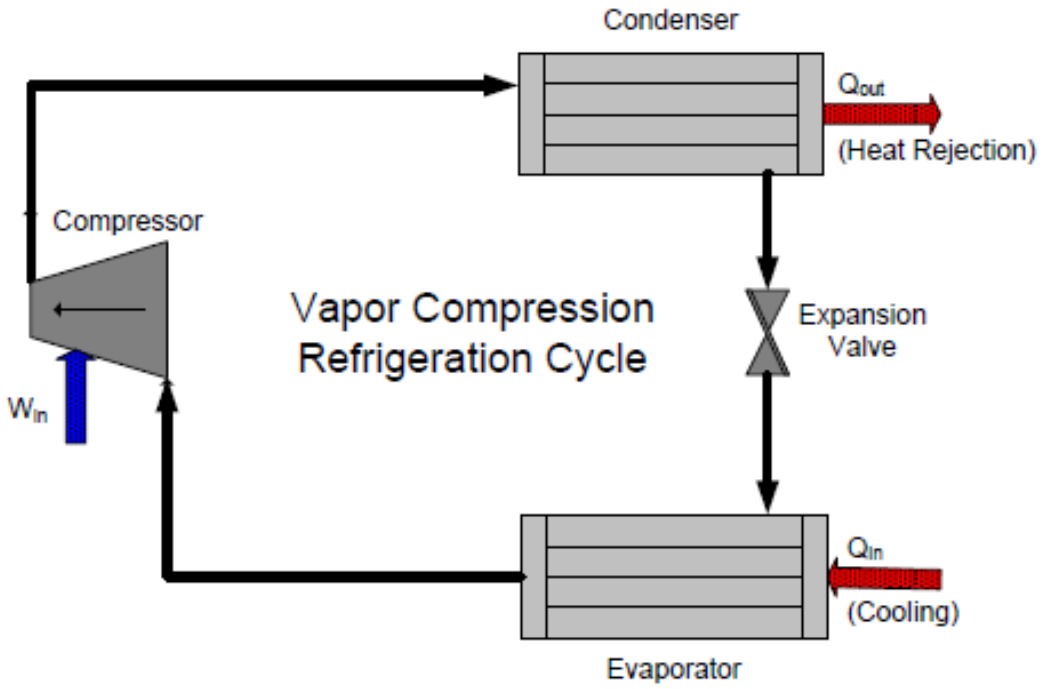

Figure 2-3: Vapor Compression Cycle [17]

In an absorption refrigeration cycle, the concept is of course the same, but it is achieved in a slightly different process. An absorption chiller uses an absorbent-refrigerant pair as its working fluid. For example, a Lithium Bromide-Water absorption chiller uses Lithium Bromide as the absorbent and water as the refrigerant. Alternatively, a Water-Ammonia absorption chiller uses water as the absorbent and Ammonia as the refrigerant. To move from the vapor compression cycle, to the absorption refrigeration cycle, the compressor is removed and replaced with a generator vessel, shown in Figure 2-4. The generator vessel, like the compressor, is where the main energy input takes place, but instead of mechanical compression, thermal energy is added in the generator. This energy boils the solution in the generator, and the refrigerant evaporates from the solution, leaving the solution more highly concentrated. While the evaporated refrigerant flows to the condenser section and proceeds much like in the vapor compression cycle, the concentrated solution flows in a separate path. Depending upon the cycle configuration, this solution is typically

used in a solution heat exchanger to preheat the dilute solution being pumped from the absorber. After this heat exchange, the concentrated solution flows to the low-pressure absorber. The absorber is cooled by the same cooling circuit as the condenser. This allows the concentrated solution to absorb the refrigerant entering from the evaporator, as its low saturation concentration limit (% wt. LiBr) is determined by temperature and pressure. The two fluids recombine, and are pumped back to the generator vessel to begin the cycle again. The cycle described here is a single-effect absorption refrigeration cycle, whereas there do exist double-and triple-effect absorption chillers as well. The single-, double-, triple- refer to the number of generator vessels used to produce refrigerant, and as this number goes up, so does the coefficient of performance (and complexity) of the chiller. Single-effect machines are popular to use for smaller applications, and double-effect chillers are very common for larger-scale refrigeration or industrial applications. Triple effect machines are less common and are still in the development phase.

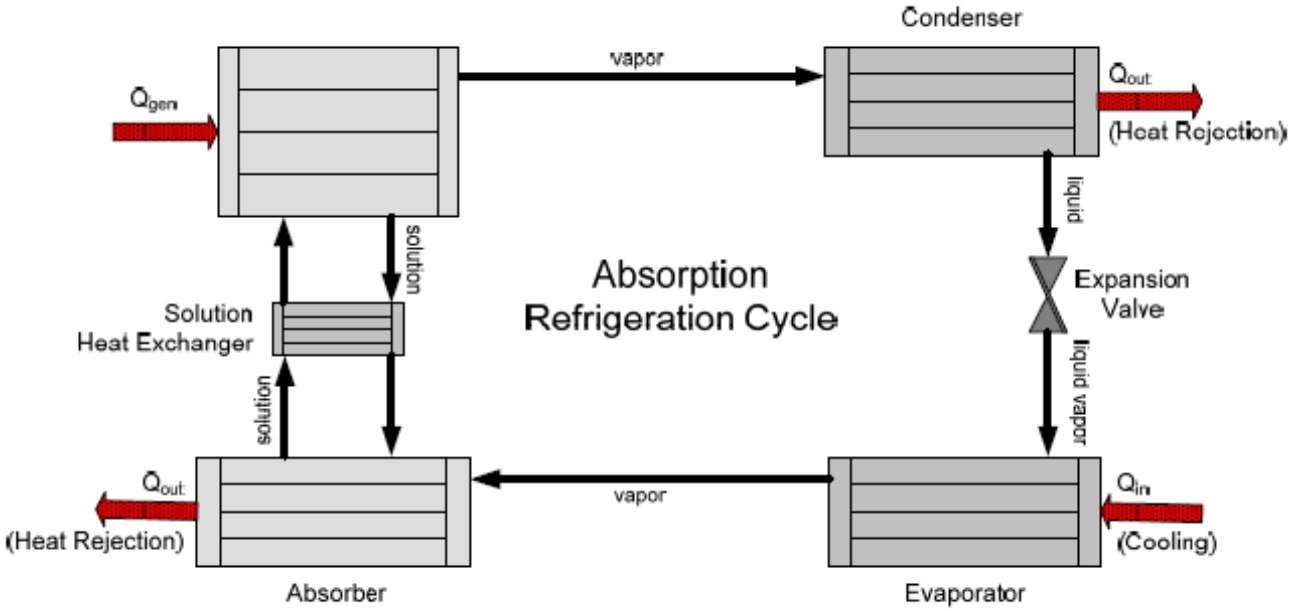

Figure 2-4: Absorption Refrigeration Cycle[17]

2.4. Previous Studies

SOFC usually operate at high temperature about $600 - 1000℃$, which temperature range is well-suited to integrating bottoming cycles for additional power, heating or cooling production which results in improved overall efficiency when compared to an individual stand-alone system. An analysis of a hybrid system of micro-turbine and fuel cell as a prime mover of CCHP plants was carried out by Saito et al. [18]. Saito et al. [18] carried out energy demand and consumption analyses of apartments, offices and hotels in Japan with the use of the hybrid system. They found that the annual fuel consumption dropped by 32%, 36% and 42% for the apartments, offices and hotels, respectively. One general method to recover the waste heat from the SOFC is the SOFC-GT system, in which SOFC is coupled with a gas turbine (GT) as the bottom cycle to increase the overall efficiency by recovering waste heat from SOFC exhaust. The concept of SOFC-GT hybrid system was proposed for decades, and many researchers have studied the theoretical analysis of this hybrid system [19][25]. Siemens-Westinghouse Power Corporation developed the first hybrid power system, which integrated an SOFC stack with a gas turbine engine. The pressurized (3 atm) system generated 220kW of electrical power at a net electrical efficiency of 53.5% [26]. Mueller et al. [27] designed a theoretical solid oxide fuel cell-gas turbine hybrid system using a 60kW micro-gas turbine. Although using a gas turbine can recover waste heat from an SOFC, the exhaust gas from the gas turbine still has relatively high temperature that could be used in other bottoming cycles. If the waste heat from gas turbine can also be recovered by some method, then the energy conversion efficiency can increase further.

Another method to recover the waste heat from the SOFC is the SOFC-ORC combined system. Using ORC as a bottoming cycle of the SOFC, the system can fully recover the waste heat from the SOFC. Some research has been conducted on the waste heat recovery of the exhaust from the SOFC by ORC. Akkaya and Sahin [28] presented an energetic analysis for a combined power

generation system consisting of an SOFC and an ORC. The results showed that the efficiency was increased by about 14-25% by recovering SOFC waste heat through ORC based on investigated design parameter conditions. And there existed an optimum value of fuel utilization factor maximizing the efficiency. Al-Sulaiman et al. [29] proposed a cooling, heating and power production system based on the SOFC and ORC. The energy analysis showed that at least a 22% gain in efficiency was achieved compared with the stand-alone SOFC system. Ghirardo et al. [30] conducted a study on heat recovery for a 250kW SOFC onboard a ship. Using ORC could produce 35kW of electricity from the waste heat of 181 kW. The overall efficiency increased from 44% to 49% and the cost of energy dropped from 0.25$/kWh to 0.22$/kWh. In another study, Al-Sulaiman et al. [31] analyzed CO_2 emissions from the CCHP system. The study showed that the CO_2 emissions per MWh are significantly less than that of the CO_2 emissions per MWh of the electricity produced by the SOFC alone or the net electrical power of the system. In another study, Al-Sulaiman et al. [32] studied the feasibility of using a CCHP plant based on ORC and solid oxide fuel cells. In their study, it was shown that there is 3–25% gain on exergy efficiency when compared with the power cycle only. In a different study, Al-Sulaiman et al. [33] examined a CCHP system using a biomass combustor and an ORC. In their study, it was shown that the exergy efficiency of the CCHP system increases significantly to 27% as compared with the exergy efficiency of the electrical power case, which is around 11%. In [34] the performances of a 100kW SOFC-ORC system coupled with a gasification facility was carried out by means of a multi-objective optimization. Their results show that efficiencies in the range of 54-56% can be achieved by wisely selecting the organic fluid properties. In [35], Al-Sulaiman et al. compared performance of three different CCHP systems based on SOFC, Biomass, and Solar using organic Rankine

cycles. This study shows that the SOFC CCHP system has the highest electrical efficiency among the three systems.

In SOFC-ORC combined systems, it is a novel idea to use the ORC waste heat for cooling purposes. Several studies were conducted in using absorption chiller as a bottoming cycle of the SOFC for cooling. Margalef and Samuelsen [36] studied an integrated molten carbonate fuel cell and absorption chiller cogeneration system, showing that the overall electrical and cooling efficiency can achieve 71.7%. Furthermore, Silveira et al. [37] [38] examined a molten carbonate fuel cell cogeneration system integrated with absorption refrigeration which was applied to a dairy for electricity and cold water production. The results showed that the electrical efficiency of the system and the second law efficiency of the fuel cell unit were 49% and 46%, respectively. Elmer et al. [39] used empirical SOFC and liquid desiccant component data and provided an energetic, economic, and environmental performance analysis assessment of the combined system. The economic and environmental analysis showed an improvement in SOFC capital cost and the transition to clean hydrogen production. Leong [40] analyzed an integrated solid oxide fuel cell with an adsorption chiller. A steady state mathematical model was developed to simulate the effects of different SOFC operating conditions on an energy system incorporating SOFC and exhaust gas driven absorption chiller. The effect of fuel utilization factor on electrical, cooling, and total efficiency was investigated [41]. Zink [42] studied an integrated solid oxide fuel cell absorption heating and cooling system for buildings, concluding that the combined system demonstrated great advantages in both technical and environmental aspects. An integrated SOFC and a double effect water/Lithium Bromide absorption chiller were presented by Yu et al. [43]. The system performance was analyzed under different fuel utilization ratio, fuel flow ratio, and air inlet temperature. However, there is currently only one study in the literature about using SOFC

integrated with both ORC and absorption chiller [29]. In this study, the waste heat from the ORC is used to produce cooling using a single-effect absorption chiller.

In addition to producing power, cooling, and/or heat from the capture and use of exhaust energy, a third product (hydrogen) can also be generation use a high-temperature fuel cell [44]. So called “Tri-Generation” systems. In [45], Becker et al. focused on the design and performance estimation of a methane-fueled, 1MW SOFC Tri-Generation system operating at steady-state. Another study focused on design and exergetic analysis of a novel carbon free Tri-Generation system for hydrogen, power and heat production from natural gas, based on combined solid oxide fuel and electrolyzer cells [46]. SOFC has the capability of converting methane into hydrogen by external reforming and/or within the anode compartment through internal steam methane reformation and water-gas shift reactions [47]. Heat and water produced by the fuel cell electrochemical reactions are used directly in the endothermic fuel processing reactions.

2.5. Summary

In the literature, most of the papers investigated the challenges related to the commercialization and development of SOFC technology combined with bottoming cycles in steady state operating condition. Very few papers have emphasized the research issues of the dynamic operation of SOFC CCHP technology for residential, marine, industrial, and transportation applications. The residential sector is responsible for 20% percent of total U.S. emissions. Emissions from the residential sectors can largely be traced to energy use in buildings. Also, load profiles of residential building are highly dynamic during the day. As a result, it is essential to capture the performance of the combined system based upon measured load profiles of residential buildings. In the literature, there is a lack of study on dynamic operation of SOFC integrated with ORC and AC for residential application.

The novelty of this study is developing a dynamic model for integrated SOFC-ORC-AC which enables capturing the behaviour of the combined system during the real dynamic operating conditions. In this research, power load of a residential complex is used as an input of SOFC model to address the feasibility of designing an SOFC system which follows the real residential dynamic loads. The mass flow rate and temperature of SOFC exhaust gas are changed as a result of following the dynamic residential load. In this study to address the effects of dynamic heat source for the bottoming cycles (ORC-AC), a dynamic model is developed for both ORC and AC cycles. This study shows the possibility of designing an integrated SOFC-ORC-AC system to not only following the residential dynamic demand, but also using SOFC dynamic waste heat to produce extra power or cooling for residential buildings.

3. APPROACH

This work begins by reviewing the relevant literature on solid oxide fuel cells, organic Rankine cycles and absorption chillers. Chapter two presents a brief summary of previous and concurrent research efforts. Information from the literature and previous efforts at the National Fuel Cell Research Center (NFCRC) aided in developing working models of relevant system components using dynamical simulation software. The Matlab-Simulink environment was chosen to develop these models for its versatility and widespread adoption in the engineering community. In chapter three, the configuration of organic Rankine cycle is characterized. Also, the dynamic formulation for each ORC component model in derived and the organic Rankine cycle model is developed. A brief summary of fuel cell model and absorption chiller model is presented in chapter three.

In chapter four, first the SOFC model is verified with two commercially available SOFC from solid power. Then, the ORC model is verified based on the literature. Once the models behavior approximated a realistic system, the load profile and usage data gathered from a target building were used to evaluate the performance characteristic of the system. First, the steady state characteristics of the system are presented. Then, the dynamic behavior of the combined system is presented. In the chapter five, the conclusions and recommendations of the research are presented.

The tasks for the study map to the objectives, namely:

Task 1. Develop a dynamic model for an Organic Rankine Cycle:

The basic configuration of ORC is characterized during this task. Also, all the dynamic formulations modelling physical behaviour of each component are derived. A state space method is defined. The dynamic model of each component based on formulation is developed in Matlab software.

Task 2. Verify the developed physical model of an ORC by comparing to literature data:

In order to verify the developed dynamic model, the dynamic input data consist of mass flow rate and temperature of heat source of a former study in literature are used. Two different scenarios for mass flow rate and temperature of heat source are considered to verify the developed dynamic model of the ORC in this study.

Task 3. Build upon an existing dynamic Matlab/Simulink SOFC model to develop a dynamic system model:

A spatially and temporally resolved dynamic model is developed in MATLAB/Simulink based upon the National Fuel Cell Research Center (NFCRC) SOFC model to simulate the dynamic operating characteristics of an SOFC system. The model, derives from first principles, incorporates the physics for SOFC simulations. The system is sized based on the load profile of target residential building.

Task 4. Verify the developed physical model of SOFC by comparison to experimental data:

Two different commercially available SOFC systems were used to verify the developed model. The first one is the 1.5kWe BlueGEN, a commercially available SOFC CHP system, designed for small- to medium-scale building applications. The second SOFC system used for model verification is the EnGen 2500 mCHP (micro-Combined Heat and Power) unit designed for residential use or small-scale commercial applications. Input parameters of the developed model are adjusted based upon the operating conditions of these two systems. In order to verify the developed model, the model V-j characteristic curve is compared with BlueGen and EnGen V-j characteristic curves.

Task 5. Build upon an existing dynamic Matlab/Simulink Absorption Chiller model to develop a dynamic system model for integration with the SOFC model:

The developed dynamic absorption chiller model is based upon a previous work in NFCRC. In this model, the absorption chiller is sized based upon SOFC exhaust capacity used as a heat source in generator.

Task 6: Simulate integrated system operation to meet the dynamics of actual buildings:

Measured dynamic power demand data from a residential complex (Verano Place, VP) located in Irvine California are used as an input to evaluate the dynamic operation of the integrated SOFC-ORC model. Data from EnergiStream Live Demand Dashboard for a work day and a weekend day are used for simulations in this study. The model is run using the residential load profile for 24 hours with 15-minute resolution.

Task 7: Determine and analyze steady state characteristics of the proposed system based upon targeted building demands:

The integrated system is sized for a 400kW SOFC and a 25kW ORC. A sensitivity analysis is done to investigate the effects of fuel utilization (FU) on SOFC power output, SOFC efficiency, SOFC exhaust gas temperature and mass flow rate, ORC power and overall efficiency.

Task 8: Evaluate the combined system efficiency, capacity, and dynamic operation:

The developed dynamic model for SOFC-ORC-AC is used to investigate the dynamic behavior of the integrated system e.g., SOFC efficiency, ORC output power, SOFC and ORC exhaust gas temperatures and mass flow rates, the ORC condenser and evaporator operating pressures and temperatures, AC cooling capacity and COP.

4. METHODOLOGY

4.1. Solid Oxide Fuel Cell Dynamic Model

4.1.1. Overview

SOFCs are promising technology for electricity generation with high efficiency, potential for low degradation characteristics, mechanical simplicity, and scalable manufacturing capability. This section will discuss dynamic modeling of SOFC which is the main driver for the entire system model. With fuel continuously supplied to the anode, and an oxidant, such as air, supplied to the cathode the zirconium oxide electrolyte will allow oxygen ions to pass through the crystal lattice by jumping from one lattice vacancy to the next. This transport mechanism allows for the flow of ions from cathode to the anode compartments while an electric current is drawn. The SOFC system contained the fuel cell stack, anode off-gas oxidizer, fuel and air preheat heat exchangers, cathode mixing, and blower control for the incoming air stream. The modeling platform used for this work is Matlab Simulink. McLarty et al. previously developed a spatially resolved fuel cell model upon which this work is based [48]-[49].

4.1.2. Matlab Simulink

Simulink is a graphical programming environment for modeling, simulating and analyzing multi-domain dynamic systems. The general layout of a Simulink model provides a strong visual representation of what is actually being modeled by organizing system components into individual blocks that contain the governing equations. Each block has its certain input and output parameters which are then connected to the other blocks present in the system. Simulink offers tight integration with the rest of the MATLAB environment and can either drive MATLAB or be scripted from it to allow a wide range of modeling capabilities and flexibility that are desirable for complex system models

Ability to use different forms of solvers such as fixed time step or variable time step solvers is another advantage of Simulink modeling. This ability is very important for simulating the dynamics of the system and temporally resolving a full system model with numerous components and numerous characteristic time scales. The ability to use vectors and matrices for variables in Simulink, provides the opportunity to spatially resolve each component of the system by breaking it up into several nodes. This can be applied to any system component to provide a deeper understanding of the phenomena that are being captured by the model.

4.1.3. Modeling Development

A spatially and temporally resolved dynamic model was developed in MATLAB/Simulink based upon the National Fuel Cell Research Center (NFCRC) SOFC model to simulate the dynamic operating characteristics of an SOFC system [49]. The model, derived from first principles, incorporates the physics for SOFC simulations. The organization of the model follows a vector format to obtain spatial resolution while temporal resolution is obtained by the use of kinetic modeling, thermal gradients, and control systems to converge components to steady state. This method allows for a wide variety of capabilities to investigate the dynamics of a system and the performance and effects of system components. This modeling approach takes advantage of the ability to model dynamics of the system until it is able to converge to steady state. Simulation of any spatial resolution is performed by determining the number of rows and columns during the model initialization. The spatially and temporally resolved SOFC model divides the surface of a fuel cell into various nodes. For each node, temperature, species concentrations, pressure, voltage, current density and flow rate are evaluated with dynamic conservation of mass, energy and momentum equations. The model takes into account the interconnect, cathode, anode, and

electrolyte structure as four separate, but bulk control volumes of each node resulting in a quasi-3-D representation of a fuel cell.

Dynamic modeling is able to introduce control schemes for flow rates, blower powers, recirculation, etc. that mirrors how a real system must be operated. It also has the ability to capture the kinetic behavior of chemical reactions to determine species compositions and the extents of reaction. These factors play an important role in the overall design aspects of the system and its components because now the properties of materials, thicknesses of piping, sizes of heat exchangers, flow directions, temperature gradients, etc. all make a difference for creating a system model that physically resembles a real world system. The main physical and chemical phenomena modeled in the system are: energy balances (consideration of energy for all flows throughout the system), mass balances (accounts for all flows present in the system), heat transfer (convective heat transfer for flows through components and conductive heat transfer through plates and membranes in multiple directions), fluid dynamics (friction factor calculations for pressure losses and flow rates), chemical reaction kinetics (captures chemical and electrochemical reactions for kinetic behavior and extent of reaction) and fuel cell potential and losses (Nernst potential with activation, concentration, and ohmic losses for fuel cell operation).

4.1.4. SOFC Model

In an SOFC, completely or partially reformed fuel (reformate) typically flows through the anode compartment while air flows through the cathode compartment. Species diffuse in and out of the porous electrodes to the triple phase boundaries (TPB) at the interface of gas, electrode and electrolyte phases. Electrochemical reactions convert the O_2 from the cathode electrode to oxygen ions ($O^{=}$) which travel through the electrolyte and then participate in electrochemical reactions at fuel electrode TPBs to produce CO_2 and water by reacting with H_2, CO, and CH_4. Electrons are

produced by the fuel electrode electrochemical reactions and consumed by the oxygen electrode electrochemical reactions and travel from the fuel electrode to the oxygen electrode through the external circuit to generate power. The polarizations result in a voltage that is lower than the thermodynamic voltage. The SOFC model is capable of producing voltage-current density (V-j) curves which are used for comparison purposes of fuel cell performance. The V-j curves depend upon the Nernst and overvoltage equations which themselves are functions of various operating parameters. The Nernst equation yields the highest achievable voltage of the SOFC Eq. (4-1). In a SOFC reaction the only reactant species involved in transport across the electrolyte interface is oxygen. Due to the highly reactive and diffusive nature of hydrogen, the losses occurring at the anode electrode will be negligible in respect to the cathode over potentials. Thus, the focus will remain on the losses occurring at the reducing electrode. The actual voltage achieved Eq. (4-2) takes into account the Nernst potential and losses defined below.

$$V_{Nernst} = E^0 + \frac{RT}{2F} ln\left(\frac{X_{H_2} X_{O_2}^{\frac{1}{2}}}{X_{H_2O}} P_{Cathode}^{\frac{1}{2}}\right) \tag{4-1}$$

$$V_{FC} = V_{Nernst} - \eta_{act} - \eta_{ohmic} - \eta_{conc} \tag{4-2}$$

$$\eta_{cath} = \frac{RT}{4F} ln\left[\frac{j}{j_0 * P_C \left\{x_{O_2|d} - \frac{t^C jRT}{4FP_C D_{O_2,N_2}^{eff}}\right\}}\right] \tag{4-3}$$

$$\eta_{Ohmic} = \frac{i}{A_{cell}} * ASR_{eff} = j * \frac{t_m}{\sigma} = \frac{t_m T}{Ae^{-\Delta G_{act}/(RT)}} \tag{4-4}$$

Where V is voltage, E_0 is standard potential, R is universal gas constant, T is temperature, F is Faraday constant, P_i is partial pressure of species i normalized by atmospheric pressure and X_i is mole fraction of species i. η is over potential. In Eq. (4-3) j is current density; j_0 is exchange current

density of the electrode, t^c is the cathode thickness, D^{eff} is effective binary diffusivity, t_m in thickness of electrolyte, σ is electrolyte conductivity and ΔG_{act} is the activation barrier for the diffusion process.

The model used in this study incorporates the following expressions to account for electrochemistry, conservation of mass and energy, species concentrations, and heat and mass transfer for each node. For the species conservation, a dynamic conservation equation Eq. (4-5), applies to each node. The species conservation depends on parameters such as chemical and electrochemical reaction rates, and inlet and outlet flow concentrations.

$$\frac{dX_i}{dt} = \frac{R_{REF} + R_{CONSUMED} + \left(\dot{N}X\right)_{in} + \left(\dot{N}X\right)_{out}}{\frac{P_j V_j}{RT_j}} \tag{4-5}$$

Where X_i is concentration of species i, R_{REF} is molar production rate of steam methane reformation reaction and $R_{CONSUMED}$ is species consumption by the electrochemical reactions. One of the important SOFC system performance parameter is electrical efficiency which is defined as ratio of electrical output power of the SOFC system to the lower heating value of fuel Eq. (3-6).

$$\eta_{SOFC} = \frac{\dot{W}_{Electric,net}}{\dot{N}_{fuel}.LHV_{fuel}} \tag{4-6}$$

Where $\dot{W}_{Electric,net}$ is net electric power output of the SOFC, $\dot{N}_{fuel}$ is molar flow rate of consumed fuel and LHV_{fuel} is lower heating value of fuel. The details of the polarization effects and detailed information of the fuel cell dynamic model are discussed by McLarty et al. [49].

4.1.5. System Model

Additional energy system components such as heat exchangers, a mixing chamber, reformers, oxidizer and blower are modeled and integrated with the SOFC model to form a complete integrated energy system model. Simultaneous solutions of the dynamic equations that govern

each of the components captures the complex and coupled interactions amongst system components.

The heat exchanger model uses different states consist of temperature of hot flow, temperature of cold flow and temperature of steel plates at each node as well as pressure of hot flow and cold flow at stack inlet to capture the thermal inertia (time constant) in heat transfer process [49]. The heat exchanger model evaluates these states at each time and calculates effectiveness of heat exchanger at that time. For nodes at stream sides, energy balance includes convective heat transferred between fluid and steel plate, while for nodes at steel plate it includes convective heat transfer as well as conduction between solid nodes.

For the blower in this study, the governing equation is the state space representation of the blower rotational velocity obtained from rate of change of energy (balanced with net power in) [49].

To thermally manage the SOFC stack, a portion of air at cathode outlet is recirculated and mixed with fresh air as shown in Figure 4-1. The mixing volume model is used to model mixing of species. This model uses some states e.g., outlet temperature, species concentration and inlet pressure to capture the behavior of gas mixture at dynamic operating conditions.

An example system configuration is presented in Figure 4-1. Pre-reformed fuel comes into the fuel preheater, and then is preheated with a portion of the oxidizer outlet to match the inlet temperature of the stack. The stream then enters the SOFC stack, where it will be further reformed internally and reacted electrochemically. The operating voltage, power, and exhaust species are computed in the stack. The anode exhaust is then sent to the gas oxidizer. The exhaust of the oxidizer is used to preheat the incoming air and fuel. The air feed is preheated by the oxidizer exhaust to the inlet temperature of the SOFC and sent to the cathode electrode of SOFC. The

cathode exhaust is then sent to the gas oxidizer. The initial system schematic can be seen in Figure 4-1.

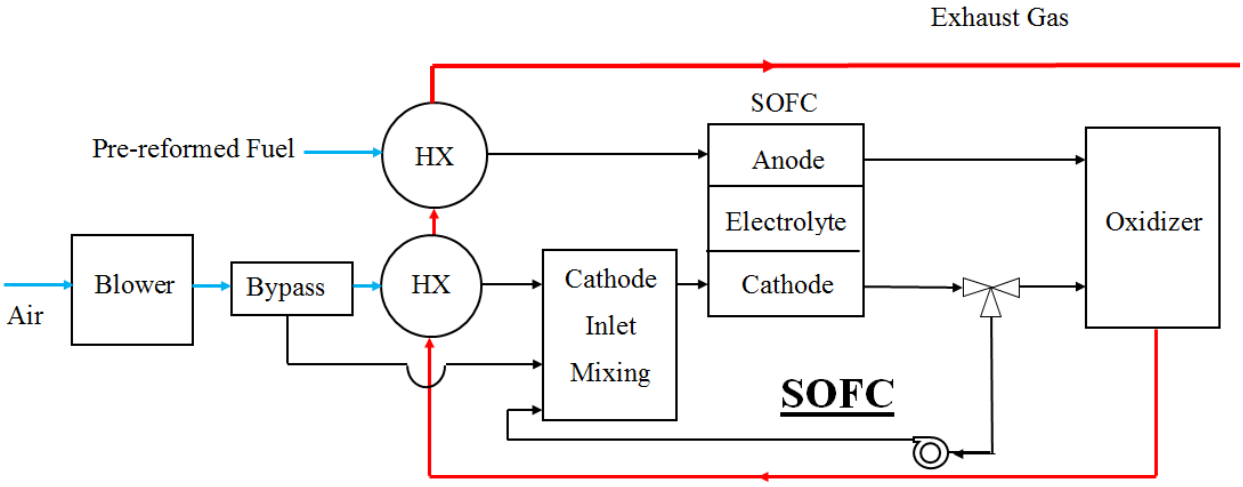

Figure 4-1: Example Configuration of the SOFC System

4.2. Organic Rankine Cycle Dynamic Model Development

4.2.1. Overview

Simulating ORC cycles requires a numerical solver in which the equations of mass and energy balance, heat transfer, pressure drops, mechanical losses, leakages, etc. are implemented. ORC models present in the literature can be subdivided into two main types: steady-state and dynamic. Steady-state models are required for design (or sizing) purpose, for part-load simulation, system performance evaluation, or cycle optimization problems. Dynamic models, on the other hand, also account for energy and mass accumulation in the different components. This kind of model is necessary when transient phenomena such as start-up or shut-down, dynamic control or variable heat sources are studied.

This section describes the development of a dynamic model of each component of a waste heat recovery ORC. Each component (e.g., evaporator) of the ORC has its own dynamic behavior that determines the input-output response. This output itself can be an input of another component. This way a connection between two components is created and considering all subsystems and

their connections an overall model of an ORC system is obtained. The models are implemented using “MATLAB” and the fluid properties are computed using the ‘‘REFPROP’’ library. The ORC cycle model is built by interconnecting the sub-models of the different components: Heat exchangers, Pump and Expander. Taking the dynamics of all components into account would yield a rather complex system model. Since the physics and chemistry of the components occur with various characteristic time scales it is possible to create a dynamic model where fast processes are assumed to be in equilibrium, while the physics and chemistry of the slower processes are captured dynamically. The proposed dynamic model focuses on dynamics of the heat exchangers; the dynamics of the other components are much faster (smaller time constants) and can be assumed to be continuously in equilibrium states. These models are used to investigate, through simulations, the performance of the system and to point out some achievable improvements.

4.2.2. Organic Rankine Cycle

The schematic diagram of the ORC based waste heat recovery system is shown in Figure 4-2. The basic components of an ORC system consist of an evaporator, an expander, a condenser and a working fluid pump.

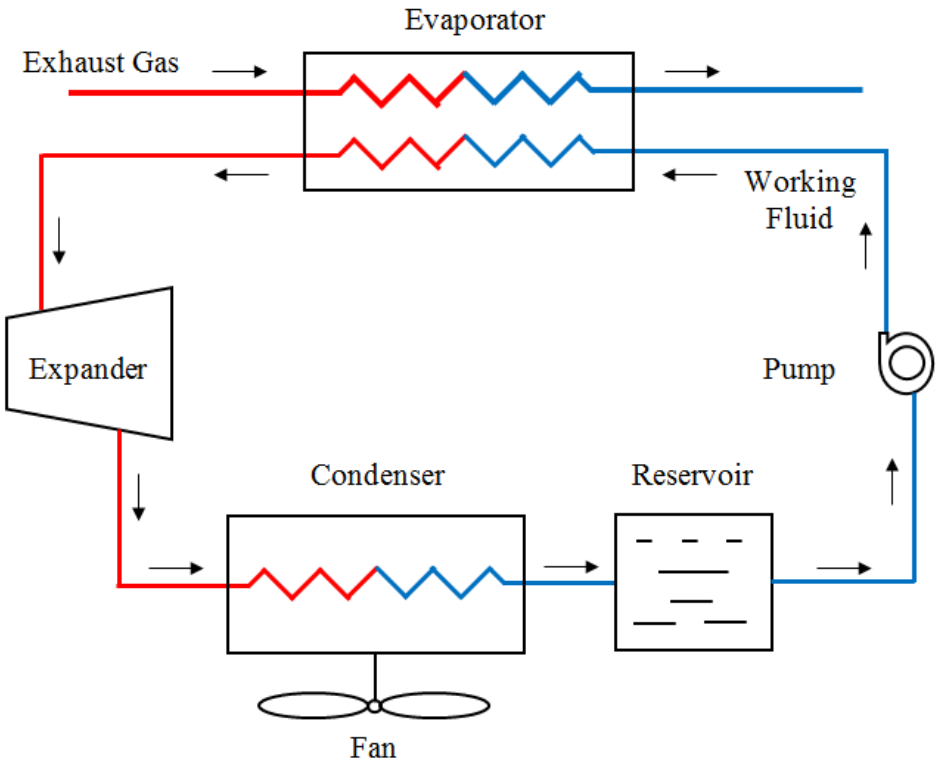

Figure 4-2: Schematic view of the ORC

R245fa, which critical properties are listed in Table 4-1, is selected as the working fluid in the current ORC system. The waste heat coming from exhaust gas of the SOFC exchanges heat with the working fluid R245fa in the evaporator, in which R245fa is vaporized at constant pressure until it becomes superheated vapor. The superheated working fluid drives the expander, and accordingly electric power is generated. The vapor from the expander is then condensed into liquid state in the air-cooled condenser and collected in the receiver. The liquid is pressurized by the pump and sent back to the evaporator. The waste heat source is always variable in temperature and flow rate. The oil-free scroll expander in this ORC is the component for converting heat into mechanical energy which can achieve better performance under low speed and variable working conditions than a constant speed expander [15].

Table 4-1: Critical Properties of R245fa.

Molecular Formula	$CF_3CH_2CHF_2$
Molecular Weight	$134.05 g/mol$
Critical Pressure	$3640 kPa$
Critical Temperature	$427.20 K$
Critical Density	$517 kg/m^3$

4.2.3. Evaporator Modeling

Evaporator is the most critical part of the ORC to capture in a dynamic model. The thermal efficiency and heat recovery of the ORC is connected to the performance and parameters of the heat exchanger used in the system. The dynamics of the evaporator are caused by the thermal inertia of the metal components and the fluid, as well as the mass inertia of the liquid phase. In the proposed model, evaporator is a cross flow shell and tube heat exchanger used in the ORC circuit which is shown in Figure 4-3. The model uses the SOFC system exhaust as the hot fluid and refrigerant (R245fa) as a cold fluid. Corresponding inputs of the evaporator model are: mass flow rate and temperature of the SOFC exhaust and refrigerant.

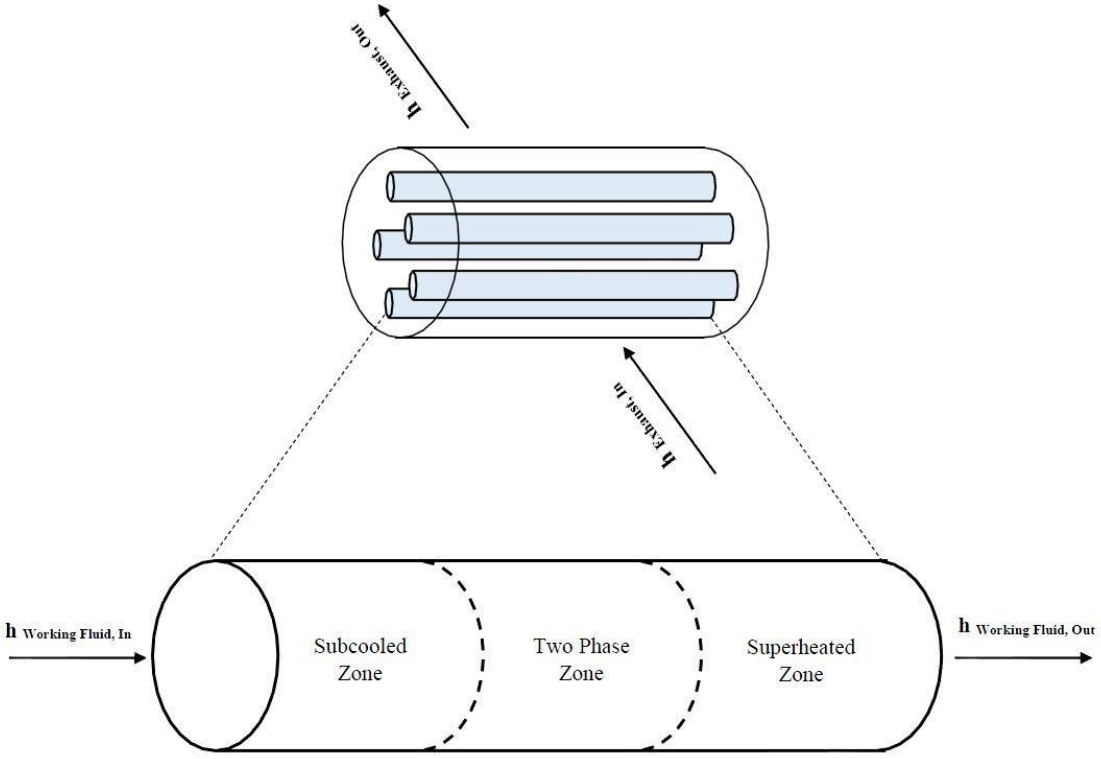

Figure 4-3: Overview of the Evaporator Model

Relevant phenomena to be modeled occurring in such heat exchangers, include the heat transfer (convective) from the hot (shell) side to the cold (tube) side, energy accumulation in the metal parts of the exchanger, and mass and energy accumulation on both fluid sides of the exchanger (e.g., SOFC exhaust and R245fa).

Figure 4-4 shows how the temperature of the working fluid typically changes when it flows through the evaporator, indicating important points: The evaporator outlet temperature (T_{out}), the saturation temperature (T_{sat}) and the difference between these two temperatures is the superheating temperature difference (ΔT_{su}).

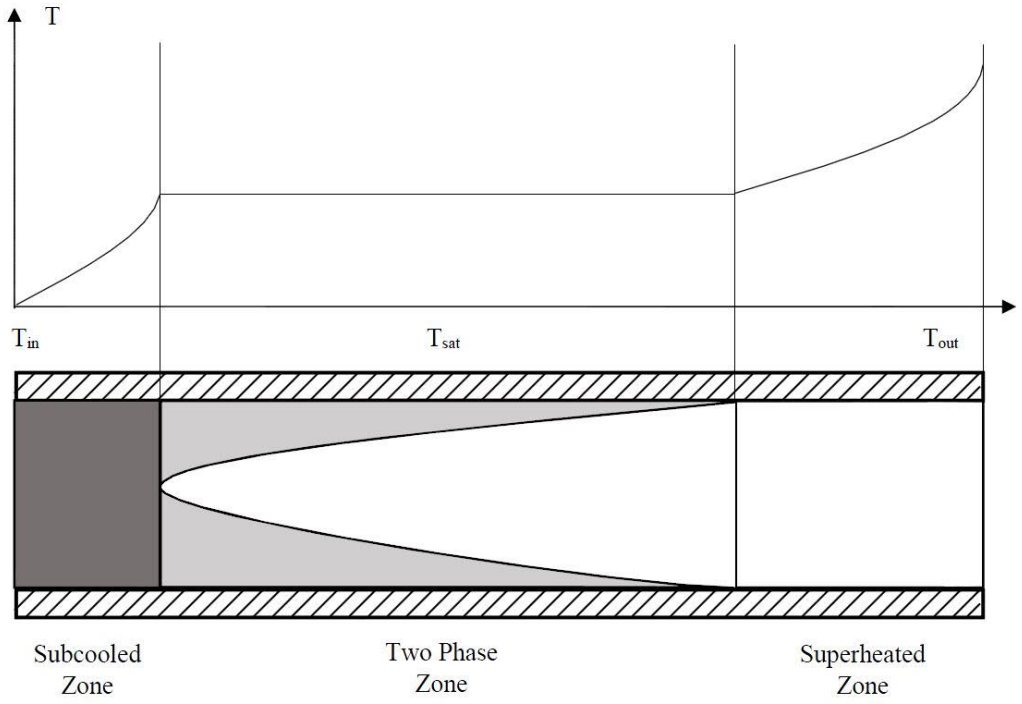

Figure 4-4: Temperature Profile of the Fluid through the Evaporator

The approach that is used in this research to model the evaporator is a lumped parameter approach in which both the inside and outside of the wall are considered uniform in temperature and composition (lumped). One control volume is considered for the all regions in working fluid side. To simplify the model, several assumptions about the working fluid flow are used as follows:

1. The evaporator is assumed to be a long, thin, horizontal tube.
2. The working fluid is mixed adequately and the working fluid flowing through the evaporator tube can be modeled as a bulk fluid flow.
3. Axial heat conduction in the working fluid as well as in the pipe wall is negligible.
4. The pressure drop along the evaporator tube, caused by momentum change in the working fluid and viscous friction, is negligible. Therefore, fluid pressure can be assumed uniform along the entire evaporator. Thus the equation for conservation of momentum is not needed.

Using the assumption of negligible pressure loss, the pressure is constant along the pipe, but is still time dependent.

In this study, dynamic model used for evaporator and condenser is based on an approach developed by Rasmussen et al. [50].

4.2.3.1. Governing Equations

4.2.3.1.1. Mass Conservation at Working Fluid Side:

The general differential mass balance is:

$$\frac{\partial \rho}{\partial t} + \nabla . (\rho \vec{v}) = 0 \tag{4-7}$$

$$\dot{m} = \rho A_{cs} v \tag{4-8}$$

In Eq. (4-7) and (4-8) ρ is the working fluid density, $\vec{v}$ is the working fluid velocity and A_{cs} is the cross sectional area of a tube in which working fluid flows.

By multiplying A_{cs} in to Eq. (4-7) and considering Eq. (4-8), Eq. (4-9) can be obtained as follows:

$$\frac{\partial (\rho A_{cs})}{\partial t} + \frac{\partial (\dot{m})}{\partial z} = 0 \tag{4-9}$$

Integrating from $z = 0$ to $z = L_e$ (evaporator tube length), which correspond to the inlet and outlet boundaries, respectively:

$$\int_0^{L_e} \frac{\partial (\rho A_{cs})}{\partial t} dz + \int_0^{L_e} \frac{\partial (\dot{m})}{\partial z} dz = 0 \tag{4-10}$$

Assuming a constant cross sectional area and applying the Leibniz rule to the first term (see Appendix A) results in Eq. (4-11).

$$A_{cs} \frac{d}{dt} \int_0^{L_e} \rho \, dz + (\dot{m}_{out} - \dot{m}_{in}) = 0 \tag{4-11}$$

In Eq. (4-11) the first term on the left hand side describes the rate of working fluid mass change. The second and third terms are the mass flows through the outlet and inlet boundaries, respectively.

Assuming an average density for working fluid and integrating the first term results in:

$$A_{cs}\frac{d}{dt}(\bar{\rho}L_e) + (\dot{m}_{out} - \dot{m}_{in}) = 0 \rightarrow$$
$$A_{cs}\dot{\bar{\rho}}L_e + (\dot{m}_{out} - \dot{m}_{in}) = 0 \quad (4\text{-}12)$$

The thermodynamic properties are calculated from (p, h) in the present analysis, where h is the average enthalpy. The choice of *p* as one of the state variables is obvious, due to the assumption of no pressure loss. Temperature and pressure cannot be selected as independent variables because in two phase flow they are dependent upon each other. The second variable should be either internal energy or enthalpy. Since this problem involves steady flow across boundaries (control volume approach), enthalpy (*h*) is selected so that pressure and enthalpy (p, h) define each state [50]. The average enthalpy $\bar{h}$ is defined as:

$$\bar{h} = \frac{(h_{in} + h_{out})}{2} \quad (4\text{-}13)$$

In Eq. (4-13) h_{in} and h_{out} are working fluid inlet and outlet enthalpy respectively.

The working fluid mean density is approximated by $\bar{\rho} = \rho(P, \bar{h})$ and the working fluid mean temperature is calculated from the same states as $\bar{T}_r = T(P, \bar{h})$ [50].

In Eq. (4-12), $\frac{d\bar{\rho}}{dt}$ is calculated using the chain rule:

$$A_{cs}L_e\left[\left(\frac{\partial\bar{\rho}}{\partial P}\Big|_{\bar{h}}\right)\frac{dP}{dt} + \left(\frac{\partial\bar{\rho}}{\partial\bar{h}}\Big|_{P}\right)\frac{d\bar{h}}{dt}\right] + (\dot{m}_{out} - \dot{m}_{in}) = 0 \rightarrow$$
$$\left[A_{cs}L_e\left(\frac{\partial\bar{\rho}}{\partial P}\Big|_{\bar{h}}\right)\right]\dot{\bar{P}} + \left[A_{cs}L_e\left(\frac{\partial\bar{\rho}}{\partial\bar{h}}\Big|_{P}\right)\right]\dot{\bar{h}} + (\dot{m}_{out} - \dot{m}_{in}) = 0 \quad (4\text{-}14)$$

4.2.3.1.2. Energy Conservation Equation at Working Fluid Side

The general differential energy balance can be obtained as follows:

$$\frac{\partial(\rho A_{cs}h - A_{cs}P)}{\partial t} + \frac{\partial(\dot{m}h)}{\partial z} = p_i\alpha_i(T_w - \bar{T}_r) \tag{4-15}$$

In Eq. (4-15) p_i is the inner cross sectional perimeter of a tube in which working fluid flows, α_i is convection heat transfer coefficient between working fluid and tube and T_w is the evaporator's tube wall temperature.

Integrating from $z = 0$ to $z = L_e$ (evaporator tube length):

$$\int_0^{L_e} \frac{\partial(\rho A_{cs}h)}{\partial t}dz - \int_0^{L_e} \frac{\partial(A_{cs}P)}{\partial t}dz + \int_0^{L_e} \frac{\partial(\dot{m}h)}{\partial z}dz = \int_0^{L_e} p_i\alpha_i(T_w - \bar{T}_r)dz \tag{4-16}$$

Applying Leibniz's rule (see Appendix A) on the first term of Eq. (4-16) and integrating other terms based on a constant cross sectional area and a constant heat transfer coefficient along the tube [50]:

$$\begin{aligned} &A_{cs}\left[\frac{d}{dt}\int_0^{L_e}\rho h dz\right] - A_{cs}\int_0^{L_e}\frac{\partial(P)}{\partial t}dz + \int_0^{L_e}\frac{\partial(\dot{m}h)}{\partial z}dz = \int_0^{L_e} p_i\alpha_i(T_w - \bar{T}_r)dz \rightarrow \\ &A_{cs}\left[\frac{d}{dt}\int_0^{L_e}\rho h dz\right] - A_{cs}L_e\dot{P} + (\dot{m}_{out}h_{out} - \dot{m}_{in}h_{in}) = L_e p_i\alpha_i(T_w - \bar{T}_r) \end{aligned} \tag{4-17}$$

In Eq. (4-17), the first term is the rate of change of enthalpy in the control volume, the second term is a consequence of using enthalpy and not internal energy in the first term. The third and fourth terms account for the convective enthalpy through the boundaries, and the last term is the heat flow from the wall.

Assuming that working fluid mean enthalpy is $\bar{h} = \frac{(h_{in}+h_{out})}{2}$, working fluid mean density is $\bar{\rho} = \rho(P, \bar{h})$ and working fluid mean temperature is $\bar{T_r} = T(P, \bar{h})$ and integrating the first term of Eq. (4-17), it can be obtained [50]:

$$A_{cs}L_e\left[\frac{d}{dt}(\bar{\rho}\bar{h}L)\right]-A_{cs}L_e\dot{P}+(\dot{m}_{out}h_{out}-\dot{m}_{in}h_{in})=L_ep_i\alpha_i(T_w-\bar{T}_r)\rightarrow$$

$$A_{cs}L_e\left[\dot{\bar{\rho}}\bar{h}+\dot{\bar{h}}\bar{\rho}\right]-A_{cs}L_e\dot{P}+(\dot{m}_{out}h_{out}-\dot{m}_{in}h_{in})=L_ep_i\alpha_i(T_w-\bar{T}_r)\rightarrow$$

$$A_{cs}L_e\left[\left[\left(\frac{\partial\bar{\rho}}{\partial P}\Big|_{\bar{h}}\right)\frac{dP}{dt}+\left(\frac{\partial\bar{\rho}}{\partial\bar{h}}\Big|_{P}\right)\frac{d\bar{h}}{dt}\right]\bar{h}+\dot{\bar{h}}\bar{\rho}\right]-A_{cs}L_e\dot{P}+(\dot{m}_{out}h_{out}-\dot{m}_{in}h_{in})$$

$$=L_ep_i\alpha_i(T_w-\bar{T}_r)\rightarrow \tag{4-18}$$

$$A_{cs}L_e\left[\left[\left(\frac{\partial\bar{\rho}}{\partial P}\Big|_{\bar{h}}\right)\dot{P}+\left(\frac{\partial\bar{\rho}}{\partial\bar{h}}\Big|_{P}\right)\dot{\bar{h}}\right]\bar{h}+\dot{\bar{h}}\bar{\rho}\right]-A_{cs}L_e\dot{P}+(\dot{m}_{out}h_{out}-\dot{m}_{in}h_{in})$$

$$=L_ep_i\alpha_i(T_w-\bar{T}_r)\rightarrow$$

$$A_{cs}L_e\left[\left(\frac{\partial\bar{\rho}}{\partial P}\Big|_{\bar{h}}\right)\bar{h}-1\right]\dot{P}+A_{cs}L_e\left[\left(\frac{\partial\bar{\rho}}{\partial\bar{h}}\Big|_{P}\right)\bar{h}+\bar{\rho}\right]\dot{\bar{h}}+(\dot{m}_{out}h_{out}-\dot{m}_{in}h_{in})=$$

$$L_ep_i\alpha_i(T_w-\bar{T}_r)$$

4.2.3.1.3. Energy Conservation at the Wall

The energy balance for the wall region is derived using a control volume analysis similar to the energy balance analysis for the flow region. A simplified differential energy balance for the wall is given in Eq. (4-19):

$$C_{p_w}\rho_wA_w\frac{\partial T_w}{\partial t}=p_i\alpha_i(\bar{T}_r-T_w)+p_o\alpha_o(\bar{T}_g-T_w) \tag{4-19}$$

In Eq. (4-19), C_{p_w} is specific heat capacity of tube wall, ρ_w is density of tube wall, A_w is the annulus cross sectional area of tube wall, p_o is the outer cross sectional perimeter of a tube in which working fluid flows and α_o is convection heat transfer coefficient between SOFC exhaust gas and tube wall.

Assuming $\bar{T}_g=T_{g_{in}}(\mu)+T_{g_{out}}(1-\mu)$ where μ is weighting factor, and integrating from $z=0$ to $z=L_e$ (evaporator tube length) [50]:

$$\int_0^{L_e} C_{p_w}\rho_w A_w \frac{\partial T_w}{\partial t}\,dz = \int_0^{L_e} p_i\alpha_i(\bar{T}_r - T_w)dz + \int_0^{L_e} p_o\alpha_o\left(\bar{T}_g - T_w\right)dz \rightarrow$$

$$C_{p_w}\rho_w A_w L_e \frac{\partial T_w}{\partial t} = L_e p_i\alpha_i(\bar{T}_r - T_w) + L_e p_o\alpha_o(\bar{T}_g - T_w) \rightarrow \quad (4\text{-}20)$$

$$C_{p_w}\rho_w A_w \frac{\partial T_w}{\partial t} = p_i\alpha_i(\bar{T}_r - T_w) + p_o\alpha_o(\bar{T}_g - T_w)$$

In Eq. (4-20), the left hand side term accounts for the rate of change in internal energy. The right hand side terms account for the heat transfer from the inside and the outside of the wall.

4.2.3.1.4. Energy Conservation Equation for SOFC Exhaust Gas Side

Based on the same assumptions for working fluid inside the tube, the model of the SOFC exhaust gas is simplified by assuming constant pressure along the tube.

General differential energy balance is [50]:

$$\frac{\partial(\rho_g A_g h_g - A_g P_g)}{\partial t} + \frac{\partial(\dot{m}_g h_g)}{\partial z} = p_o\alpha_o(T_w - \bar{T}_g) \quad (4\text{-}21)$$

In Eq. (4-21), ρ_g is SOFC exhaust gas density, A_g is the cross sectional area in which the SOFC exhaust gas is located inside the evaporator shell, h_g is mean enthalpy of exhaust gas, P_g is pressure of exhaust gas and $\dot{m}_g$ is mass flow rate of exhaust gas.

Integrating from $z = 0$ to $z = L_e$ (evaporator tube length):

$$\int_0^{L_e} \frac{\partial(\rho_g A_g h_g)}{\partial t}\,dz - \int_0^{L_e} \frac{\partial(A_g P_g)}{\partial t}\,dz + \int_0^{L_e} \frac{\partial(\dot{m}_g h)}{\partial z}\,dz = \int_0^{L_e} p_o\alpha_o(T_w - \bar{T}_g)dz$$

$$\rightarrow$$

$$A_g\rho_g\left[\frac{d}{dt}\int_0^{L_e} h dz\right] + \dot{m}_g\left(h_{g,out} - h_{g,in}\right) = L_e p_o\alpha_o(T_w - \bar{T}_g) \rightarrow \quad (4\text{-}22)$$

$$A_g L_e\rho_g C_{p,g}\frac{d\bar{T}_g}{dt} = L_e p_o\alpha_o\left(T_w - \bar{T}_g\right) + \dot{m}_g\left(h_{g,in} - h_{g,out}\right) \rightarrow$$

$$A_g L_e \rho_g C_{p,g} \frac{d\bar{T}_g}{dt} = L_e p_o \alpha_o (T_w - \bar{T}_g) + \dot{m}_g C_{p,g} \left(T_{g_{in}} - T_{g_{out}}\right)$$

In Eq. (4-22), $C_{p,g}$ is specific heat capacity of SOFC exhaust gas.

4.2.3.2. Heat transfer Coefficient for the Working Fluid side in the Evaporator

In this study, as it was mentioned, the bulk model is used to model the working fluid inside the evaporator. Thus, working fluid flows inside the evaporator has a uniform state along the tube. For the single phase region, Gnielinski's correlation is applied to calculate the working fluid Nusselt number, and for two phase region, heat transfer coefficient is calculated by Wang-Touber's correlation [51].

In single phase flow, equation (4-23) is used to calculate working fluid Nusselt number.

$$f = (0.79\, ln(Re) - 1.64)^{-2}$$

$$Nu = \begin{cases} \dfrac{\left(\frac{f}{8}\right)(Re - 1000)Pr}{1 + 12.7\left(\frac{f}{8}\right)^{0.5}(Pr^{\frac{2}{3}} - 1)} & Re > 2300 \\ 4.36 & Re < 2300 \end{cases} \quad (4\text{-}23)$$

In two phase flow, equation (4-24) is used to calculate working fluid heat transfer coefficient.

$$\alpha_{tp} = \begin{cases} \alpha_{ww} & 0 \le x \le 0.85 \\ \alpha_{ww}|_{x=0.85} - \left(\dfrac{x - 0.85}{0.15}\right)^2 \left(\alpha_{ww}|_{x=0.85} - \alpha_{v,all}\right) & 0.85 < x \le 1 \end{cases} \quad (4\text{-}24)$$

$$\alpha_{ww} = 3.4 \left(\frac{1}{X_{tt}}\right)^{0.45} \alpha_{l,all}$$

In equation (4-24), X_{tt} is Lockhart-Martinelli number which defines as:

$$X_{tt}^2 = \left(\frac{1 - x}{x}\right)^{1.75} \left(\frac{\nu_l}{\nu_v}\right)\left(\frac{\mu_l}{\mu_v}\right) \quad (4\text{-}25)$$

Where $\nu_l$and ν_v are specific volumes for saturated liquid and saturated vapor, respectively. μ_l and μ_v are dynamic viscosity for saturated liquid and saturated vapor, respectively. *x* is vapor mass

quality. $\alpha_{l,all}$ is heat exchange coefficient off working fluid in a case that all the working fluid is liquid and $\alpha_{v,all}$ is heat exchange coefficient off working fluid in a case that all the working fluid is vapor.

4.2.3.3. Boundary conditions

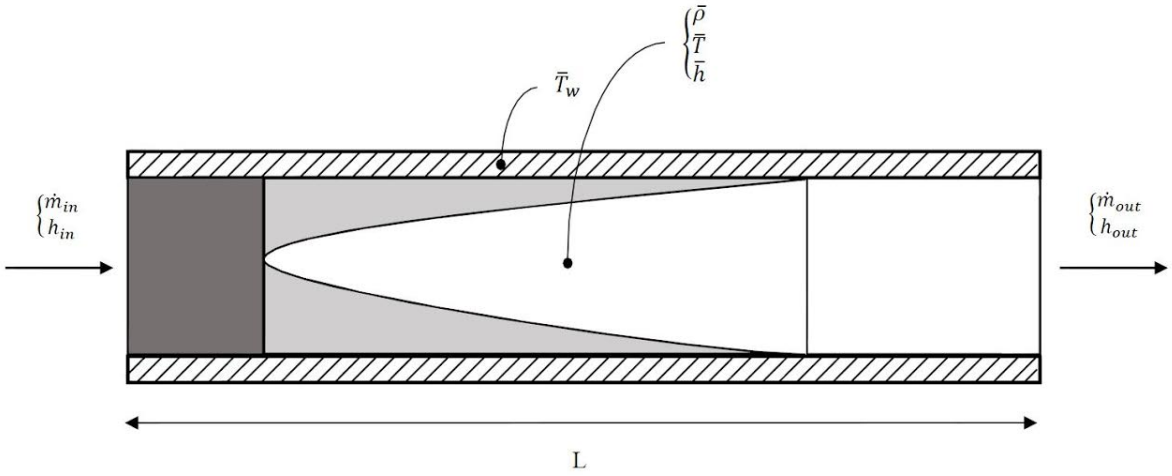

Figure 4-5: Schematic of the Bulk Model for Evaporator

Figure 4-5 shows a schematic of the general bulk model. Liquid is entering with mass flow rate $\dot{m}_{in}$ and enthalpy (h_{in}). In a system model, both of these terms are usually calculated in adjacent models (pump) and are considered as known boundary conditions. Mass flow is leaving the evaporator at a rate ($\dot{m}_{out}$), which is also usually calculated in a succeeding model (expander) and is considered as a known boundary condition for this model. The boundary conditions correspond to a design case, which may be changed as required. The evaporator is heated by the SOFC exhaust gas. The other terms shown on the schematic are calculated in the model and are thus results of the model. The design inputs and outputs are shown on Figure 4-6, where dependent variables are those, which can be calculated from other output variables. The term "design" reflects that inputs and outputs may be changed depending on the boundary conditions for a given simulation task.

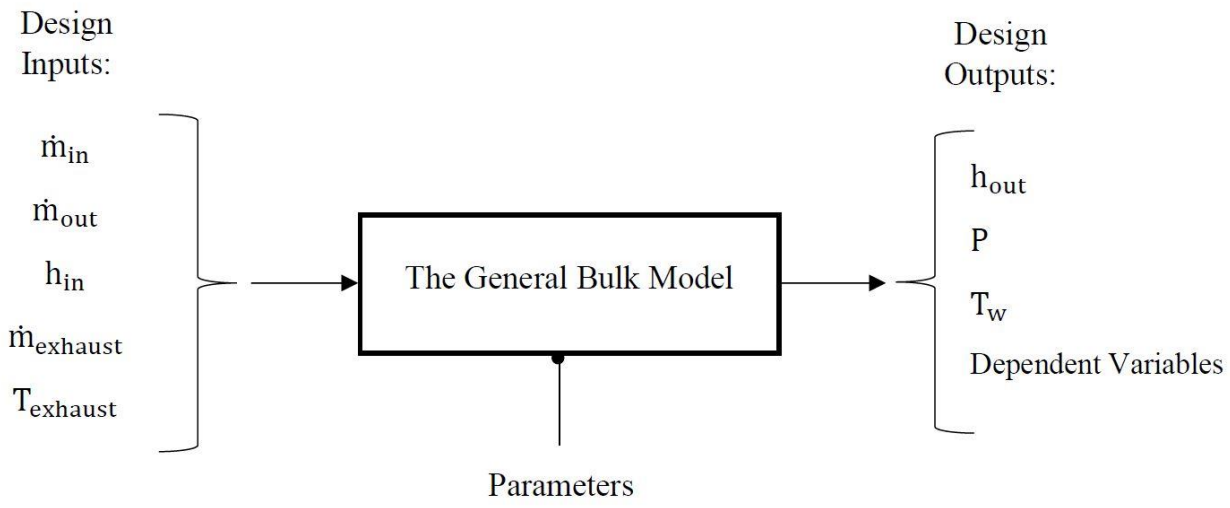

Figure 4-6: Design Inputs and Outputs in the General Bulk Model for Evaporator

4.2.3.4. State Space Model for the Evaporator

Eq. (4-14), (4-18), (4-20) and (4-22) are governing equations for evaporator. Rewriting these equations into a matrix form results in equation (4-26) which is known as state space form [50]:

$$\begin{bmatrix} A_{cs}L_e\left(\frac{\partial\bar{\rho}}{\partial P}\Big|_{\bar{h}}\right) & A_{cs}L_e\left(\frac{\partial\bar{\rho}}{\partial\bar{h}}\Big|_{P}\right) & 0 & 0 \\ A_{cs}L_e\left[\left(\frac{\partial\bar{\rho}}{\partial P}\Big|_{\bar{h}}\right)\bar{h}-1\right] & A_{cs}L_e\left[\left(\frac{\partial\bar{\rho}}{\partial\bar{h}}\Big|_{P}\right)\bar{h}+\bar{\rho}\right] & 0 & 0 \\ 0 & 0 & C_{p_w}\rho_w A_w & 0 \\ 0 & 0 & 0 & A_g L_e \rho_g C_{p,g} \end{bmatrix}_e \begin{bmatrix} \dot{P} \\ \dot{\bar{h}} \\ \dot{T}_w \\ \dot{\bar{T}}_g \end{bmatrix}_e \tag{4-26}$$

$$= \begin{bmatrix} \dot{m}_{in} - \dot{m}_{out} \\ \dot{m}_{in}h_{in} - \dot{m}_{out}h_{out} + L_e p_i \alpha_i (T_w - \bar{T}_r) \\ p_i\alpha_i(\bar{T}_r - T_w) + p_o\alpha_o(\bar{T}_g - T_w) \\ L_e p_o \alpha_o (T_w - \bar{T}_g) + \dot{m}_g C_{p,g}\left(T_{g_{in}} - T_{g_{out}}\right) \end{bmatrix}_e$$

Assuming $\mu = 0.5$ in SOFC mean temperature [$\bar{T}_g = T_{g_{in}}(\mu) + T_{g_{out}}(1-\mu)$] results in:

$$\bar{T}_g = T_{g_{in}}(\mu) + T_{g_{out}}(1-\mu) \rightarrow$$
$$\bar{T}_g = \frac{T_{g_{in}} + T_{g_{out}}}{2} \rightarrow \; T_{g_{out}} = 2\bar{T}_g - T_{g_{in}} \tag{4-27}$$

Also, assume that the mean enthalpy of working fluid is defined as follow:

$$\bar{h} = \frac{(h_{in} + h_{out})}{2} \rightarrow h_{out} = 2\bar{h} - h_{in} \tag{4-28}$$

Rewriting Eq. (4-26) using Eq. (4-27) and (4-28):

$$\begin{bmatrix} A_{cs}L_e\left(\frac{\partial\bar{\rho}}{\partial P}\Big|_{\bar{h}}\right) & A_{cs}L_e\left(\frac{\partial\bar{\rho}}{\partial\bar{h}}\Big|_{P}\right) & 0 & 0 \\ A_{cs}L_e\left[\left(\frac{\partial\bar{\rho}}{\partial P}\Big|_{\bar{h}}\right)\bar{h} - 1\right] & A_{cs}L_e\left[\left(\frac{\partial\bar{\rho}}{\partial\bar{h}}\Big|_{P}\right)\bar{h} + \bar{\rho}\right] & 0 & 0 \\ 0 & 0 & C_{p_w}\rho_w A_w & 0 \\ 0 & 0 & 0 & A_g L_e \rho_g C_{p,g} \end{bmatrix}_e \begin{bmatrix} \dot{P} \\ \dot{\bar{h}} \\ \dot{T}_w \\ \dot{\bar{T}}_g \end{bmatrix}_e$$
$$= \begin{bmatrix} \dot{m}_{in} - \dot{m}_{out} \\ \dot{m}_{in}h_{in} - \dot{m}_{out}(2\bar{h} - h_{in}) + L_e p_i \alpha_i (T_w - \bar{T}_r) \\ p_i\alpha_i(\bar{T}_r - T_w) + p_o\alpha_o(\bar{T}_g - T_w) \\ L_e p_o \alpha_o (T_w - \bar{T}_g) + 2\dot{m}_g C_{p,g}\left(T_{g_{in}} - \bar{T}_g\right) \end{bmatrix}_e \tag{4-29}$$

Equation (4-29) can be rewritten as $Z(x,u).\dot{x} = f(x_e, u_e)$ form, in which matrix of state parameters (x_e), matrix of input parameters (u_e), $Z(x,u)$ and $f(x_e,u_e)$ are as follows [50]:

$$x_e = \begin{bmatrix} P & \bar{h} & T_w & \bar{T}_g \end{bmatrix}_e^T \tag{4-30}$$

$$u_e = \begin{bmatrix} \dot{m}_{in} & \dot{m}_{out} & h_{in} & T_{g_{in}} & \dot{m}_g \end{bmatrix}_e^T \tag{4-31}$$

$$Z(x,u)$$
$$= \begin{bmatrix} A_{cs}L_e\left(\frac{\partial\bar{\rho}}{\partial P}\Big|_{\bar{h}}\right) & A_{cs}L_e\left(\frac{\partial\bar{\rho}}{\partial\bar{h}}\Big|_{P}\right) & 0 & 0 \\ A_{cs}L_e\left[\left(\frac{\partial\bar{\rho}}{\partial P}\Big|_{\bar{h}}\right)\bar{h} - 1\right] & A_{cs}L_e\left[\left(\frac{\partial\bar{\rho}}{\partial\bar{h}}\Big|_{P}\right)\bar{h} + \bar{\rho}\right] & 0 & 0 \\ 0 & 0 & C_{p_w}\rho_w A_w & 0 \\ 0 & 0 & 0 & A_g L_e \rho_g C_{p,g} \end{bmatrix}_e \tag{4-32}$$

$$f(x_e,u_e) = \begin{bmatrix} \dot{m}_{in} - \dot{m}_{out} \\ \dot{m}_{in}h_{in} - \dot{m}_{out}(2\bar{h} - h_{in}) + L_e p_i \alpha_i (T_w - \bar{T}_r) \\ p_i\alpha_i(\bar{T}_r - T_w) + p_o\alpha_o(\bar{T}_g - T_w) \\ L_e p_o \alpha_o (T_w - \bar{T}_g) + 2\dot{m}_g C_{p,g}\left(T_{g_{in}} - \bar{T}_g\right) \end{bmatrix}_e \tag{4-33}$$

4.2.4. Condenser Model

A condenser is a required part of the ORC system in which the working fluid losses its heat to an exterior colder stream, such as an air stream. The dynamics of the condenser are caused by the thermal inertia of the metal components and the fluid, as well as the mass inertia of the gas phase. In the proposed model, the condenser is a cross flow shell and tube heat exchanger that is typical of those used in an ORC system, which is shown in Figure 4-7. The model uses an exterior air flow as the cold fluid while the refrigerant (R245fa) is the hot fluid. Corresponding inputs of the condenser model are: mass flow rate and temperature of the exterior air stream and refrigerant.

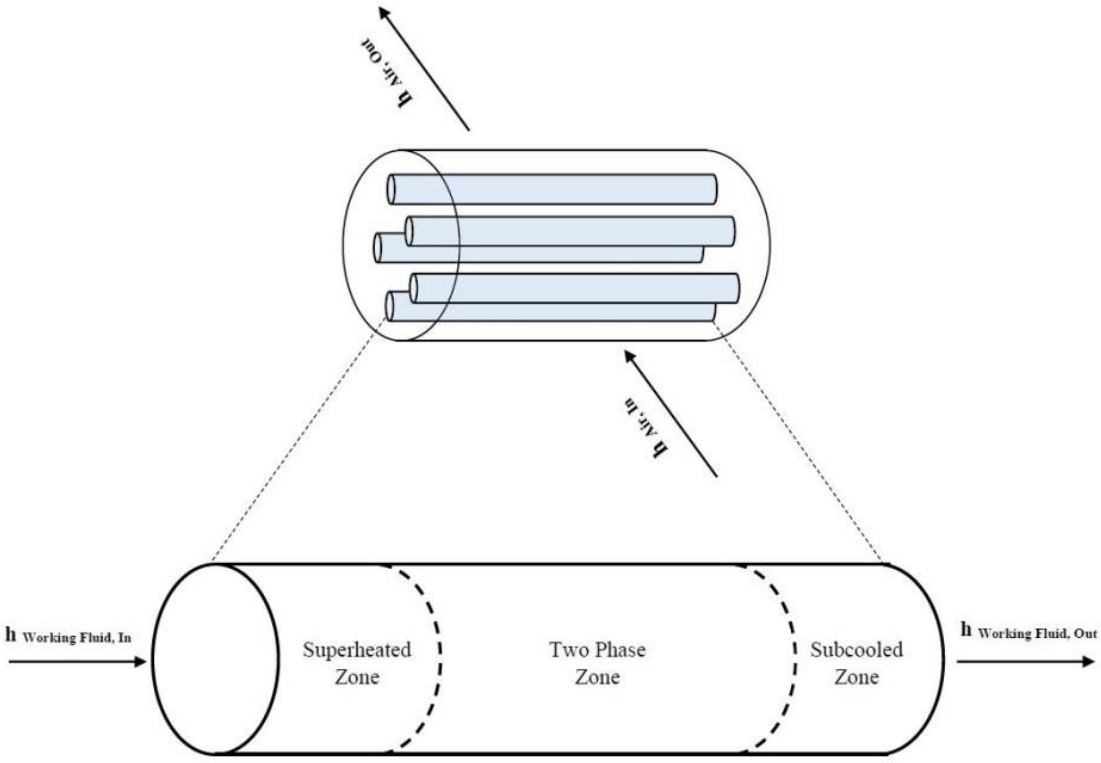

Figure 4-7: Overview of the Condenser Model

Relevant phenomena to be modeled occurring in such heat exchangers, include the heat transfer (convective) from the hot (shell) side to the cold (tube) side, energy accumulation in the metal parts of the exchanger, mass and energy accumulation on both fluid sides of the exchanger (e.g., exterior air stream and R245fa).

Figure 4-8 shows how the temperature of the working fluid typically changes when it flows through the condenser, indicating important points: The condenser outlet temperature (T_{out}), the saturation temperature (T_{sat}) and the difference between these two temperatures is the subcooled temperature difference (ΔT_{sc}).

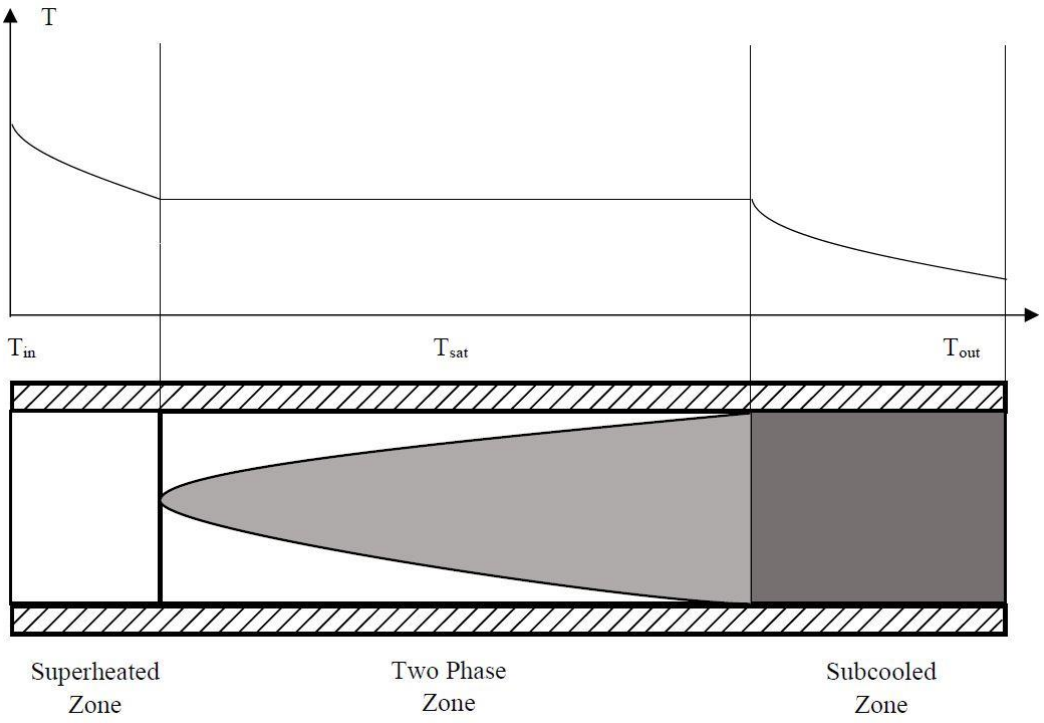

Figure 4-8: Temperature profile of the fluid through the condenser

The modeling methodology for the condenser follows the same methodology as that of the evaporator with a few changes. To simplify the model the same assumptions about the working fluid flow are used.

4.2.4.1. Governing Equations

The derivation of governing equation for mass conservation, Energy conversion at working fluid side, and wall side of condenser follows the same methodology as that of the evaporator with minor changes. The detailed of derivation of Eq. (4-34), (4-35) and (4-36) can be found in Appendix B.

4.2.4.1.1. Mass Conservation at Working Fluid Side

$$\left[A_{cs}L_c\left(\frac{\partial\bar{\rho}}{\partial P}\Big|_{\bar{h}}\right)\right]\dot{\bar{P}}+\left[A_{cs}L_c\left(\frac{\partial\bar{\rho}}{\partial\bar{h}}\Big|_{P}\right)\right]\dot{\bar{h}}+(\dot{m}_{out}-\dot{m}_{in})=0 \tag{4-34}$$

Where A_{cs} is cross sectional area of a tube in which working fluid flows. L_c is the condenser tube length, $\bar{\rho}$ is average density of working fluid in condenser, P is condenser working pressure, $\bar{h}$ is average enthalpy of working fluid in condenser. $\dot{m}_{in}$ and $\dot{m}_{out}$ are the mass flows through the inlet and outlet boundaries, respectively.

4.2.4.1.2. Energy Conservation Equation at Working Fluid Side

$$A_{cs}L_c\left[\left(\frac{\partial\bar{\rho}}{\partial P}\Big|_{\bar{h}}\right)\bar{h}-1\right]\dot{P}+A_{cs}L_c\left[\left(\frac{\partial\bar{\rho}}{\partial\bar{h}}\Big|_{P}\right)\bar{h}+\bar{\rho}\right]\dot{\bar{h}}+(\dot{m}_{out}h_{out}-\dot{m}_{in}h_{in})=$$
$$L_c p_i\alpha_i(T_w-\bar{T}_r) \tag{4-35}$$

Where p_i is the inner cross sectional perimeter of a tube in which working fluid flows. α_i is convection heat transfer coefficient between working fluid and tube. T_w is the evaporator tube wall temperature. $\bar{T}_r$ is working fluid mean temperature in condenser and h_{in} and h_{out} are convective enthalpies throughout the boundaries.

4.2.4.1.3. Energy Conservation at Wall Side

$$C_{p_w}\rho_w A_w\frac{\partial T_w}{\partial t}=p_i\alpha_i(\bar{T}_r-T_w)+p_o\alpha_o(\bar{T}_a-T_w) \tag{4-36}$$

Where C_{p_w} is specific heat capacity of condenser tube wall, ρ_w is density of condenser tube wall, A_w is annulus cross sectional area of tube wall, p_o is the outer cross sectional perimeter of a tube in which working fluid flows, α_o is convection heat transfer coefficient between working fluid and tube and $\bar{T}_a$ is average temperature of cooling air passes through condenser.

4.2.4.1.4. Energy Conservation Equation for Air Side

The energy balance for the air is:

$$\dot{m}_a C_{p_a}\left(T_{a_{in}} - T_{a_{out}}\right) = L_c p_o \alpha_o (\bar{T}_a - T_w) \tag{4-37}$$

Where C_{p_a} is specific heat capacity of air. ($T_{a_{in}}$) and ($T_{a_{out}}$) are inlet and outlet air temperatures respectively. $\dot{m}_a$ is mass flow rate of air passes through condenser.

Assuming that the mean air temperature is $\bar{T}_a = \frac{T_{a_{in}} + T_{a_{out}}}{2}$ results in:

$$\bar{T}_a = \frac{T_{a_{in}} + T_{a_{out}}}{2} \rightarrow \ T_{a_{out}} = 2\bar{T}_a - T_{a_{in}} \tag{4-38}$$

Substituting equation (4-38) in to equation (4-37) as follow:

$$\dot{m}_a C_{p_a}\left(T_{a_{in}} - 2\bar{T}_a + T_{a_{in}}\right) = L_c p_o \alpha_o (\bar{T}_a - T_w) \tag{4-39}$$

Calculating $\bar{T}_a$ from equation (4-39):

$$\bar{T}_a = \frac{\left(\frac{\dot{m}_a C_{p_a}}{L_c p_o \alpha_o}\right) 2T_{a_{in}} + T_w}{1 + 2\left(\frac{\dot{m}_a C_{p_a}}{L_c p_o \alpha_o}\right)} \tag{4-40}$$

4.2.4.2. Heat transfer Coefficient for the Working Fluid side of the Condenser

In this study, as it was mentioned, a bulk model is used to model the working fluid inside the condenser. Thus, working fluid flows inside the condenser has a uniform state along the tube. The model suggested by Cavallini and Zecchin [52] has a typical structure of a single heat transfer correlation. This equation gives the local Nusselt number, but its use is also suggested to predict the mean heat transfer coefficient over the whole tube length by referring to the arithmetic average of the inlet and outlet values of ($\mathrm{Re_{eq}}$).

$$\alpha_{2ph,cond} = 0.05\, Re_{eq}^{0.8} Pr_l^{0.33} \frac{k_l}{D} \tag{4-41}$$

Where $\alpha_{2ph,cond}$ is two phase convective heat transfer coefficient between working fluid and tube wall.

In equation (4-41), Re_{eq} is calculated as follow:

$$Re_{eq} = Re_v \left(\frac{\mu_v}{\mu_l}\right)\left(\frac{\rho_l}{\rho_v}\right)^{0.5} + Re_l \tag{4-42}$$

(Re_l) and (Re_v) are Reynolds numbers for liquid and vapor phases respectively. These Reynolds numbers are defined as below:

$$Re_l = \frac{\dot{m}}{A}\frac{D}{\mu_l}(1-x)$$
$$Re_v = \frac{\dot{m}}{A}\frac{D}{\mu_v}(x) \tag{4-43}$$

4.2.4.3. Boundary condition

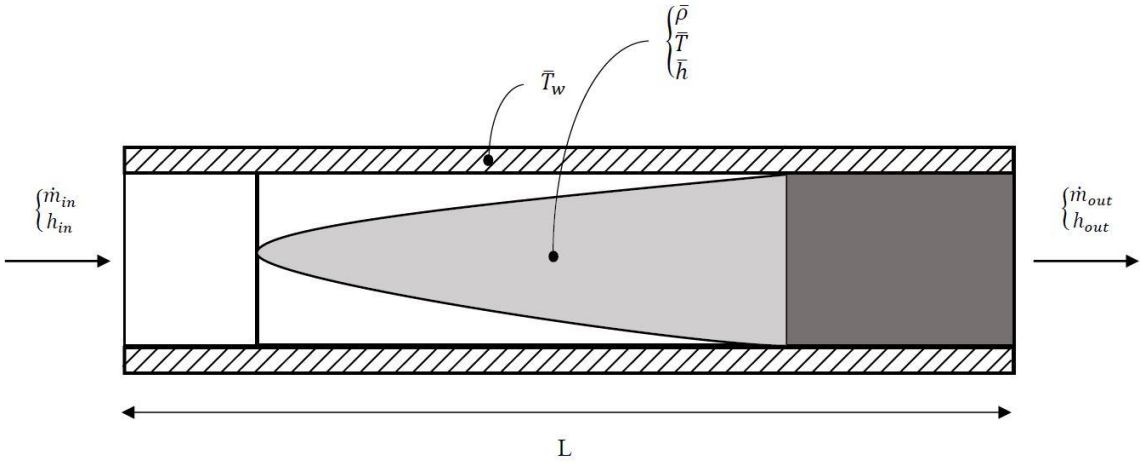

Figure 4-9: Schematic of the Bulk model for Condenser

Figure 4-9 shows a schematic of the general bulk model. Gas is entering with mass flow rate $\dot{m}_{in}$ and enthalpy (h_{in}). In a system model, both of these terms are usually calculated in adjacent model (expander) and are considered as known boundary conditions. Mass flow is leaving the condenser at a rate ($\dot{m}_{out}$), which is also usually calculated in a succeeding model (pump) and is considered as a known boundary condition for this model. The boundary conditions correspond to a design case, which may be changed as required. The condenser is cooled by the air stream. The other terms shown on the schematic are calculated in the model and are thus results of the model.

The design inputs and outputs are shown on Figure 4-10, where dependent variables are those, which can be calculated from other output variables.

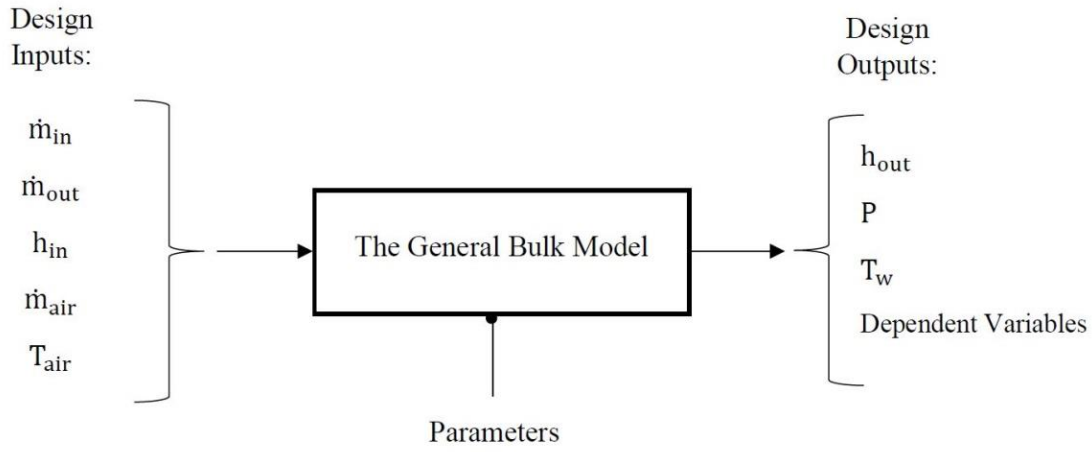

Figure 4-10: Design Input and Outputs in the General Bulk Model for Condenser

4.2.4.4. State Space Model for the Condenser

Eq. (4-34), (4-35) and (4-36) are governing equations for condenser. Rewriting these equations into a matrix form results in equation (4-44) which is known as state space form [50]:

$$\begin{bmatrix} A_{cs}L_c\left(\frac{\partial\bar{\rho}}{\partial P}\Big|_{\bar{h}}\right) & A_{cs}L_c\left(\frac{\partial\bar{\rho}}{\partial\bar{h}}\Big|_{P}\right) & 0 \\ A_{cs}L_c\left[\left(\frac{\partial\bar{\rho}}{\partial P}\Big|_{\bar{h}}\right)\bar{h}-1\right] & A_{cs}L_c\left[\left(\frac{\partial\bar{\rho}}{\partial\bar{h}}\Big|_{P}\right)\bar{h}+\bar{\rho}\right] & 0 \\ 0 & 0 & C_{p_w}\rho_w A_w \end{bmatrix}_c \begin{bmatrix} \dot{P} \\ \dot{\bar{h}} \\ \dot{T}_w \end{bmatrix}_c \tag{4-44}$$

$$= \begin{bmatrix} \dot{m}_{in}-\dot{m}_{out} \\ \dot{m}_{in}h_{in}-\dot{m}_{out}(h_{out})+L_c p_i\alpha_i(T_w-\bar{T}_r) \\ p_i\alpha_i(\bar{T}_r-T_w)+p_o\alpha_o(\bar{T}_a-T_w) \end{bmatrix}_c$$

Assume that the mean enthalpy of working fluid is defined as follow:

$$\bar{h}=\frac{(h_{in}+h_{out})}{2}\rightarrow h_{out}=2\bar{h}-h_{in} \tag{4-45}$$

Rewriting Eq. (4-44) using Eq. (4-45):

$$\begin{bmatrix} A_{cs}L_c\left(\frac{\partial\bar{\rho}}{\partial P}\Big|_{\bar{h}}\right) & A_{cs}L_c\left(\frac{\partial\bar{\rho}}{\partial\bar{h}}\Big|_{P}\right) & 0 \\ A_{cs}L_c\left[\left(\frac{\partial\bar{\rho}}{\partial P}\Big|_{\bar{h}}\right)\bar{h}-1\right] & A_{cs}L_c\left[\left(\frac{\partial\bar{\rho}}{\partial\bar{h}}\Big|_{P}\right)\bar{h}+\bar{\rho}\right] & 0 \\ 0 & 0 & C_{p_w}\rho_w A_w \end{bmatrix}_c \begin{bmatrix} \dot{P} \\ \dot{\bar{h}} \\ \dot{T}_w \end{bmatrix}_c \tag{4-46}$$

$$= \begin{bmatrix} \dot{m}_{in}-\dot{m}_{out} \\ \dot{m}_{in}h_{in}-\dot{m}_{out}(2\bar{h}-h_{in})+L_c p_i\alpha_i(T_w-\bar{T}_r) \\ p_i\alpha_i(\bar{T}_r-T_w)+p_o\alpha_o(\bar{T}_a-T_w) \end{bmatrix}_c$$

Eq. (4-46) can be rewritten as $Z(x,u).\dot{x}=f(x_c,u_c)$ form, in which matrix of state parameters (x_c), matrix of input parameters (u_c), $Z(x,u)$ and $f(x_c,u_c)$ are as follows:

$$x_c = [P \quad \bar{h} \quad T_w]_c^{\ T} \tag{4-47}$$

$$u_c = [\dot{m}_{in} \quad \dot{m}_{out} \quad h_{in} \quad T_{a\,in} \quad \dot{m}_a]_c^{\ T} \tag{4-48}$$

$$Z(x,u) = \begin{bmatrix} A_{cs}L_c\left(\frac{\partial\bar{\rho}}{\partial P}\Big|_{\bar{h}}\right) & A_{cs}L_c\left(\frac{\partial\bar{\rho}}{\partial\bar{h}}\Big|_{P}\right) & 0 \\ A_{cs}L_c\left[\left(\frac{\partial\bar{\rho}}{\partial P}\Big|_{\bar{h}}\right)\bar{h}-1\right] & A_{cs}L_c\left[\left(\frac{\partial\bar{\rho}}{\partial\bar{h}}\Big|_{P}\right)\bar{h}+\bar{\rho}\right] & 0 \\ 0 & 0 & C_{p_w}\rho_w A_w \end{bmatrix}_c \tag{4-49}$$

$$f(x_c,u_c) = \begin{bmatrix} \dot{m}_{in}-\dot{m}_{out} \\ \dot{m}_{in}h_{in}-\dot{m}_{out}(2\bar{h}-h_{in})+L_c p_i\alpha_i(T_w-\bar{T}_r) \\ p_i\alpha_i(\bar{T}_r-T_w)+p_o\alpha_o(\bar{T}_a-T_w) \end{bmatrix}_c \tag{4-50}$$

4.2.5. Convection Heat Transfer Coefficient outside the Tube

The annularly finned tubes heat exchangers which are arranged in staggered manner are utilized as evaporator and condenser in this ORC system (Figure 4-11 and Figure 4-12). The heat transfer coefficient between the tube wall and SOFC exhaust gas for evaporator and heat transfer coefficient between the tube wall and cooling air can be calculated by Eq. (4-51).

$$\alpha_o = \alpha_{o,dp}\left(\frac{\dot{m}}{\dot{m}_{dp}}\right)^m \tag{4-51}$$

In Eq. (4-51), α_o is convection heat transfer coefficient in the evaporator and condenser outside surface for variable mass flow rate ṁ and $\alpha_{o,dp}$ is design point convection heat transfer coefficient in the evaporator and condenser outside surface for design point $\dot{m}_{dp}$ and m is a coefficient based on the number and arrangement of evaporator's and condenser's tubes inside the shell.

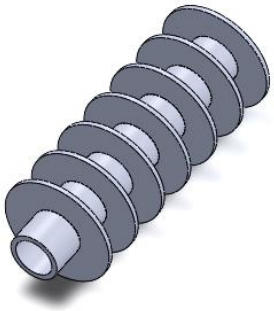

Figure 4-11: Schematic of High Finned Tubes Used in Evaporator and Condenser models

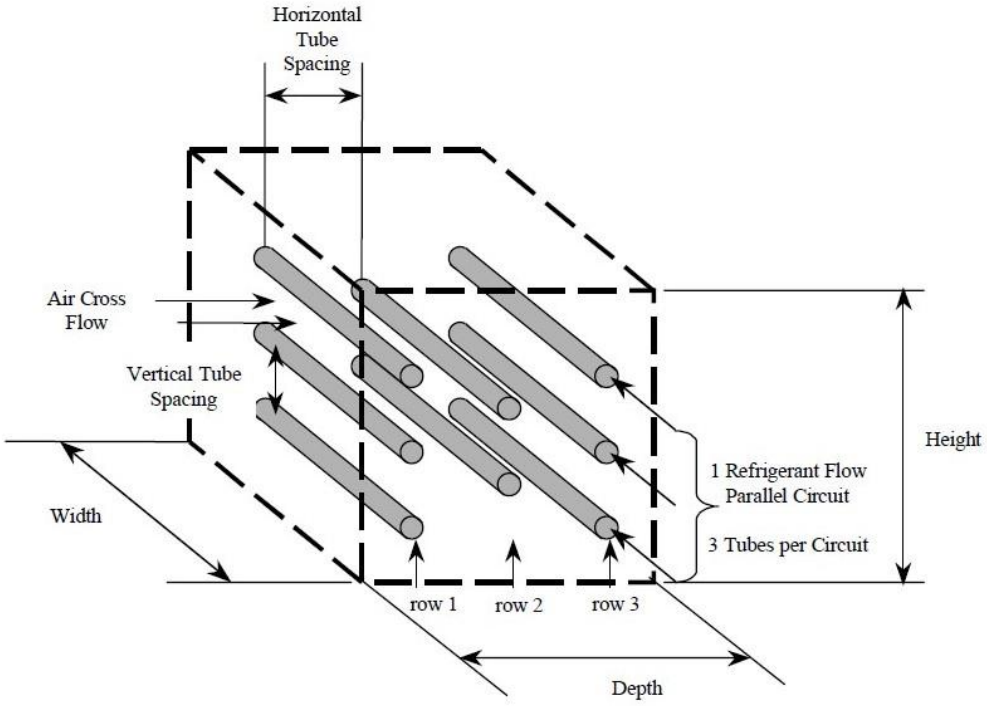

Figure 4-12: Schematic of the Evaporator's Annular Tubes Arranged in Staggered Manner

All finned tube heat transfer coefficient are obtained from the result of known experimental correlations. Various researchers have conducted tests that have yielded different experimental

relational forms, but with results that are phenomenologically similar. For the high finned tube banks, heat transfer coefficient α_o is calculated by Briggs and Young's experimental correlations [53]:

$$\alpha_o = 0.1378 \frac{\lambda}{D_o} \left(\frac{D_o\, G_m}{\mu}\right)^{0.718} \left(\frac{C_p\, \mu}{\lambda}\right)^{\frac{1}{3}} \left(\frac{Y}{H}\right)^{0.296} \tag{4-52}$$

In Eq. (4-52), G_m is mass flux of SOFC exhaust gas or air through minimum flow area, H is fin Height, Y is fin spacing. The heat transfer coefficient based on bare tube outer surface is then obtained by:

$$\alpha_{o,dp} = \alpha_{o,i}.\beta.\eta_f \tag{4-53}$$

In the above equation, β is finned ratio and η_f is fin efficiency. Fin efficiency is due to a temperature change through fin. (β) is defined as:

$$\beta = \frac{total\ surface(fin\ and\ origin)}{outer\ surface} \tag{4-54}$$

4.2.6. Reservoir Model

The model of the reservoir can be represented by mass and energy balances of working fluid as Eq. (4-55) and (4-56) respectively.

$$\frac{dm_{res}}{dt} = \dot{m}_{res,i} - \dot{m}_{res.o} \tag{4-55}$$

$$\frac{dh_{res}}{dt} = \frac{\dot{m}_{res,i}\left(h_{res,i} - h_{res}\right) - \dot{m}_{res,o}\left(h_{res,o} - h_{res}\right)}{m_{rec}} \tag{4-56}$$

In the above equations, (m_{res}) is the mass of the reservoir's fluid, ($\dot{m}_{res,i}$) and ($\dot{m}_{res,o}$) are reservoir's inlet and outlet mass flow rates and (h_{res}), ($h_{res,i}$) and ($h_{res,o}$) are enthalpy of working fluid inside the reservoir and inlet and outlet enthalpy of working fluid.

The reservoir is considered large enough, so ($\dot{m}_{res,i} = \dot{m}_{res.o}$) and ($h_{res,o} = h_{res}$). So, Eq. (4-55) can be neglected and Eq. (4-56) simplifies to:

$$\frac{dh_{res}}{dt} = \frac{\dot{m}_{res,o}\left(h_{res,i} - h_{res}\right)}{m_{res}} \tag{4-57}$$

As a consequence, the dynamics of the reservoir can be described by the state space equation of $\dot{x}_r = f(x_r, u_r)$ in which state parameters and input parameters are:

$$x_r = [h_{res}]_r^T \tag{4-58}$$

$$u_r = [h_{res,i} \quad \dot{m}_{res,o}]_r^T \tag{4-59}$$

4.2.7. Pump Model

Dynamic modeling of pump is much faster than that of evaporator, so for pump a static model is used. The mass flow rate corresponding to different rotational speed in the pump is expressed as follows [54]:

$$\frac{\dot{m}_p}{\dot{m}_{p,n}} = \frac{N_p}{N_{p.n}} \tag{4-60}$$

In Eq. (4-60), $\dot{m}_{p,n}$ and $N_{p.n}$ are nominal mass flow rate and rotational speed of pump and $\dot{m}_p$ is a variable mass flow rate corresponds to variable rotational speed (N_p).

Positive displacement pump model used in this study follows the semi-empirical model proposed by Quoilin et al. [55], which is based on the capacity factor of the pump which is defined by:

$$X_{pp} = \frac{\dot{m}_p}{\rho_{cd_{out}} \dot{V}_{max}} \tag{4-61}$$

In Eq. (4-61), $\rho_{cd_{out}}$ is the density of working fluid in the condenser outlet and $\dot{V}_{max}$ is maximum pump volumetric flow rate.

In Eq. (4-61), X_{pp} is limited by the following boundary condition:

$$0.1 \leq X_{pp} \leq 1 \tag{4-62}$$

The pump internal isentropic efficiency is defined by:

$$\eta_p = \frac{P_{ev} - P_{cd}}{\rho_{cd_{out}}(h_{p_{out}} - h_{p_{in}})} \tag{4-63}$$

In Eq. (4-63), P_{ev} and P_{cd} are evaporator and condenser pressures and $h_{p_{in}}$ and $h_{p_{out}}$ are pump's inlet and outlet enthalpy.

An empirical law provided is fitted by a third order polynomial in the form of:

$$\eta_p = a_0 + a_1.log(X_{pp}) + a_2.log(X_{pp})^2 + a_3.log(X_{pp})^3 \tag{4-64}$$

The outlet enthalpy of the pump can be described by:

$$h_{p_{out}} = h_{p_{in}} + \frac{P_{ev} - P_{cd}}{\rho_{cd_{out}}\eta_p} \tag{4-65}$$

Also, the pump work is obtained as:

$$W_p = \frac{\bar{v}_p(P_{ev} - P_{cd})\dot{m}_p}{\eta_p} \tag{4-66}$$

In Eq. (4-66), $\bar{v}_p$ is the working fluid's average specific volume in the pump.

The obtained steady state model for the pump can be expressed in matrix form as follow:

$$y_p = f_p(u_p) \tag{4-67}$$

In equation (4-67) input and outputs are:

$$u_p = [N_p \quad h_{p_{in}} \quad P_{ev} \quad P_{cd} \quad \rho_{cd_{out}}]_p^T \tag{4-68}$$

$$y_p = [\dot{m}_p \quad h_{p_{out}} \quad W_p]_p^T \tag{4-69}$$

4.2.8. Expander Model

Experimental studies of small scale ORC units demonstrated that a scroll expander is a good candidate for small scale power generation, because of its reduced number of moving parts,

reliability, wide output power range, and broad availability. The oil-free scroll expander is the best component for converting heat into mechanical energy. The dynamic response characteristics of an expander are very fast compared with the dynamics of the evaporator, so that a steady-state model is established for the scroll expander, in which the expansion losses are modeled by dividing the expansion into two steps: Isentropic expansion and constant volume expansion [53].

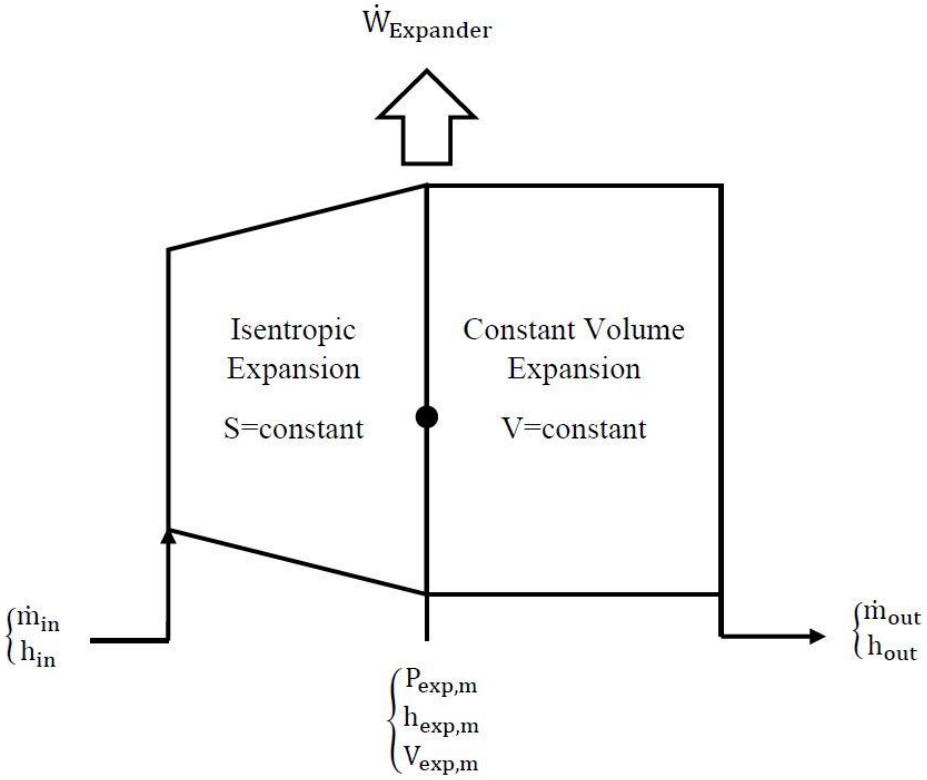

Figure 4-13: Conceptual Scheme of the Expander Model

The isentropic expansion work and constant volume expansion work are calculated as follow:

$$w_1 = h_{exp,in} - h_{exp,m} = \frac{K}{K-1} P_{exp.in} v_{exp,in} \left[1 - \left(\frac{1}{r_{v,m}}\right)^{K-1}\right] \quad (4\text{-}70)$$

$$w_2 = v_{exp,m}(P_{exp,m} - P_{cond}) \quad (4\text{-}71)$$

In the above equations, w_1 and w_2 are specific expander's works in isentropic expansion and constant volume expansion parts, $h_{exp,in}$ is the working fluid's enthalpy at expander's inlet, $h_{exp,m}$

is the working fluid's enthalpy at isentropic expansion part outlet, K is the specific heat ratio, $P_{exp.in}$ and $v_{exp,in}$ are pressure and specific volume at the inlet of expander. ($r_{v,m}$) is the ratio between inlet pocket volume and outlet pocket volume and $v_{exp,m}$ is the working fluid's specific volume at the outlet of isentropic expansion part.

Other losses caused by internal leakage, supply pressure drop, heat transfer and friction are lumped into one single mechanical efficiency term, η_{exp}, thus the mechanical work of expander can be obtained by summing w_1 and w_2 and multiplying by this efficiency. So, the total mechanical work of the expander is:

$$\dot{W} = \dot{m}_{exp} \times (w_1 + w_2) \times \eta_{exp} \tag{4-72}$$

Since the expansion is assumed adiabatic, then:

$$h_{exp,out} = h_{exp,in} - \frac{\dot{W}}{\dot{m}_{exp}} \tag{4-73}$$

The mass flow rate entering the expander is formulated by:

$$\dot{m}_{exp} = \frac{f V_s N_{exp}}{60 v_{exp,i}} \tag{4-74}$$

In Eq. (4-74), V_s is the swept volume of expander, N_{exp} is the rotational speed of the expander and f is the filling factor. The volumetric performance of the expander is represented by the filling factor which is defined as the ratio between the measured mass flow rate and the mass flow rate theoretically displaced by the expander.

Thus, a steady-state model is established by the following equation:

$$y_{exp} = f_{exp}(u_{exp}) \tag{4-75}$$

In Eq. (4-75) input and outputs are:

$$u_{exp} = [P_{exp,in} \quad v_{exp,in} \quad P_{cond} \quad N_{exp} \quad h_{exp,in}]^T_{exp} \tag{4-76}$$

$$y_{exp} = \left[\dot{m}_{exp} \quad \dot{W} \quad h_{exp,out}\right]_{exp}^{T} \tag{4-77}$$

4.2.9. Overall ORC Model

The overall model of the ORC is obtained by interconnecting each subcomponent model. The input matrix of all the components is presented below.

$$u_e = \left[\dot{m}_{in} \quad \dot{m}_{out} \quad h_{in} \quad T_{g_{in}} \quad \dot{m}_g\right]_e^{T} = \left[y_p(1) \quad y_{exp}(1) \quad y_p(2) \quad T_{g_{in}} \quad \dot{m}_g\right]^{T} \tag{4-78}$$

$$u_c = \left[\dot{m}_{in} \quad \dot{m}_{out} \quad h_{in} \quad T_{a_{in}} \quad \dot{m}_a\right]_c^{T} = \left[y_{exp}(1) \quad y_p(1) \quad y_{exp}(3) \quad T_{a_{in}} \quad \dot{m}_a\right]^{T} \tag{4-79}$$

$$u_{res} = \left[h_{res,i} \quad \dot{m}_{res,o}\right]_r^{T} = \left[f_1(x_c(2), y_{exp}(3)) \quad y_p(1)\right]^{T} \tag{4-80}$$

$$\begin{aligned} u_p &= \left[N_p \quad h_{p_{in}} \quad P_{ev} \quad P_{cd} \quad \rho_{cd_{out}}\right]_p^{T} \\ &= \left[N_p \quad x_{res}(1) \quad x_c(1) \quad x_e(1) \quad f_2(x_c(1), x_c(2))\right]^{T} \end{aligned} \tag{4-81}$$

$$\begin{aligned} u_{exp} &= \left[P_{exp,in} \quad v_{exp,in} \quad P_{cond} \quad N_{exp} \quad h_{exp,in}\right]_{exp}^{T} \\ &= \left[x_e(1) \quad f_3(x_e(1), x_e(2)) \quad x_c(1) \quad N_{exp} \quad f_4(x_e(2), y_p(2))\right] \end{aligned} \tag{4-82}$$

In the above equations, $\left[f_1\left(x_c(2), y_{exp}(3)\right) = 2x_c(2) - y_{exp}(3)\right]$, $\left[f_4\left(x_e(2), y_p(2)\right) = 2x_e(2) - y_p(2)\right]$ and f_2 and f_3 are the working fluid's properties which are calculated by using properties of working fluid from Engineering Equation Solver (EES).

Figure 4-14 schematically depicts the inputs, outputs and disturbances in the ORC dynamic model.

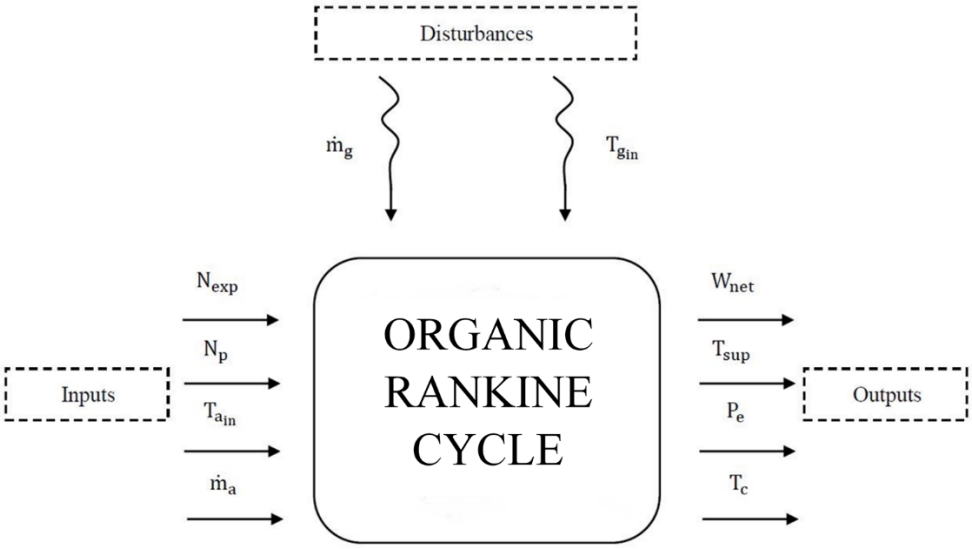

Figure 4-14: Inputs, Outputs and Disturbances in the ORC Dynamic Model

The dynamic characteristic of the ORC system (state parameters) is described by:

$$x = \begin{bmatrix} P_e & \bar{h}_e & \bar{T}_{w,e} & \bar{T}_g & P_c & \bar{h}_c & \bar{T}_{w,c} & h_{res} \end{bmatrix}^T \quad (4\text{-}83)$$

The input and output parameters of the overall system's model are:

$$u = [N_p \quad N_{exp} \quad T_{a_{in}} \quad \dot{m}_a] \quad (4\text{-}84)$$

$$y = [W_{net} \quad T_{su} \quad P_e \quad T_c] \quad (4\text{-}85)$$

The disturbance vector $d = \begin{bmatrix} T_{g_{in}} & \dot{m}_g \end{bmatrix}^T$ stands for disturbances induced by the SOFC exhaust gas. ($\dot{m}_g$) and ($T_{g_{in}}$) are the mass flow rate and temperature of the SOFC exhaust gas at the inlet of the evaporator respectively.

The dynamic characteristic of the ORC (in state space form) is:

$$Z\dot{x} = F \quad (4\text{-}86)$$

In Eq. (4-86), Matrixes are defined as follow:

$$z = \begin{bmatrix} \left[A_{cs}L_e\left(\frac{\partial\bar{\rho}}{\partial P}\middle|_{\bar{h}}\right)\right]_e & \left[A_{cs}L_e\left(\frac{\partial\bar{\rho}}{\partial\bar{h}}\middle|_P\right)\right]_e & 0 & 0 & 0 & 0 & 0 & 0 \\ \left[A_{cs}L_e\left[\left(\frac{\partial\bar{\rho}}{\partial P}\middle|_{\bar{h}}\right)\bar{h}-1\right]\right]_e & \left[A_{cs}L\left[\left(\frac{\partial\bar{\rho}}{\partial\bar{h}}\middle|_P\right)\bar{h}+\bar{\rho}\right]\right]_e & 0 & 0 & 0 & 0 & 0 & 0 \\ 0 & 0 & \left(C_{p_w}\rho_w A_w\right)_e & 0 & 0 & 0 & 0 & 0 \\ 0 & 0 & 0 & A_g L_e \rho_g C_{p,g} & 0 & 0 & 0 & 0 \\ 0 & 0 & 0 & 0 & \left[A_{cs}L_c\left(\frac{\partial\bar{\rho}}{\partial P}\middle|_{\bar{h}}\right)\right]_c & \left[A_{cs}L_c\left(\frac{\partial\bar{\rho}}{\partial\bar{h}}\middle|_P\right)\right]_c & 0 & 0 \\ 0 & 0 & 0 & 0 & \left[A_{cs}L_c\left[\left(\frac{\partial\bar{\rho}}{\partial P}\middle|_{\bar{h}}\right)\bar{h}-1\right]\right]_c & \left[A_{cs}L_c\left[\left(\frac{\partial\bar{\rho}}{\partial\bar{h}}\middle|_P\right)\bar{h}+\bar{\rho}\right]\right]_c & 0 & 0 \\ 0 & 0 & 0 & 0 & 0 & 0 & \left(C_{p_w}\rho_w A_w\right)_c & 0 \\ 0 & 0 & 0 & 0 & 0 & 0 & 0 & 1 \end{bmatrix} \quad (4\text{-}87)$$

$$x = \begin{bmatrix} P_e & \bar{h}_e & \bar{T}_{w,e} & \bar{T}_g & P_c & \bar{h}_c & \bar{T}_{w,c} & h_{res} \end{bmatrix}^T \quad (4\text{-}88)$$

$$F = \begin{bmatrix} \left(\dot{m}_{in} - \dot{m}_{out}\right)_e \\ \left(\dot{m}_{in}h_{in} - \dot{m}_{out}(2\bar{h} - h_{in}) + L_e p_i \alpha_i (T_w - \bar{T}_r)\right)_e \\ \left(p_i\alpha_i(\bar{T}_r - T_w) + p_o\alpha_o\left(\bar{T}_g - T_w\right)\right)_e \\ \left(L_e p_o \alpha_o\left(T_w - \bar{T}_g\right) + 2\dot{m}_g C_{p,g}\left(T_{g_{in}} - \bar{T}_g\right)\right)_e \\ \left(\dot{m}_{in} - \dot{m}_{out}\right)_c \\ \left(\dot{m}_{in}h_{in} - \dot{m}_{out}\left(2\bar{h} - h_{in}\right) + L_c p_i \alpha_i (T_w - \bar{T}_r)\right)_c \\ \left(p_i\alpha_i(\bar{T}_r - T_w) + p_o\alpha_o(\bar{T}_a - T_w)\right)_c \\ \frac{\dot{m}_{res,o}}{m_{res}}\left(h_{res,i} - h_{res}\right) \end{bmatrix} \quad (4\text{-}89)$$

4.3. Absorption Chiller Modeling

The dynamic absorption chiller model was based upon a similar system configuration for a Yazaki Energy, Inc. CH-KE4040 double-effect lithium bromide absorption chiller rated for 40 refrigeration tons (RT) [56]. A single-effect AC incorporates one generator with one heat exchanger whereas a double-effect AC has two generators and multiple heat exchangers. The second generator recovers leftover heat from the first generator which increases the overall system coefficient of performance (COP). A system diagram is provided in Figure 4-15.

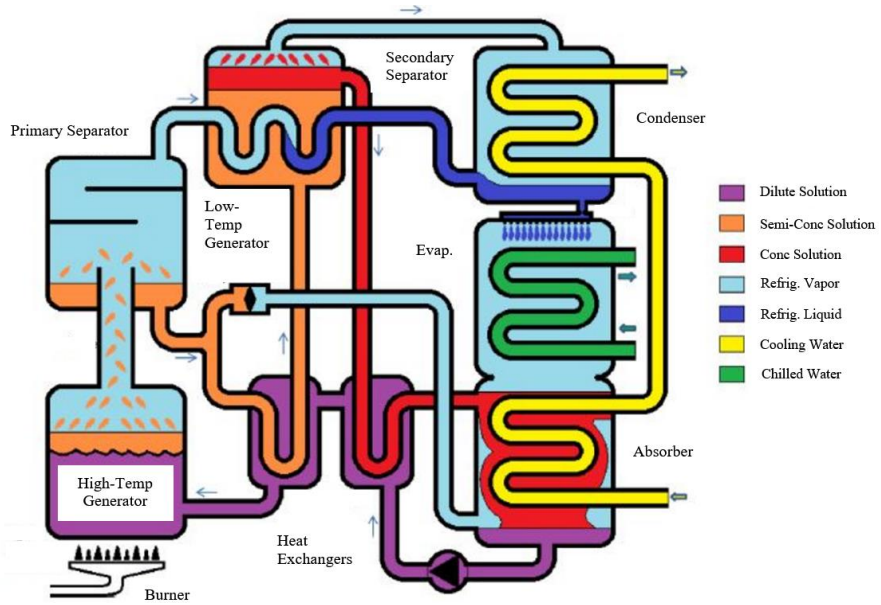

Figure 4-15: Yazaki double-effect lithium bromide absorption chiller system schematic (Yazaki Energy, Inc., 2003)

Energy and mass conservation relations were applied to the AC model with the fluid properties for water using data from The International Association for the Properties of Water and Steam, 1997 whereas the lithium-bromide (LiBr) fluid and thermal properties used were from the American Society of Heating, Refrigerating and Air-Conditioning Engineers Fundamentals Handbook, 1989. For example, in the first generator the energy balance used is given by Eq. 3-90 [17].

$$\frac{dE_{gen1}}{dt} = \dot{m}_{weak}h_{weak} + \dot{Q}_{exh} - \dot{m}_{refrig}h_{refrig} - \dot{m}_{med}h_{med} \tag{4-90}$$

Equation 3-90 describes the change in energy with respect to time in the generator for a weak solution ($\dot{m}_{weak}h_{weak}$) that has added heat ($\dot{Q}_{exh}$), the outlet energy of the generator is balanced by the exiting refrigerant ($\dot{m}_{refrig}h_{refrig}$ $\dot{m}_{refrig}h_{refrig}$), which is steam for a lithium-bromide AC, and the medium solution ($\dot{m}_{med}h_{med}$). Weak solution corresponds to a mixture of about 52% LiBr in water, medium solution consists of about 56% LiBr, and strong solution consists of about 58% LiBr in water. The thermal mass of the generator is significant and is considered with respect to Equation 3-90.

$$\frac{dE_{gen1}}{dt} = \frac{dT_{gen1}}{dt} M_{stored} C_{stored} \tag{4-91}$$

M_{stored} in Eq. 3-91 corresponds to the mass of the first generator (stainless steel) and the fluids contained therein. C_{stored} corresponds to the heat capacity of the generator and contained fluids. The change in temperature considers a combination of Eq. 3-90 and 3-91 as well as radiation heat losses ($\dot{Q}_{rad}$).

$$\frac{dT_{gen1}}{dt} = \frac{\dot{Q}_{gen1} + \dot{m}_{weak} h_{weak} - \dot{m}_{refrig} h_{refrig} - \dot{m}_{med} h_{med} - \dot{Q}_{rad}}{M_{stored} C_{stored}} \tag{4-92}$$

The generator's temperature is then calculated by integrating Eq. 3-92 with a specified initial temperature of the generator with respect to time. Radiative heat losses ($\dot{Q}_{rad}$) are calculated according to Eq. 3-93.

$$\dot{Q}_{rad} = \sigma A (T_{gen1}^4 - T_{amb}^4) \tag{4-93}$$

The area (A) corresponds to the surface area of the generator and ambient temperature is taken as 30°C. A similar analysis is performed for each major component of the AC including the second generator, condenser, and the absorber. Heat exchanger heat transfer calculations are based upon the effectiveness-NTU method for a single pass, cross-flow heat exchanger. MATLAB Simulink was used to simulate the dynamic operation of a chiller under the exhaust conditions of the SOFC system [36].

The combined utilization coefficient used to evaluate the overall system efficiency is given by:

$$H_{CCP} = \frac{\dot{W}_{SOFC} + \dot{Q}_{cooling}}{\dot{N}_{fuel}. LHV_{fuel}} \tag{4-94}$$

5. RESULTS

5.1. Overview

In this study, the possibility of using a highly efficient, zero emission solid oxide fuel cell (SOFC) system that can be dynamically dispatched to produce electricity and cooling in various amounts to meet energy and electricity demands is investigated. Although SOFC systems exhibit high electrical efficiency, in practical applications almost half of the fuel energy is converted to heat. The SOFC high temperature (high quality) heat can be used as the primary thermal energy source to supply cooling or heating or to produce extra electricity through a bottoming cycle. In this study the waste heat from the fuel cell is captured and processed through an organic Rankine cycle (ORC) to produce extra electricity, and then the exhaust goes through an absorption chiller to provide cooling for meeting a cooling demand.

In the first section the SOFC dynamic model is verified by comparison to the measured performance of two commercially available 1.5kW and 2.5kW SOFC systems from SOLIDpower S.p.a. Then, a complete ORC cycle is designed based upon the desired outputs and the SOFC steady state working condition. In the next section, the ORC model is verified by comparison to data from a Zhang et al. study [53] in two scenarios. Then, a case study which includes the data from an Irvine residential apartment complex is introduced. Steady state and dynamic operation of the integrated system to meet this demand is explained in the last section.

5.2. Solid Oxide Fuel Cell Dynamic Model Verification

Two different commercially available SOFC systems were used to verify the model. The first one is the BlueGEN CHP unit, originally manufactured by Ceramic Fuel Cells Ltd (CFCL). BlueGEN is a commercially available SOFC CHP system, now built and sold by SOLIDpower, designed for small- to medium-scale building applications. Operating on natural gas, the unit can

produce power modulated from 500We (25%) to 2kWe (100%); however, it achieves its highest net electrical efficiency of 60% at a 1.5kWe output. As a result, SOLIDpower has optimized the default operation of the unit at 1.5kWe to provide the highest electrical efficiency and thus greatest economic benefit to the user. The BlueGEN SOFC unit consists of 51 planar type YSZ (Yttria-stabalised Zirconia) electrolyte-supported cell layer sets (each layer consist of 4 cells), and operates at around 750℃. Hydrogen is produced from natural gas by internal steam reforming (endothermic) on the fuel cell anode, utilizing the heat and water of the electrochemical reactions (exothermic). The BlueGEN SOFC unit is installed at The National Fuel Cell Research Center (NFCRC) as shown in Figure 5-1. Table 5-1 shows the main technical data for the BlueGEN as published on the SOLIDpower website [57]:

Table 5-1: Technical data for the BlueGEN

Parameter	**Value**
Operation mode	Power-led, continuous (approx. 8,700h per year)
Fuel type	Natural gas, bio-methane
Fuel cell technology	SOFC (Solid Oxide Fuel Cell)
Fuel consumption	2.51kW
Electrical efficiency	Up to 60 % (1.5kW)
Thermal efficiency	Up to 25 % (0.6kW)
Overall efficiency	Up to 85 %
Electrical energy generated per year	~ 13,000kWhe
Thermal energy generated per year	~ 5,220kWhth
Control	Remote monitoring and control via Internet
Weight, Dimensions (H x W x D)	195kg, 1,010 x 600 x 660mm
Noise level	< 47db (A)
Service interval	12 months

Figure 5-1: 1.5 kW BlueGEN installed in the NFCRC laboratory

The second SOFC system used for model verification is the EnGen 2500 mCHP (micro-Combined Heat and Power) unit designed and produced by SOLIDpower, for residential use or small-scale commercial applications. The Engen-2500 system is a floor-standing unit generating a maximum of 2.5 kWe of net AC power at 50% efficiency, combined with a high amount of cogeneration potential and efficiency (90%). EnGen can run solely on natural gas fuel from the grid at normal supply pressure. When integrated for mCHP purposes, the system is controlled by the heat available at output, meaning the integrated system controller modulates power output following a heat demand command from an external energy manager. As an alternative, the system can also be operated in load-following heat-capped mode where the power can be modulated between 30% and 100% of total rated stack power [58]. The EnGen-2500 SOFC unit is installed at The National Fuel Cell Research Center (NFCRC) as shown in Figure 5-2. Table 5-2 shows the main technical and operational data for the Engen-2500 as published on the SOLIDpower website:

Table 5-2: Technical and operational data for the Engen-2500

Parameter	Value
Maximum electric AC power	2.5[kW]
Nominal electrical power range	2.0-2.5[kW]
Electrical modulation range	30-100 [%]
Energy efficiency (AC power, LHV)	>50 [%]
Cogeneration efficiency (H_2O Temp. @ 30°C)	>90 [%]
Maximum measurements of installation space	1.2 x 1.5 x 1.7[m] (W x L x H)
Weight	<350[kg] or <772[lbs]
Electrical connection	Grid network
Fuel	Natural gas grid
Operation modes	Baseload/Load-following heat-capped CHP mode
Thermal cycles per year	10
Start-up time	<8[hrs]
Recommended thermal storage volume	>300[L]
Return water temperature	30-70[°C]
Noise	<50[dB(A)]
Maintenance interval	1[yr]

Figure 5-2: EnGen 2500 SOFC System installed in the NFCRC laboratory

These two SOFC systems (BlueGEN & EnGen) have been used for verification of the developed model.

5.2.1. SOFC Model Verification with BlueGEN

Some of the parameters and design operating conditions of the commercial 1.5kW SOFC are listed in Table 5-3. Input parameters of the developed model are adjusted according to the operating condition of the 1.5kW BlueGEN. Figure 5-3 depicts voltage-current density (V-j) curves for the developed SOFC model. The highlighted point on Figure 5-3 shows the voltage and current density of the BlueGEN system at steady state condition. The steady state performance parameters of the model and BlueGEN are listed in Table 5-4. Data in Table 5-4 show that the developed model is simulating the behavior of BlueGEN quite accurately. The exhaust temperature and exhaust mass flow rate of the system in steady state mode is $81℃$ and $0.0089\,\frac{\mathrm{Kg}}{\mathrm{s}}$ respectively.

Table 5-3. SOFC Parameters and Design Operating Condition

Parameters	Value
Power output	1.5kW
Power Density	$230\mathrm{mW/Cm^2}$
Fuel Utilization	0.85
Steam to Carbon Ratio	2
Total Cell Active Area	$34.81\mathrm{cm^2}$
Delta T Stack	50

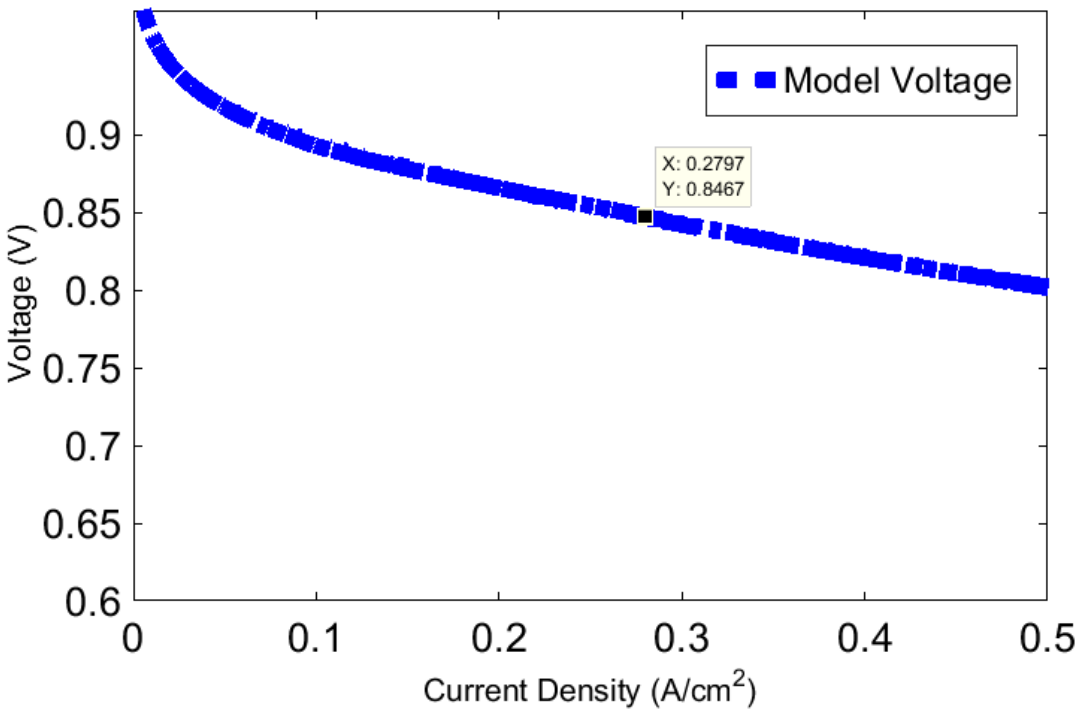

Figure 5-3: Voltage-Current Density Curve of BlueGEN Simulation Model

Table 5-4: Steady State Performance of SOFC

Parameter	Simulation model	BlueGEN
Operating Voltage	0.838V	0.833V
Current Density	$0.274 A/cm^3$	$0.28 A/cm^3$
Stack Efficiency	68.5%	69%

5.2.2. SOFC Model Verification with EnGen

The parameters and design operating conditions of the commercially available 2.5kW EnGen SOFC are listed in Table 5-5. Input parameters of the developed model are adjusted according to the operating conditions of the EnGen SOFC. Figure 5-4 depicts voltage-current density (V-j) curves for both the EnGen SOFC system and the developed model. As shown in Figure 5-4, the V-j curve obtained from the model follows the measured SOFC V-j curve accurately. The steady state performance parameters of the model for simulating this 2.5kW SOFC system are listed in Table 5-6. Note that the EnGen system only operates in a range of current density from about 0.25 to $0.50 A/cm^2$. The model well matches the performance in this entire range.

Table 5-5: SOFC Parameters and Design Operating Condition

Parameters	Value
Fuel Utilization	0.75
Steam to Carbon Ratio	2.2
Cell Area	$80cm^2$
Anode Thickness	240e-6m
Cathode Thickness	40e-6m
Electrolyte Thickness	8e-6m
SOFC Stack Average Temperature	1023K

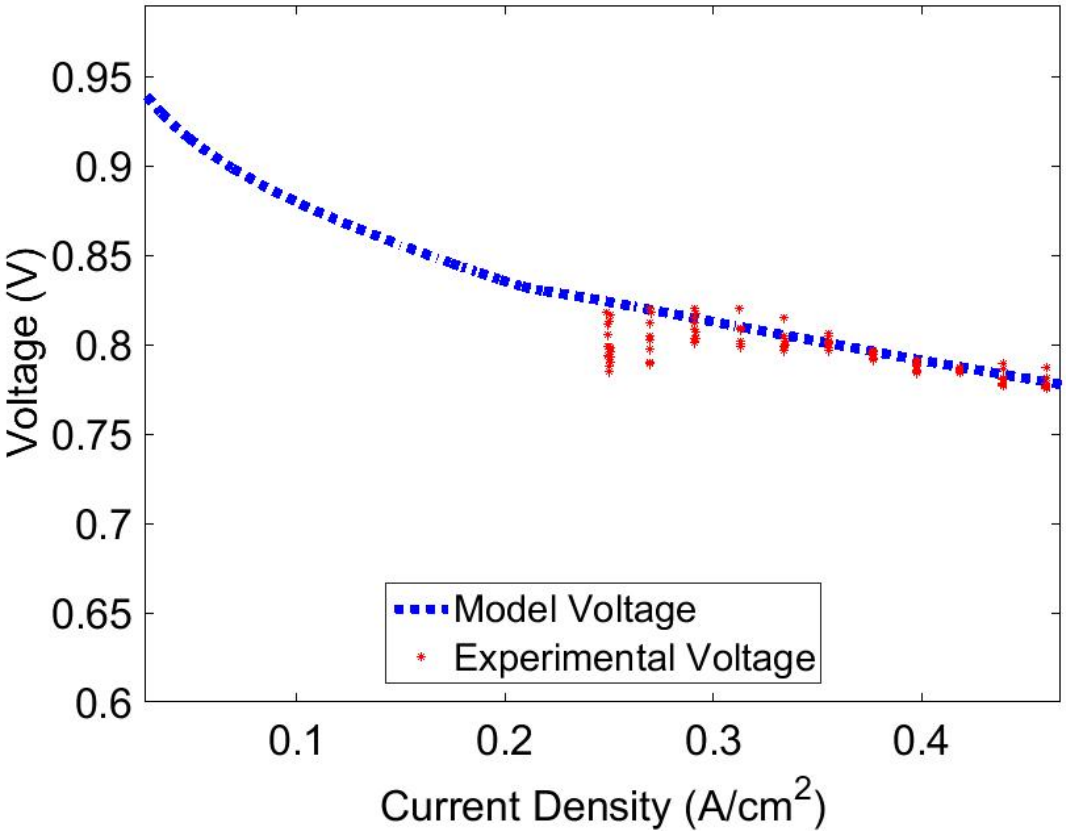

Figure 5-4: Comparison of SOFC model and experiment voltage

Table 5-6: SOFC Steady State Performance Parameters

Parameters	Value
Voltage	0.79V
Current Density	0.34A/cm^2
Electrical Efficiency	50%
Exhaust Gas Temperature	570K
Exhaust Gas Mass Flow Rate	0.0078Kg/sec

5.3. ORC Design

5.3.1. Overview

In order to dynamically model an ORC cycle, first of all, a complete ORC cycle should be designed based upon the desired outputs and the measured SOFC steady state working condition, called the nominal condition. In this study, a 400kW SOFC is used to meet Verano Place community demand (case used in this study). The designed unit is a 25kW ORC consisting of five key components: Evaporator, Expander, Condenser, Reservoir and Pump. Selection of the working fluid was found to be a constraining factor in the design. R245fa was selected due to its desirable performance and high safety. The heat source for the system is the SOFC exhaust gas. Heat is transferred to the working fluid in a shell and tube heat exchanger. Cooling is supplied to the shell and tube heat exchanger from the air supply. A scroll expander is used to extract work from the system.

5.3.2. Conceptual Design

5.3.2.1. Working Fluid

To further develop the conceptual design of the ORC system the potential working fluids need to be determined. The working fluid is a limiting factor in ORC design as it affects the

thermodynamic design and performance of all components within the system. The refrigerant also influences the required pressure rating and material type of all components in the system. R245fa is selected due to its desirable performance and high safety. The refrigerant offers several benefits over water, such as the lower boiling temperature at condenser working pressure based upon pressure-temperature space in liquid-gas phase diagram. This is beneficial to the system performance as it means the vapor flowing through the turbine is not a wet mixture. Table 5-7 presents the thermo-physical properties of R245fa.

Table 5-7: Critical Properties of R245fa

Molecular Formula	$CF_3CH_2CHF_2$
Molecular Weight	$134.05 g/mol$
Critical Pressure	$3640 kPa$
Critical Temperature	$427.2 K$
Critical Density	$517 kg/m^3$

5.3.2.2. Evaporator

An annularly high finned shell and tube heat exchanger is typically used as the evaporator for this size of ORC system. Figure 5-5 schematically shows the evaporator concept used in the current ORC cycle.

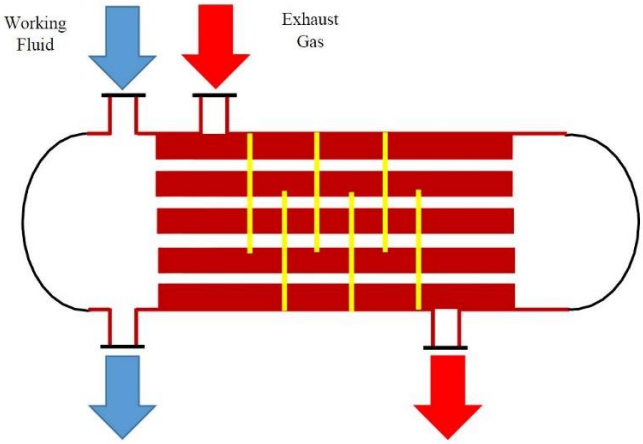

Figure 5-5: Schematic View of the Evaporator

Table 5-8 shows the physical properties of the SOFC exhaust gas.

Table 5-8: SOFC Exhaust Gas Properties

Specific Heat Capacity (C_p)	874.5[J/kgK]
Thermal Conductivity (k)	0.0414[W/m.K]
Dynamic Viscosity (μ)	2.8e-5[Pa.s]
Prandtl number (Pr)	0.59

For a 400kW SOFC which is used as a case study in this study, the designed mass flow rates, temperatures and pressures of SOFC exhaust gas and working fluid are depicted in Table 5-9. Exhaust gas energy is recuperated in an ORC cycle which is a bottoming cycle of the SOFC.

Table 5-9: Fluid States in the Evaporator

Exhaust Gas Mass Flow Rate	1.269[kg/s]
Exhaust Gas Inlet Temperature	592.2[K]
Exhaust Gas Outlet Temperature	343.5[K]
Working Fluid Mass Flow Rate	1[kg/s]
Working Fluid Inlet Temperature	309.85K
Working Fluid Outlet Temperature	422.87K
Working Fluid Pressure	2212kPa

The evaporator is sized using thermodynamic calculations for heat transfer. Table 5-10 shows the geometric parameters of the designed evaporator.

Table 5-10: The Designed Evaporator Geometric Parameters

Evaporator Height	0.87(m)
Evaporator Width	1.84(m)
Evaporator Depth	0.87(m)
Tube Inner Diameter (D_i)	0.02(m)
Tube Outer Diameter (D_o)	0.025(m)
Horizontal Spacing	0.084(m)
Vertical Spacing	0.084(m)
Fin Spacing (Y)	0.007(m)
Fin Height (H)	0.015(m)
Number of Tubes per Row (N_L)	8
Number of Tubes per Column (N_T)	8
Number of Baffles	8

Figure 5-6, Figure 5-7 and Figure 5-8 show the designed evaporator.

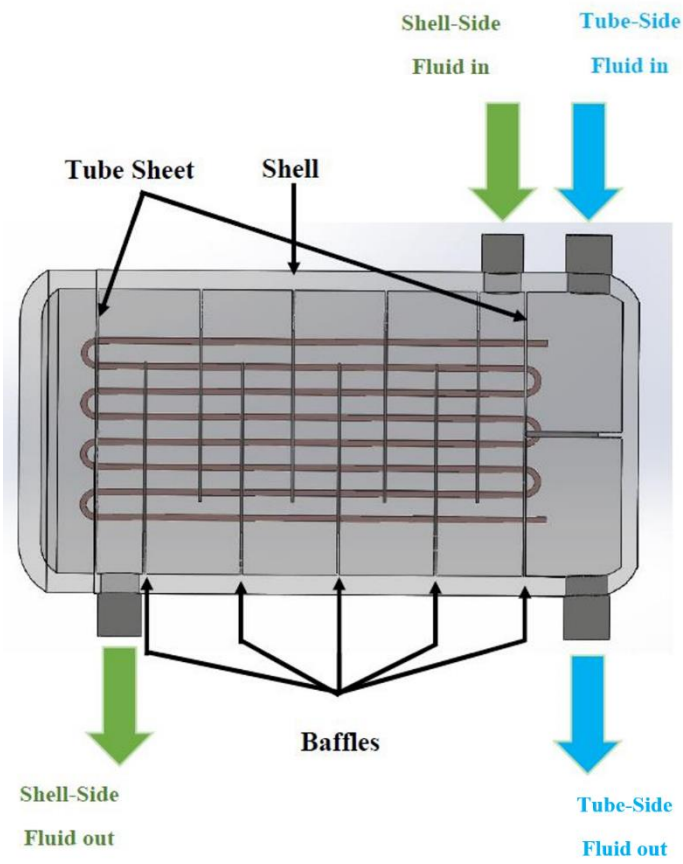

Figure 5-6: The Designed Evaporator and fluids' path

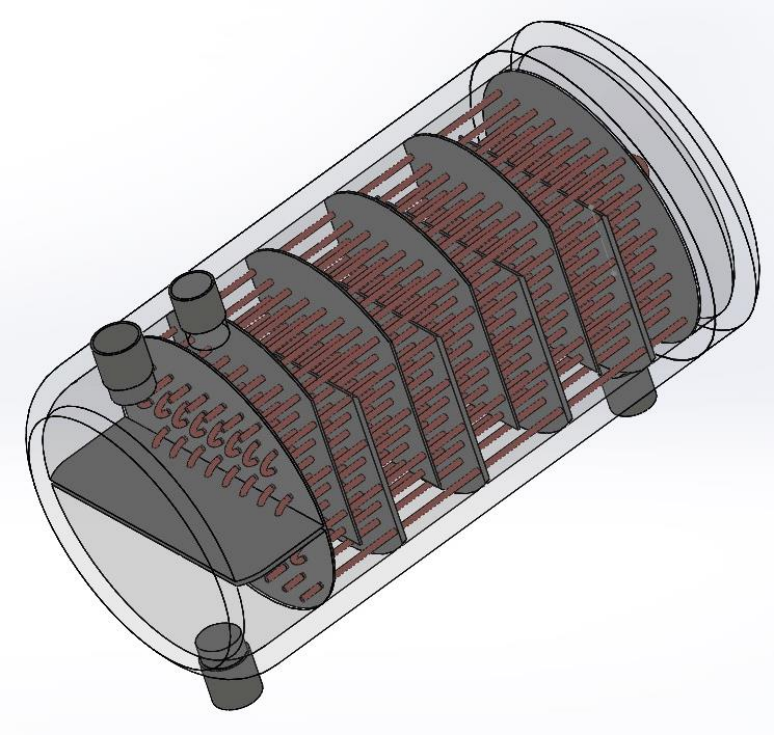

Figure 5-7: 3-D View of the Designed Evaporator

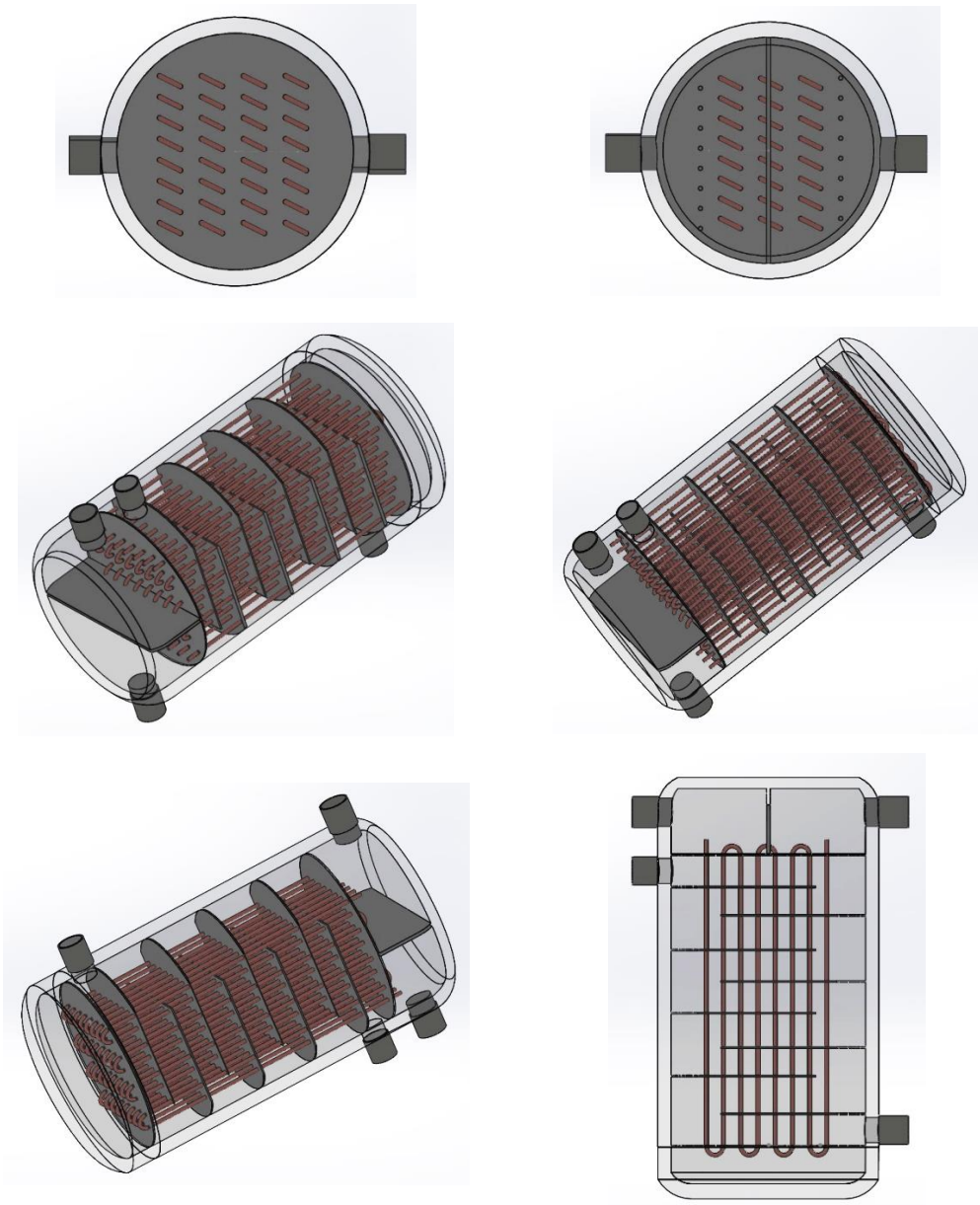

Figure 5-8: Different Views of the Designed Evaporator

5.3.2.3. Expander

The expander (or turbine) is typically the most costly component in an ORC system as it needs to be precision engineered. The turbine is the most vital element in an ORC system as it allows work to be extracted from the fluid energy via an expansion process. The energy is converted to mechanical shaft energy which is finally converted into electricity by an electrical generator. The turbine needs to be selected carefully to maintain optimum system efficiency. A scroll expander is

used to extract work from the system. The expansion process is modeled by dividing the expander into two steps: Isentropic expansion and constant volume expansion following the method of Zhang et al. [53]. Figure 5-9 schematically shows expander in the ORC cycle.

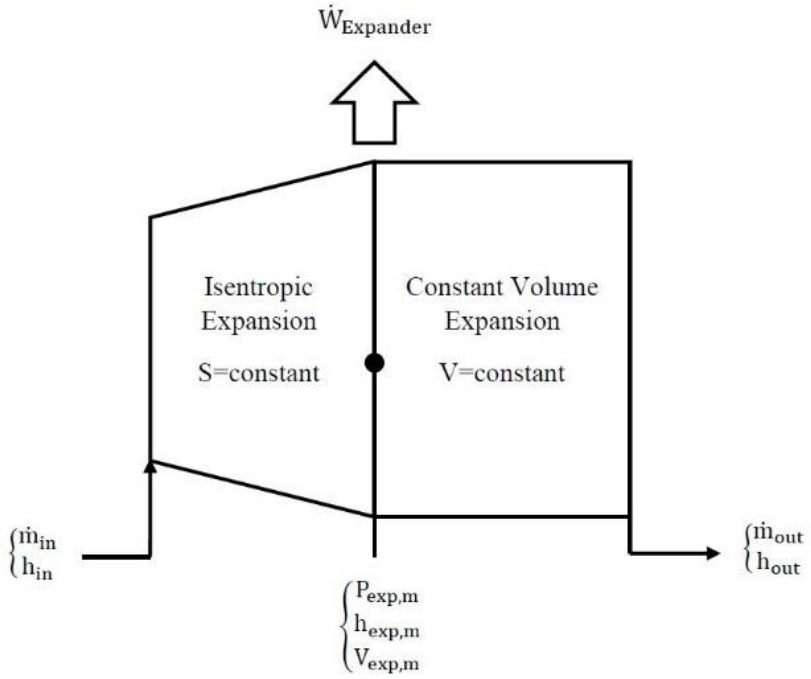

Figure 5-9: Schematic View of the Expander

Table 5-11 presents the mass flow rate, enthalpy, specific volume, pressure and other specifications of the designed expander and the working fluid inside it.

Table 5-11: Working Fluid State Parameters and Expander Specifications

Working Fluid Mass Flow Rate	1[kg/s]
Working Fluid Inlet Enthalpy	512.89[kJ/kg]
Working Fluid Inlet Pressure	2212[kPa]
Working Fluid Inlet Temperature	422.87[K]
Working Fluid Inlet Specific Volume	0.0088[m^3/kg]
Working Fluid Pressure in the Middle of two Steps	347.56[kPa]
Working Fluid Specific Volume in the Middle of two Steps	0.0438[m^3/kg]
Working Fluid Outlet Enthalpy	493.49[kJ/kg]
Working Fluid Outlet Pressure	263.9[kPa]
Working Fluid Outlet Temperature	372.67[K]
Expander Efficiency	0.8

5.3.2.4. Condenser

An annularly high finned shell and tube heat exchanger is typically used as a condenser for this size of ORC system. Figure 5-10 schematically shows the condenser used in the current ORC cycle.

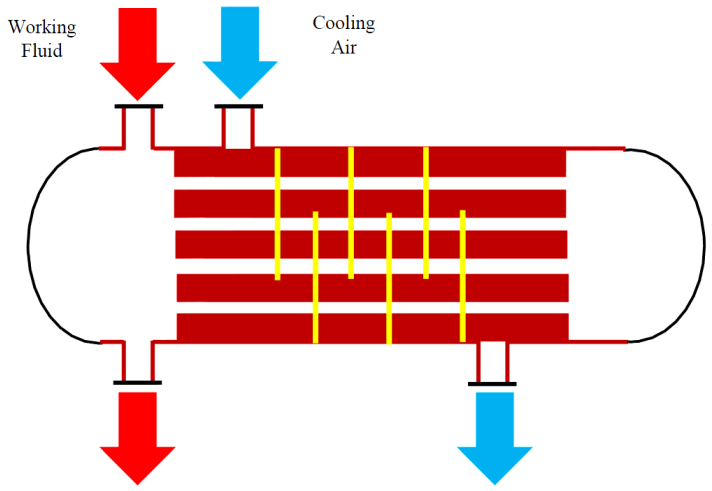

Figure 5-10: Schematic View of the Condenser

Table 5-12 shows the physical properties of cooling air.

Table 5-12: Cooling Air Properties

Specific Heat Capacity (C_p)	1.0064[kJ/kgK]
Thermal Conductivity (k)	0.0256[W/m.K]
Dynamic Viscosity (μ)	1.8248e-5[Pa.s]
Prandtl number (Pr)	0.71

The designed mass flow rates, temperatures and pressures of cooling air and working fluid are depicted in Table 5-13.

Table 5-13: Fluids' States in Condenser

Cooling Air Mass Flow Rate	18[kg/sec]
Cooling Air Inlet Temperature	298[K]
Cooling Air Outlet Temperature	311.6[K]
Working Fluid Mass Flow Rate	1[kg/sec]
Working Fluid Inlet Temperature	372.67[K]
Working Fluid Pressure	263.9[kPa]

The condenser is sized using thermodynamic calculations for heat transfer. Table 5-14 shows the geometric parameters of the designed condenser.

Table 5-14: The Designed Condenser's Geometric Parameters

Evaporator Height	1(m)
Evaporator Width	2.08(m)
Evaporator Depth	1(m)
Tube Inner Diameter (Di)	0.02(m)
Tube Outer Diameter (Do)	0.025(m)
Horizontal Spacing	0.075(m)
Vertical Spacing	0.075(m)
Fin Spacing (Y)	0.007(m)
Fin Height (H)	0.015(m)
Number of Tubes per Row (NL)	10
Number of Tubes per Column (NT)	10
Number of Baffles	10

Figure 5-11, Figure 5-12 and Figure 5-13show the designed condenser.

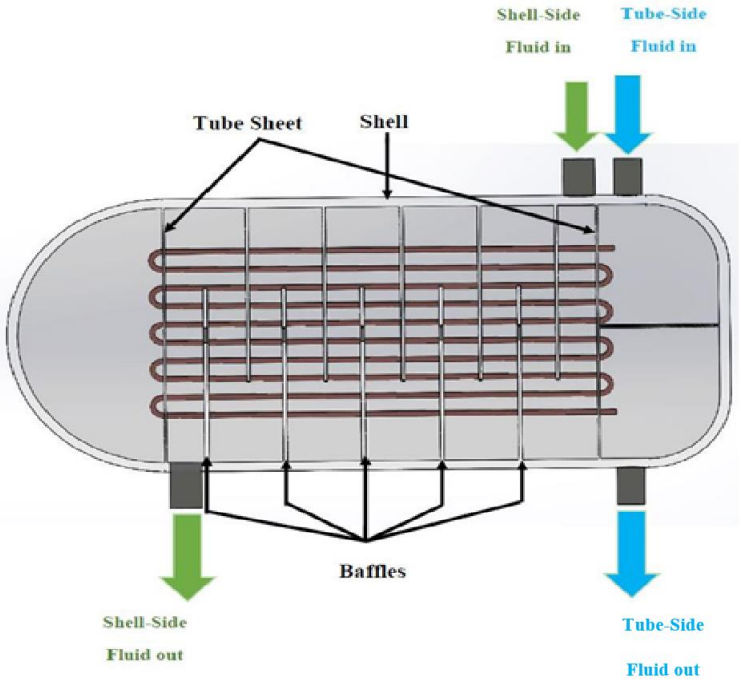

Figure 5-11: The Designed Condenser and fluids' path

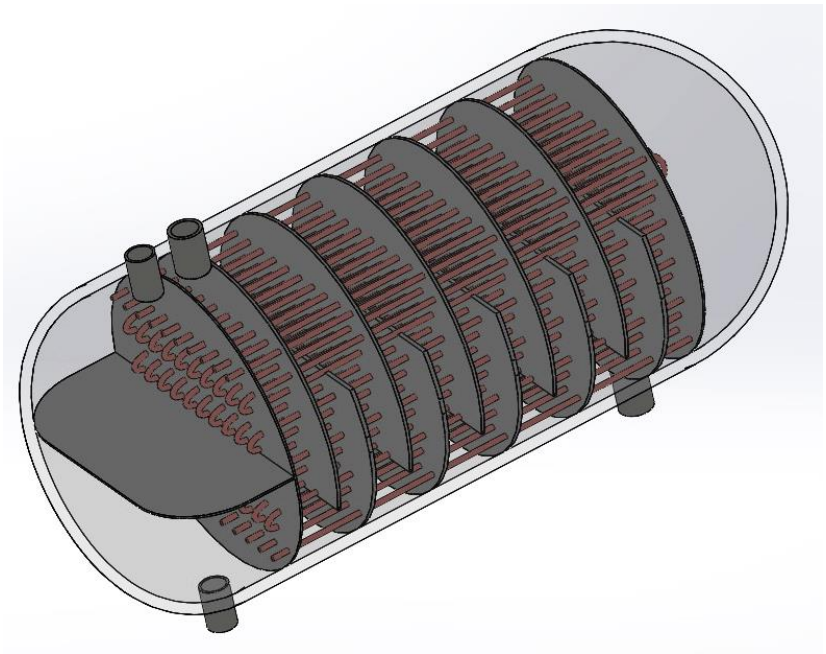

Figure 5-12: 3-D View of the Designed Condenser

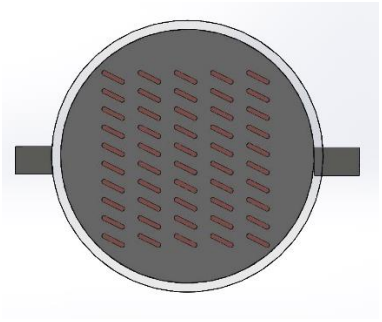

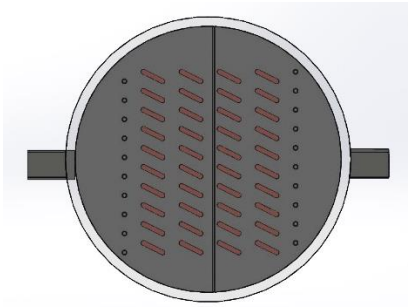

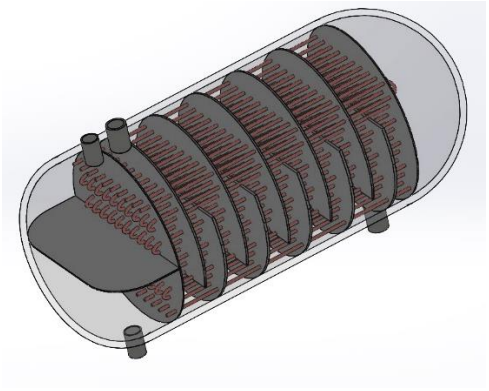

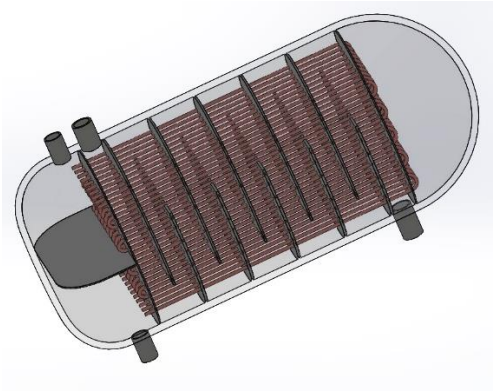

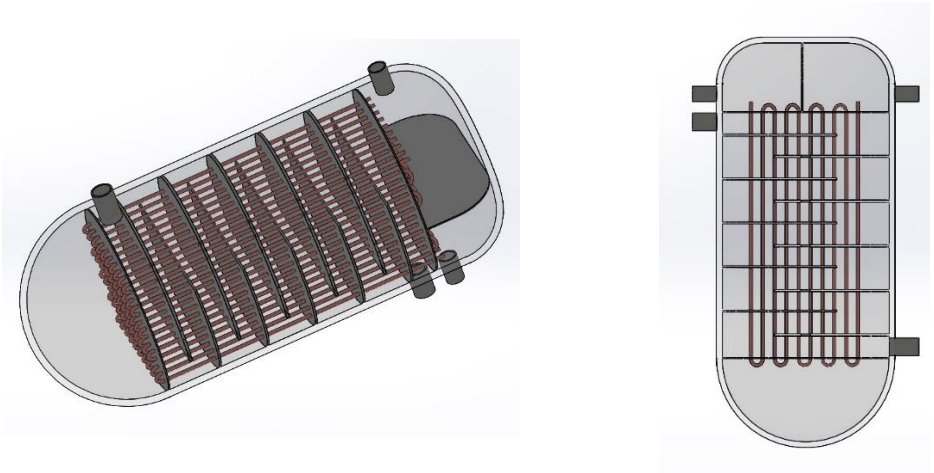

Figure 5-13: Different Views of the Designed Condenser

5.3.2.5. Pump

The ORC feed pump is used to provide the evaporator with a constant supply of liquid. Typically a centrifugal pump would be used in a large scale ORC as the flow and pressure requirements could easily be matched.

Table 5-15 presents the mass flow rate, enthalpy, pressure and other specifications of the designed pump and the working fluid inside it.

Table 5-15: Working Fluid State Parameters and pump Specifications

Working Fluid Mass Flow Rate	1[kg/s]
Working Fluid Inlet Pressure	263.9[kPa]
Working Fluid Outlet Enthalpy	248.62[kJ/kg]
Working Fluid Outlet Pressure	2212[kPa]
Working Fluid Outlet Temperature	309.85[K]
Pump Efficiency	0.82

5.4. Organic Rankine Cycle Dynamic Model Verification

In order to verify the developed dynamic model, the dynamic input data (exhaust gas mass flow rate and exhaust gas temperature) of the Zhang et al. study are used [53]. In this article, Zhang et al. used two different distributions for exhaust gas mass flow rate and exhaust gas temperature. Both of these two different input data are used to verify the developed dynamic model in our study.

As the organic Rankine cycle in the mentioned article was designed for a nominal operating condition different than the current study, both the exhaust gas mass flow rate and temperature dynamic variation around its nominal condition should be scaled around the nominal condition of the designed organic Rankine cycle in this study and then they should be used as input disturbances for the developed ORC dynamic model. The obtained output power, pump rotational speed and expander rotational speed in this study should be scaled and then compared to those one in [53] to see how well the results compare to those produced by the current dynamic model.

5.4.1. Reference Used for Verification of Dynamic Model of Organic Rankine Cycle

Zhang et al. [53] developed a dynamic model for an Organic Rankine Cycle which is shown in Figure 5-14 which is based upon a moving boundary method for the evaporator and condenser. It used a proposed generalized predictive control to enable the cycle to deeply utilize waste heat and keep the process variables within safe operating limits, simultaneously. In order to deeply recover the waste heat, the cycle adapts to the variations of the heat source temperature and flow rate while the developed control strategies ensure that the ORC process variables are maintained within appropriate ranges.

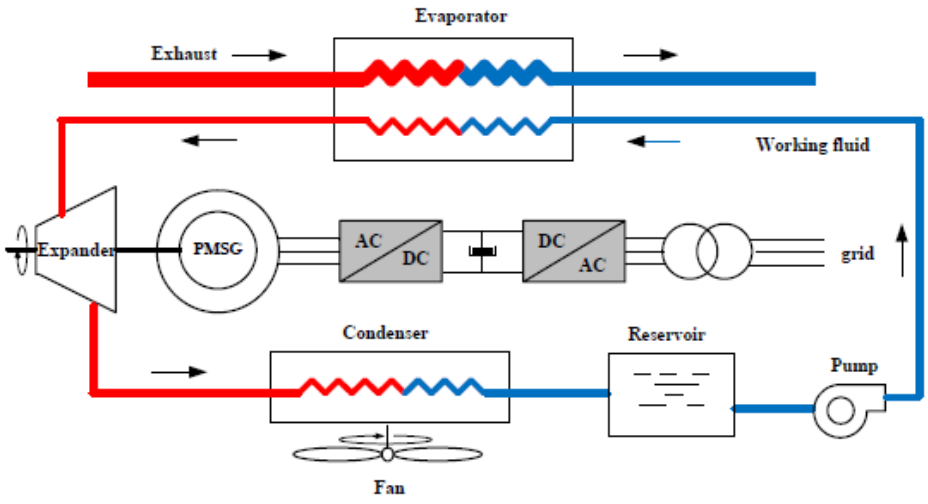

Figure 5-14: Organic Rankine Cycle Used in [53]

The nominal operating conditions in [53] are listed in Table 5-16.

Table 5-16: The Nominal Operating Condition in [6]

$\mathbf{P_c}$	255kPa
$\mathbf{P_e}$	2000kPa
$\mathbf{\dot{m}_{exhaus\ gas}}$	7.44kg/s
$\mathbf{T_{exhaus\ gas,i}}$	573K
$\mathbf{T_{exhaus\ gas,o}}$	353K
$\mathbf{\dot{m}_{cooling\ air}}$	7.44kg/s
$\mathbf{N_{pump}}$	2850r/min
$\mathbf{N_{expander}}$	1500r/min
$\mathbf{T_{su}}$	17K
Power	100kW

5.4.2. First Scenario Used for Verification

The first disturbance scenario (exhaust gas mass flow rate and temperature) used in [53] is shown in Figure 5-15. As it is obvious in this figure, in the first part (0 to 500s), only the variation of exhaust temperature is taken into account while exhaust mass is considered to have its nominal value. In the second part (500 to 1000s) of this figure, exhaust temperature is considered to be constant and variation of exhaust mass is investigated. And, in the last part (1000 to 1500s) variation of both exhaust temperature and mass are taken into account and their effects on the output power and other manipulated parameters are investigated simultaneously.

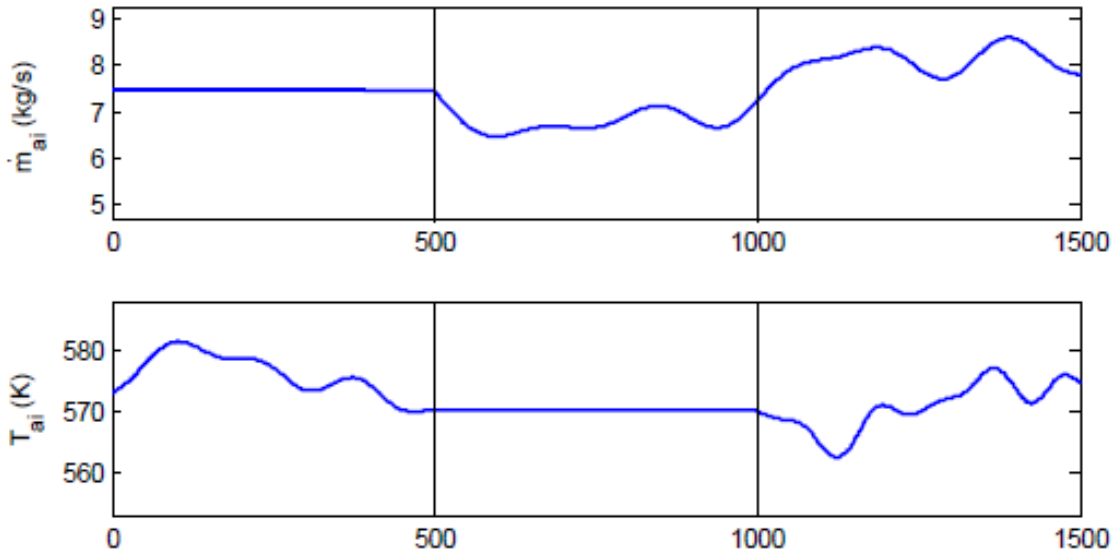

Figure 5-15: Fluctuation of Waste Heat in the First Scenario Plotted Versus Time in Seconds (s) [53]

Exhaust gas mass flow rate and exhaust gas temperature variation versus time should be captured from Figure 5-15 and used as input disturbances to validate our developed dynamic model. The Get-Data Graph Digitizer software was implemented to capture the required data from Figure 5-15.

The effect of the considered disturbance (Figure 5-15) on the Zhang et al. ORC model output power is presented as Figure 5-16 [53].

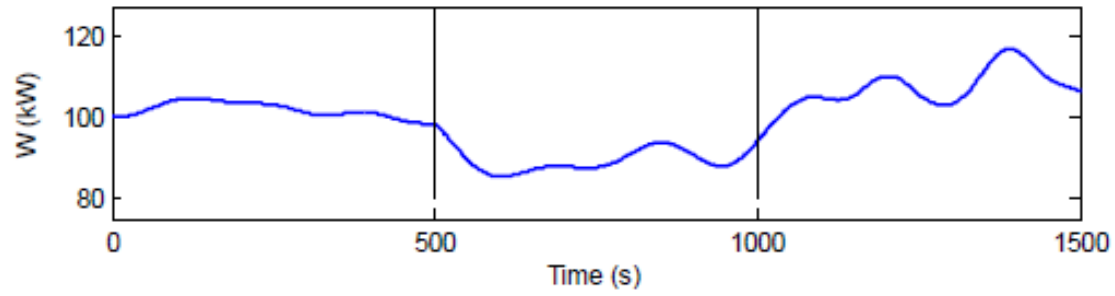

Figure 5-16: Variation of Output Power in the First Scenario Plotted Versus Time in Seconds (s) [53]

Manipulated variables (pump rotational speed, expander rotational speed and mass flow rate of cooling air) are obtained from [53] and presented in Figure 5-17.

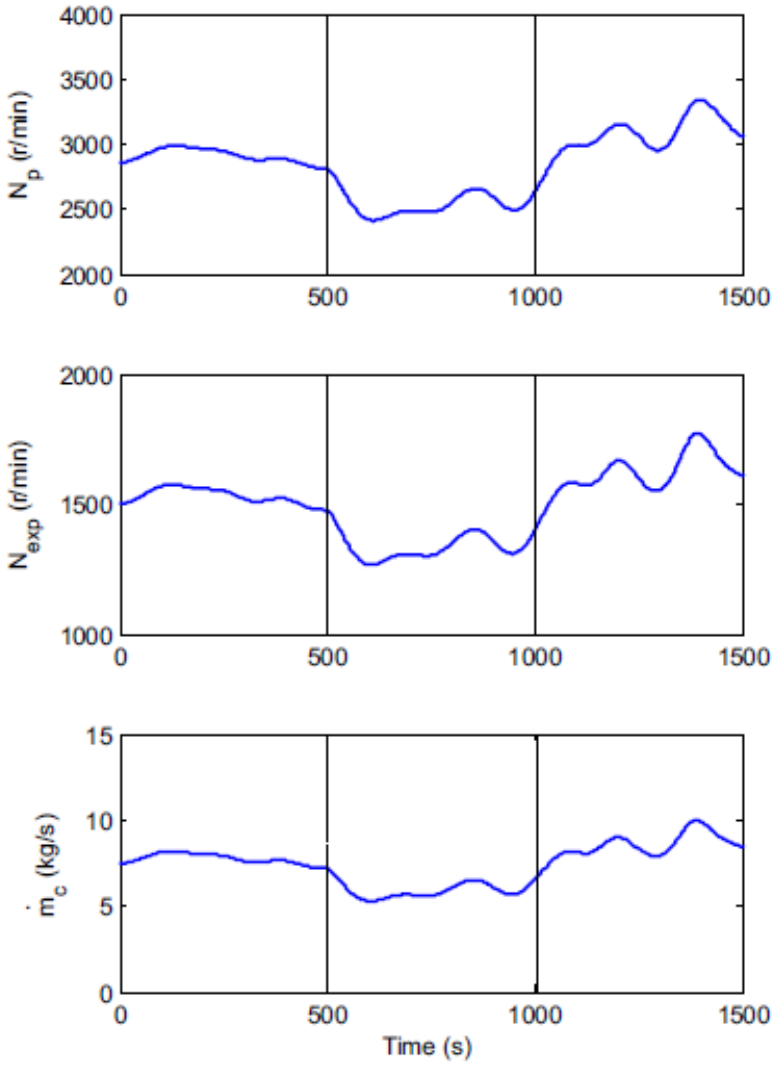

Figure 5-17: Variation of Manipulated Variables in the First Scenario [53]

5.4.2.1. Scaling of the Disturbance

As it was said, the disturbance used in [53] should be scaled based upon the nominal operating conditions (design parameters) used in this study. Figure 5-18 depicts the scaled disturbance which should be used to verify the proposed dynamic model in this study with the results in [53].

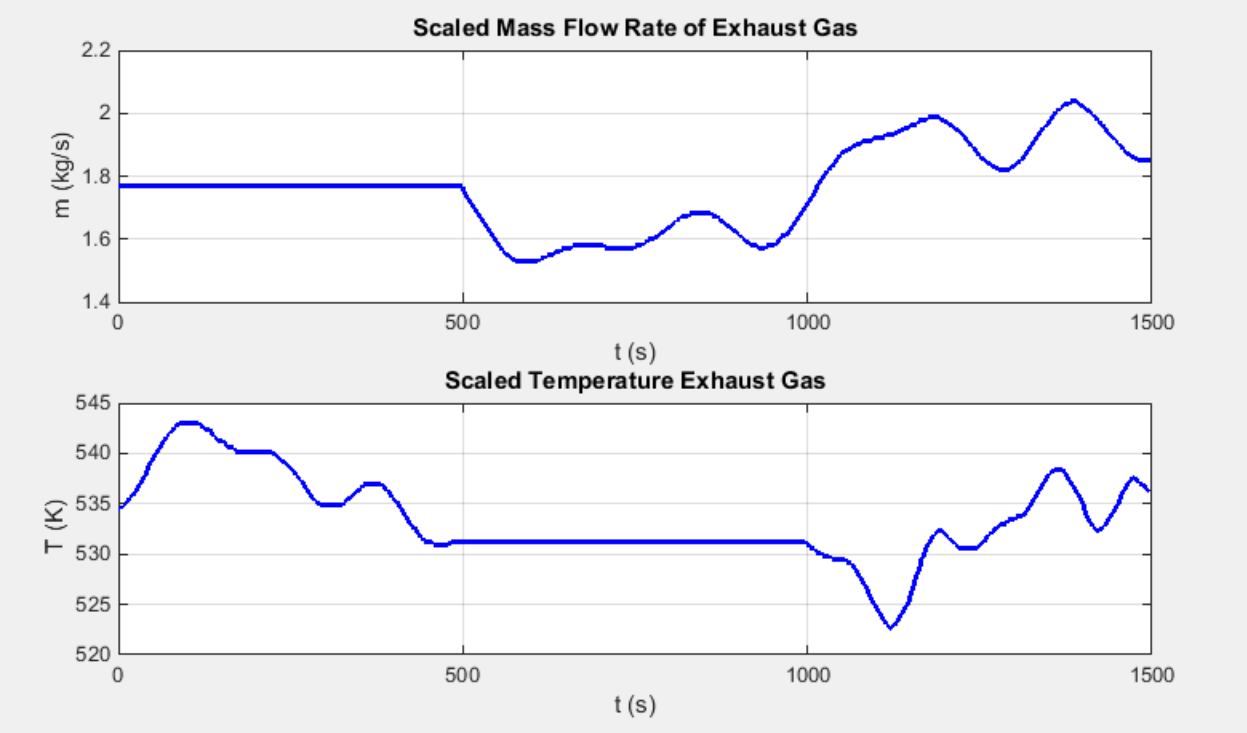

Figure 5-18: The Scaled Disturbance in the First Scenario

5.4.2.2. Verification Results

The developed dynamic model uses the disturbance in Figure 5-18 as its input and the output power is captured. The captured output power is scaled based upon the nominal output power in [53]. Figure 5-19 shows both the variation of output power in [53] and the scaled variation of output power obtained from the current dynamic model. The percentage root mean square error (%RMSE) is only 1.41%.

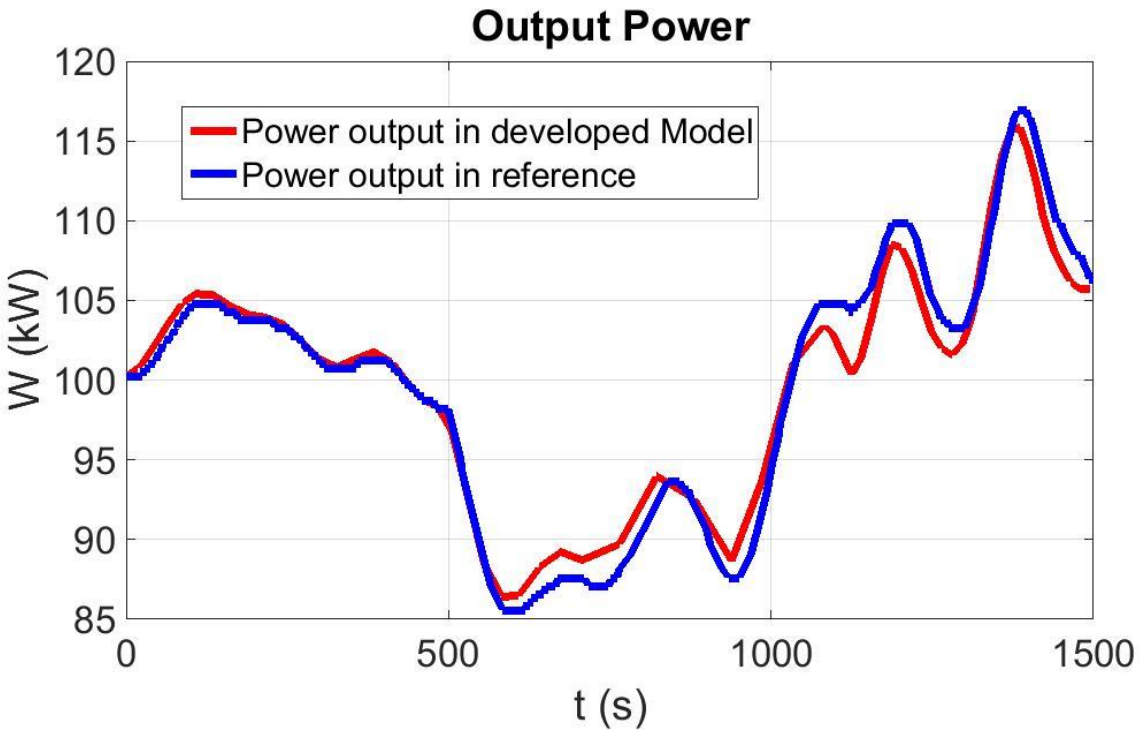

Figure 5-19: Compatibility of Output Work Variation in This Study and [53] in the First Scenario

As it can be seen, the variation of the obtained power is highly compatible with the results shown in [53]. The presented small differences are likely due to the differences in the two dynamic models (e.g., moving boundary versus bulk models for the evaporator and condenser) and the control system that is used in [53].

Figure 5-20 and Figure 5-21 present the variation of both pump rotational speed and expander rotational speed in the used reference [53] and the scaled ones which are obtained from our dynamic model. As shown in these figures, these obtained rotational speeds are as compatible as the output power data of [53].

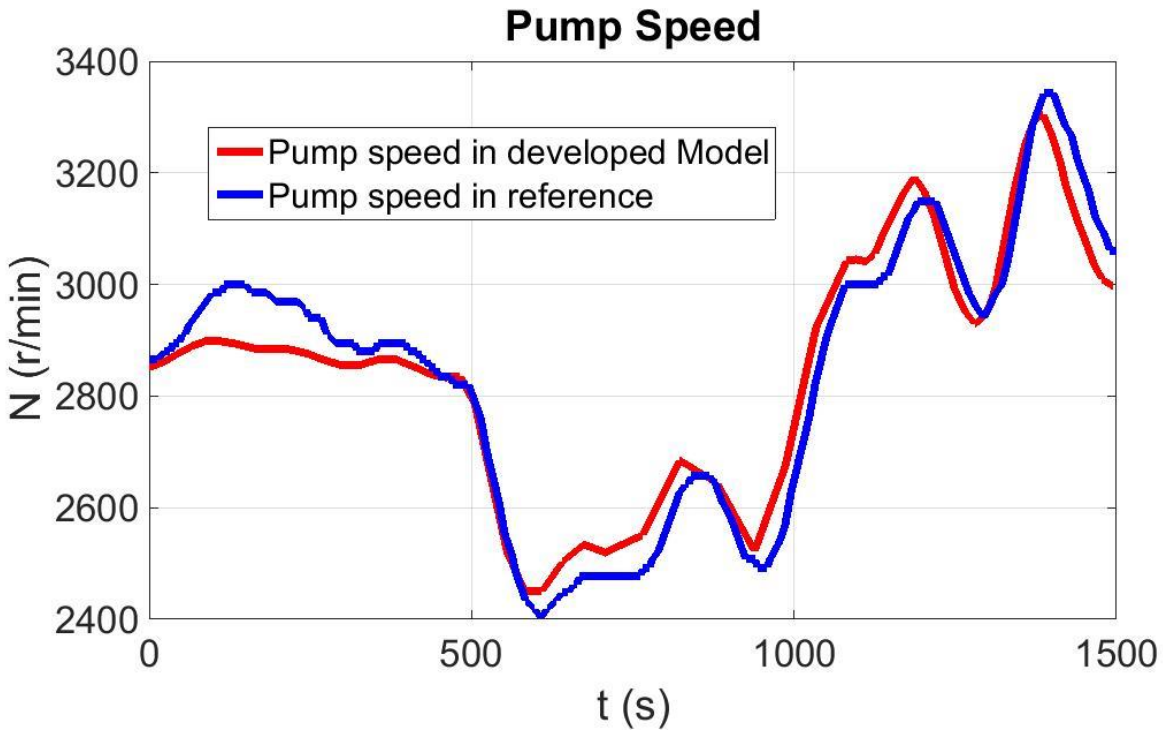

Figure 5-20: Compatibility of Pump Rotational Speed Variation in This Study and [53] in the First Scenario

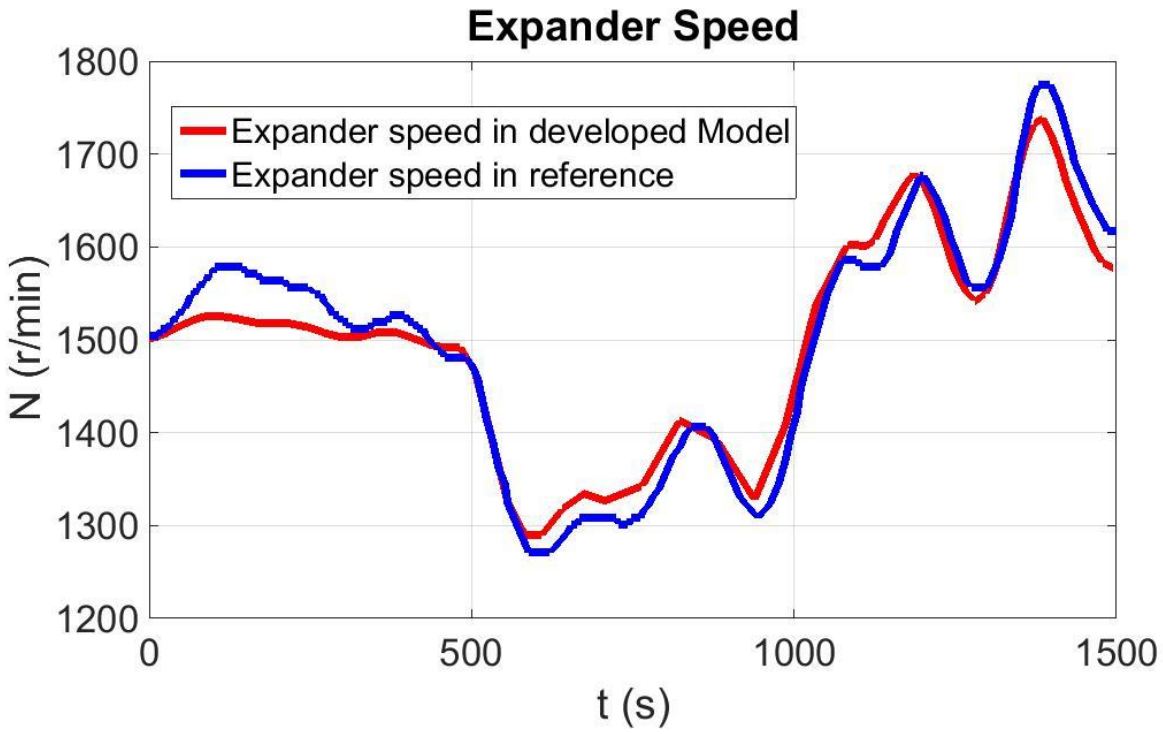

Figure 5-21: Compatibility of Expander Rotational Speed Variation in This Study and [53] in the First Scenario

Figure 5-22 shows the variation of mass flow rate of cooling air in the used reference [53] and the scaled one which is obtained from our dynamic model. As shown in this figures, the obtained mass flow rate of cooling air is quite compatible with the one in [53], although the match is not as good as that associated with the other dynamic operating parameters shown.

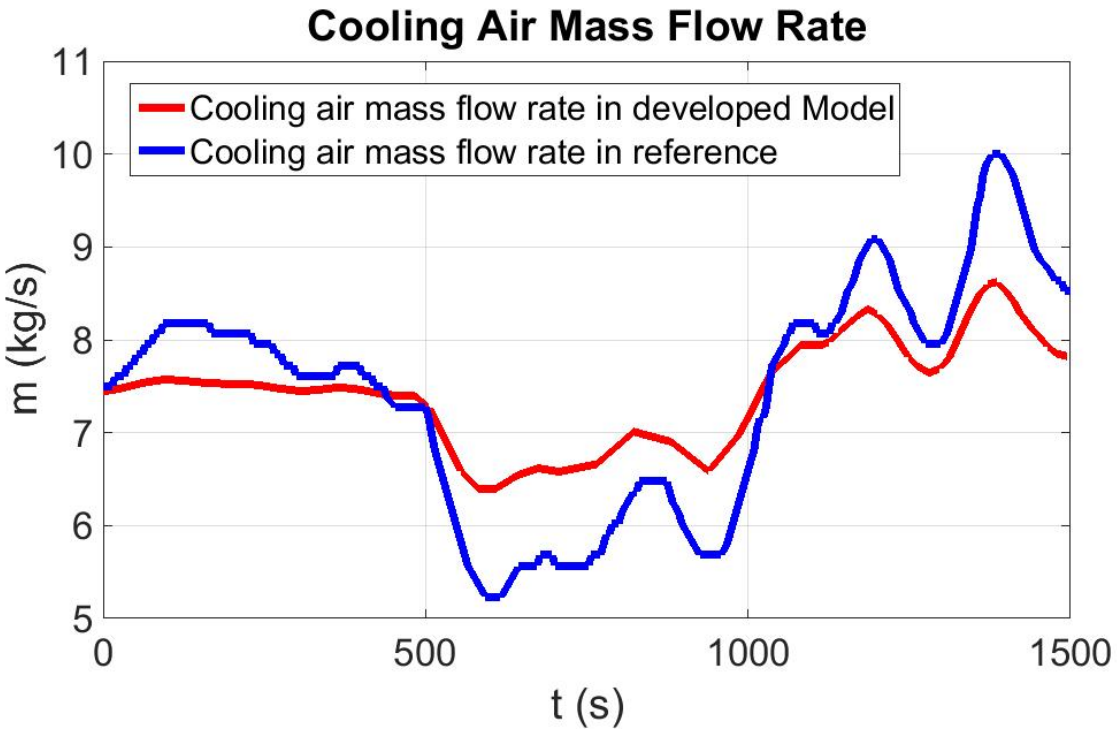

Figure 5-22: Compatibility of Mass Flow Rate of Cooling Air Variation in This Study and [53] in the First Scenario

5.4.3. Second Scenario Used for Verification

The data associated with the second disturbance scenario (exhaust gas mass flow rate and temperature) used in [53] are presented in Figure 5-23.

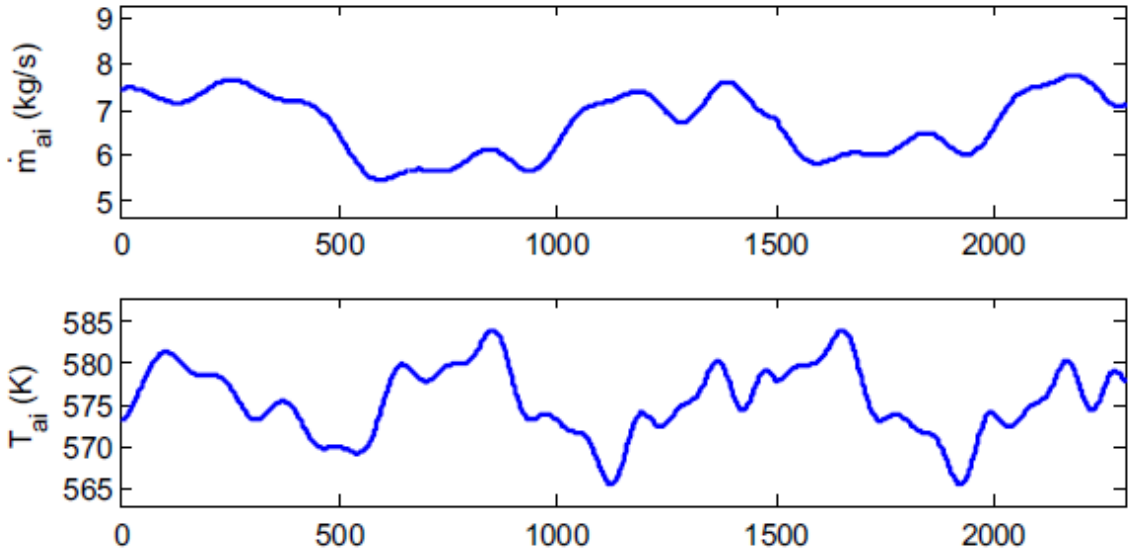

Figure 5-23: Fluctuation of Waste Heat in the Second Scenario Plotted Versus Time in Seconds (s) [53]

Exhaust gas mass flow rate and exhaust gas temperature variation versus time should be captured from Figure 5-23 and used as an input disturbance to validate our developed dynamic model. The Get-Data Graph Digitizer software is implemented to capture the required data from Figure 5-23.

The effect of the considered disturbance (Figure 5-23) on the ORC output power is presented as Figure 5-24 [53].

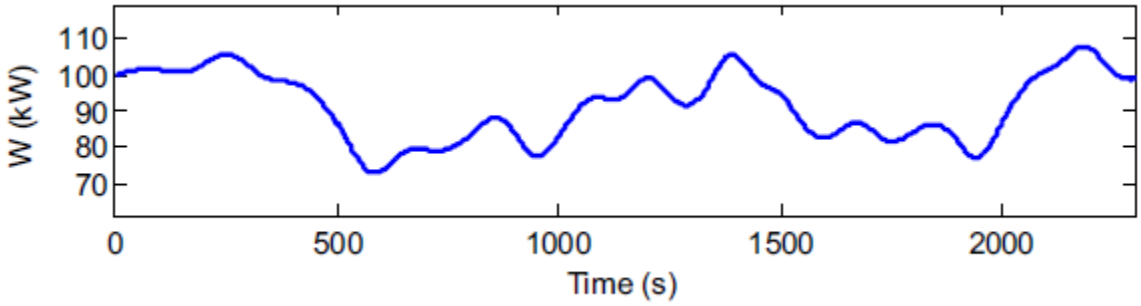

Figure 5-24: Variation of Output Power in the Second Scenario [53]

Manipulated variables (pump rotational speed, expander rotational speed and mass flow rate of cooling air) are obtained from [53] as presented in Figure 5-25.

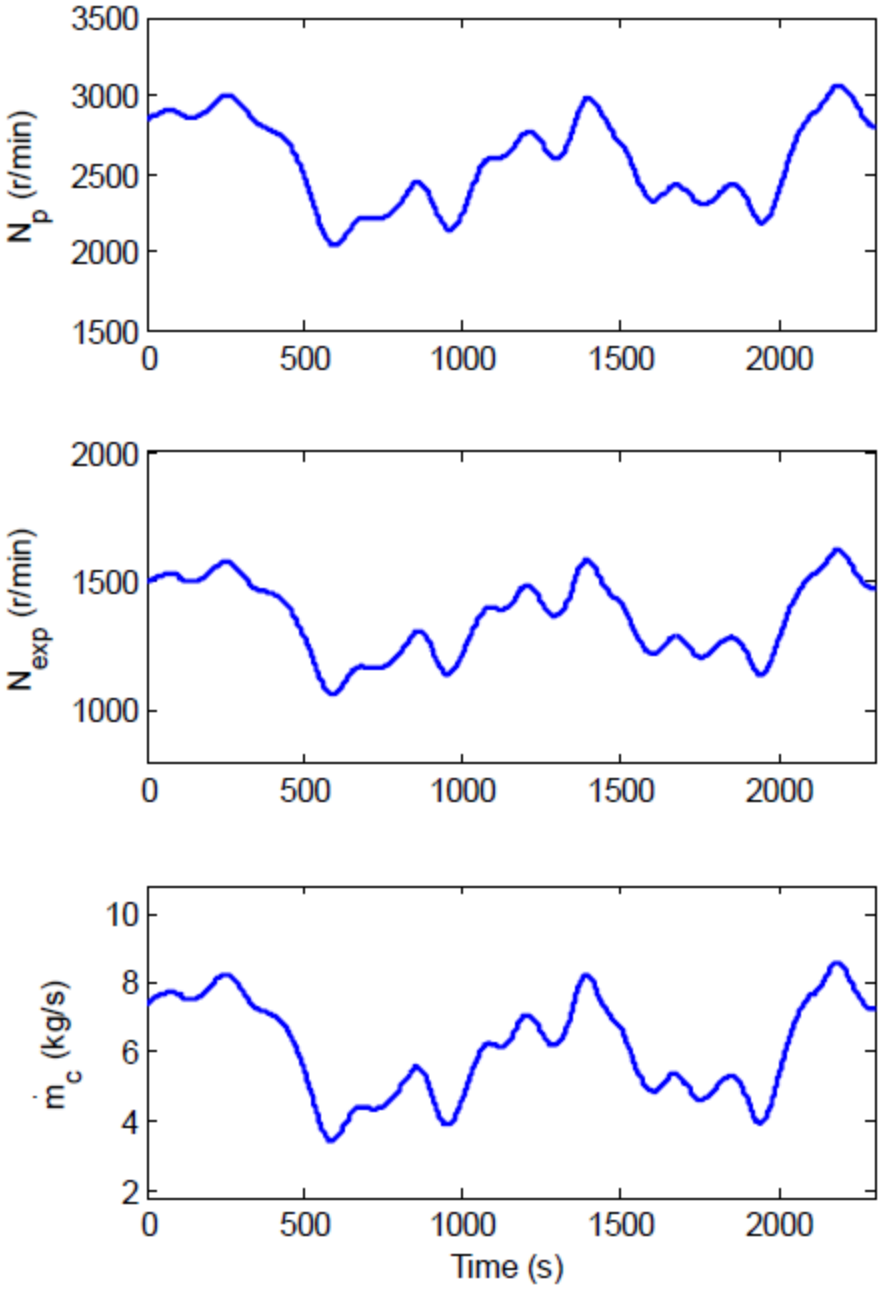

Figure 5-25: Variation of Manipulated Variables in the Second Scenario [53]

5.4.3.1. Scaling Disturbance

As it was said, the disturbance used in [53] should be scaled based upon the nominal operating conditions (design parameters) used in this study. Figure 5-26 depicts the scaled disturbance which should be used to verify the proposed dynamic model in this study with the results in [53].

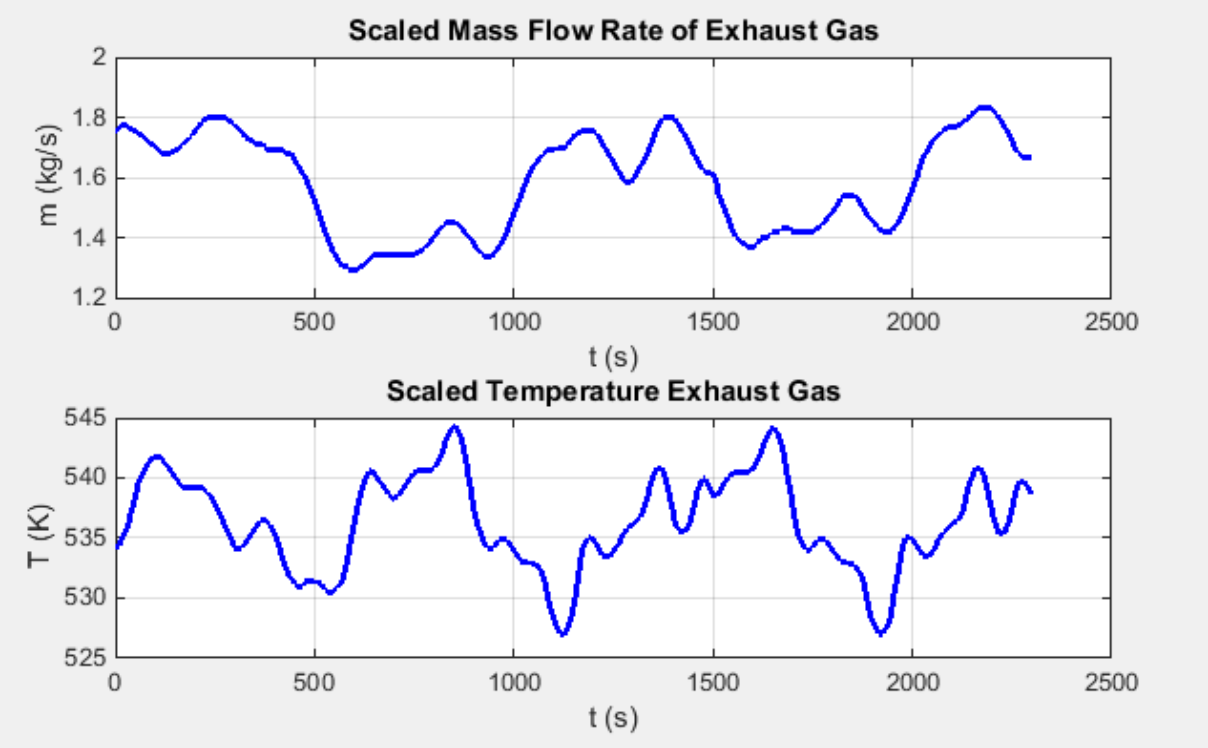

Figure 5-26: The Scaled Disturbance in the Second Scenario

5.4.3.2. Verification Result

The developed dynamic model uses the disturbance in Figure 5-26 as its input and the output power is captured. The captured output power is scaled base on the nominal output power in [53]. Figure 5-27 shows both the variation of output power in [53] and the scaled variation of output power obtained from our proposed dynamic model. The percentage root mean square error (%RMSE) is only 1.49%.

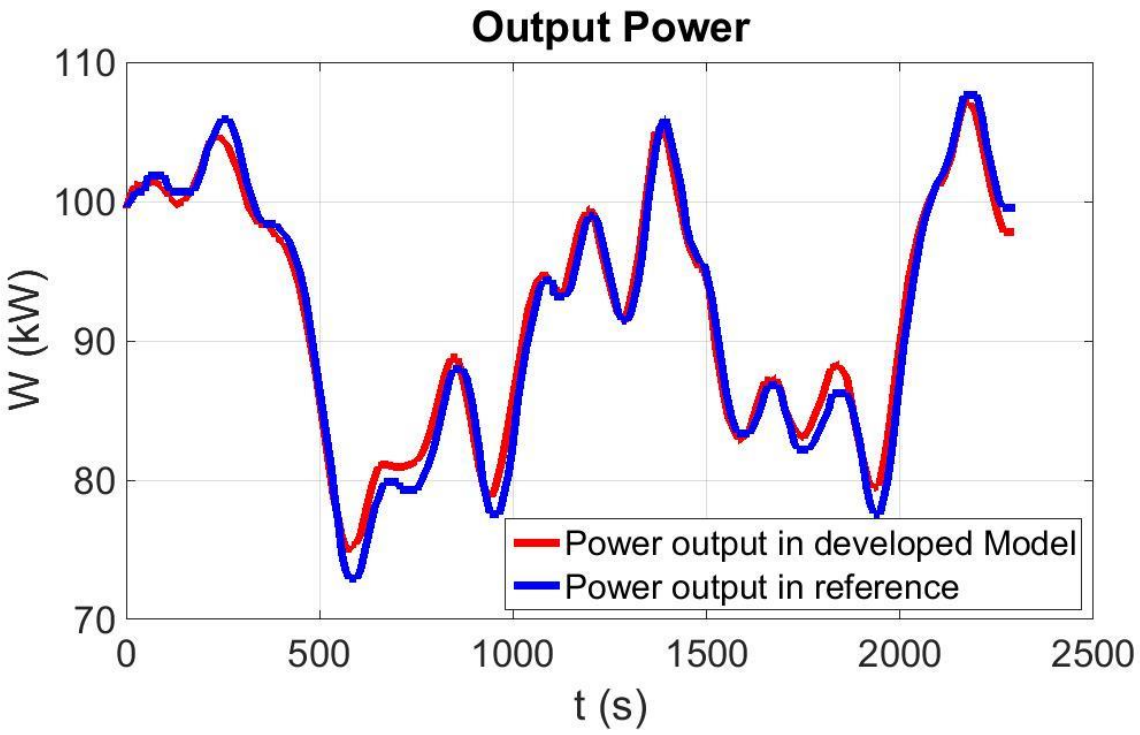

Figure 5-27: Compatibility of Output Work Variation in This Study and [53] in the Second Scenario

As it can be seen, the variation of the obtained power is highly compatible with the results shown in [53]. The presented small differences are likely due to the differences in the two dynamic models dynamic model (e.g., moving boundary versus bulk models for the evaporator and condenser) and the control system which is used in [53].

Figure 5-28 and Figure 5-29 present the variation of both pump rotational speed and expander rotational speed in the used reference [53] and the scaled ones which are obtained from our dynamic model. As shown in these figures, these obtained rotational speeds are as compatible as the output power data presented in [53].

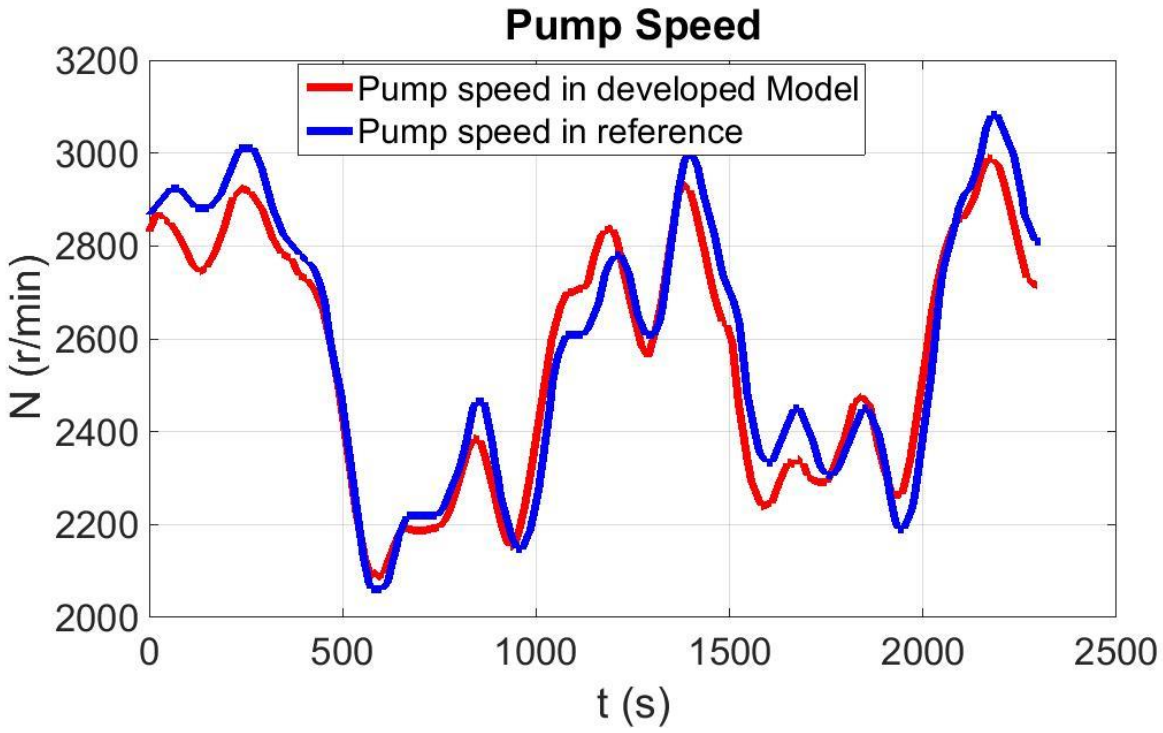

Figure 5-28: Compatibility of Pump Rotational Speed Variation in This Study and [53] in the Second Scenario

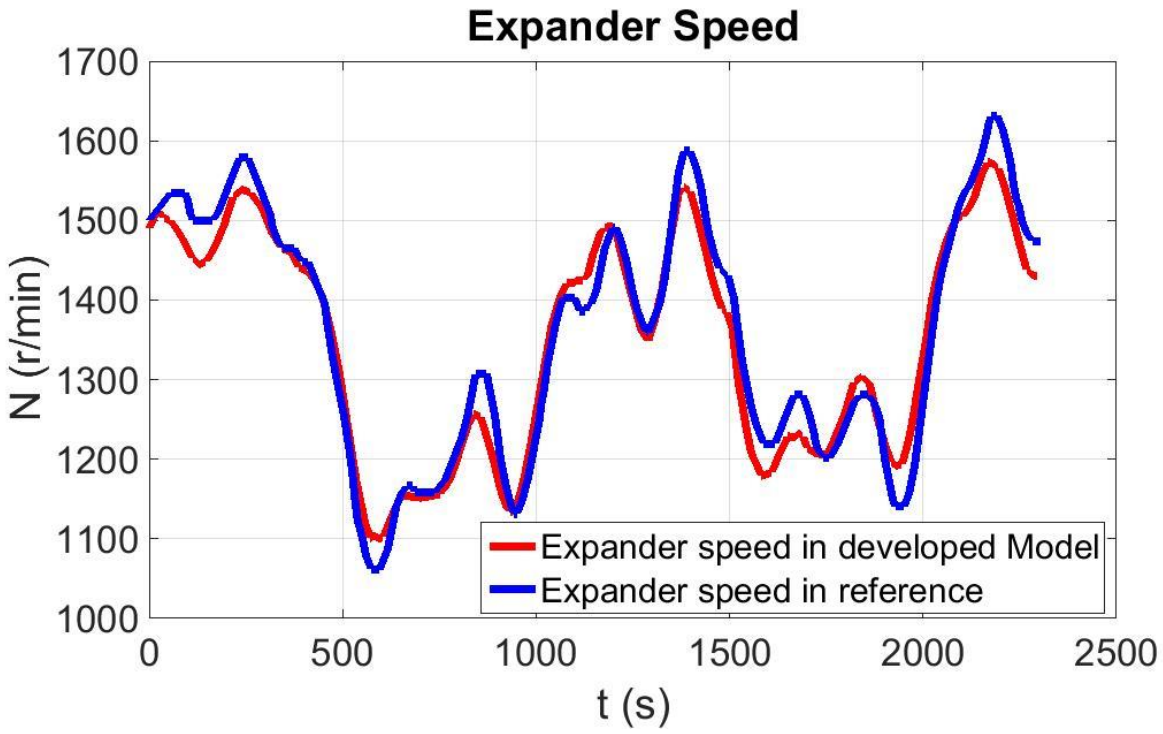

Figure 5-29: Compatibility of Expander Rotational Speed Variation in This Study and [53] in the Second Scenario

Figure 5-30 shows the variation of mass flow rate of cooling air in the used reference [53] and the scaled one which is obtained from our dynamic model. As shown in this figures, the obtained mass flow rate of cooling air is quite compatible with the data of [53], although (again) not as closely matching the data of Zhang et al. [53].

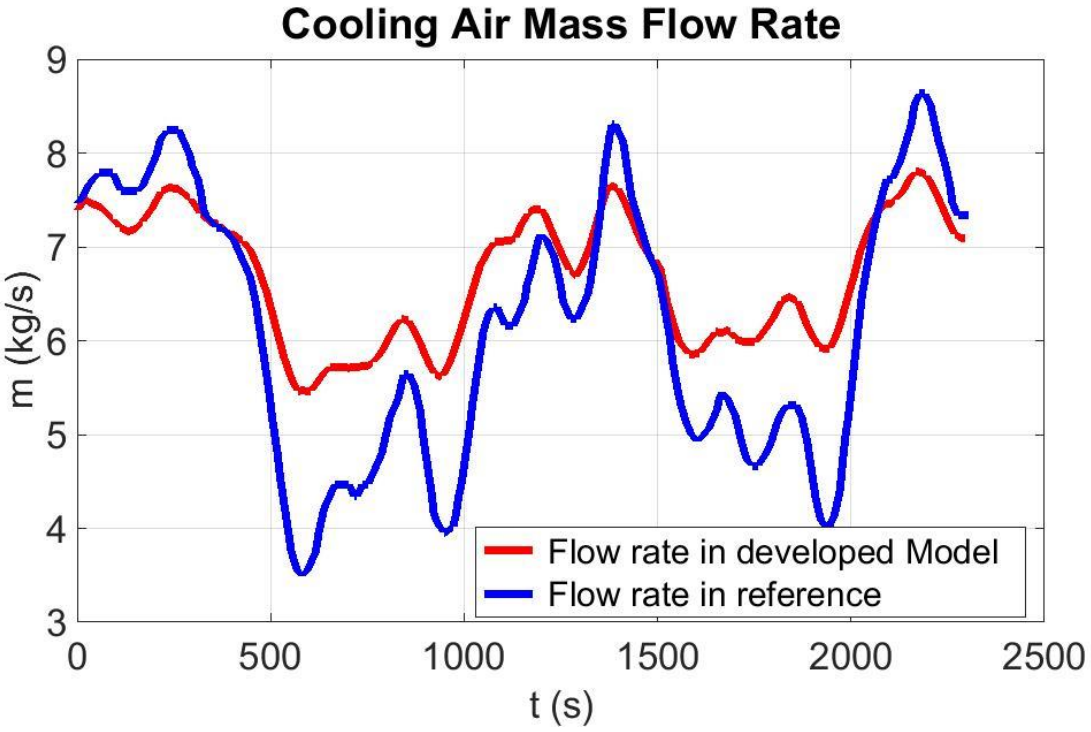

Figure 5-30: Compatibility of Mass Flow Rate of Cooling Air Variation in This Study and [53] in the Second Scenario

5.5. Case Study

In this study, measured dynamic power demand data from a residential complex (Verano Place, VP) located in Irvine California are used as an input to evaluate the dynamic operation of the integrated SOFC-ORC model. Figure 5-31 shows the actual total power demand of the VP residential complex for a week from Monday July 25th to Sunday July 31 with 1 hour resolution, respectively. Data are used from EnergiStream Live Demand Dashboard. As it is clear from the plot the trend of demand is similar for each day. The demand is higher on week days and lower demand is observed on weekend days. The demand profiles of Monday July 25th and Sunday July 30th, with the highest and lowest demand in the week, are used for the current simulations. Figure 5-32 and Figure 5-33 show the actual total power demand of the VP residential complex from July 25th to July 30th for 24 hours with 15-minute resolution, respectively.

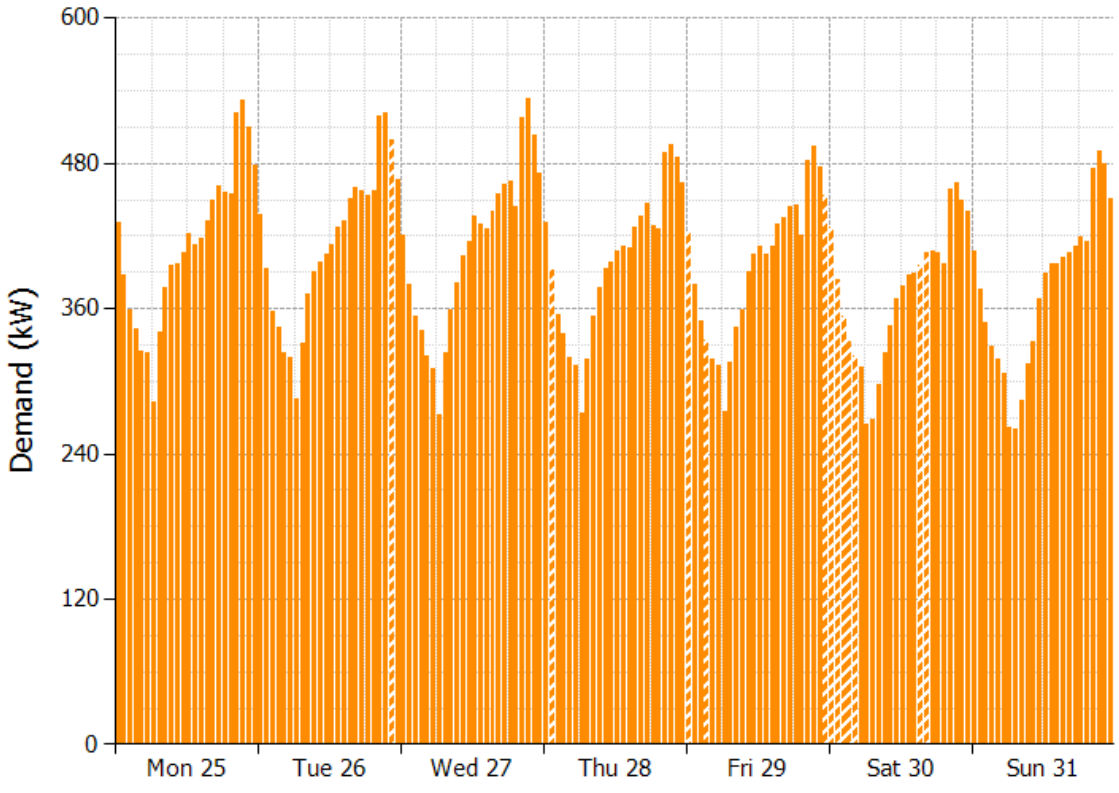

Figure 5-31: Actual Total Power Demand of the VP Residential Complex for a week from Monday to Sunday

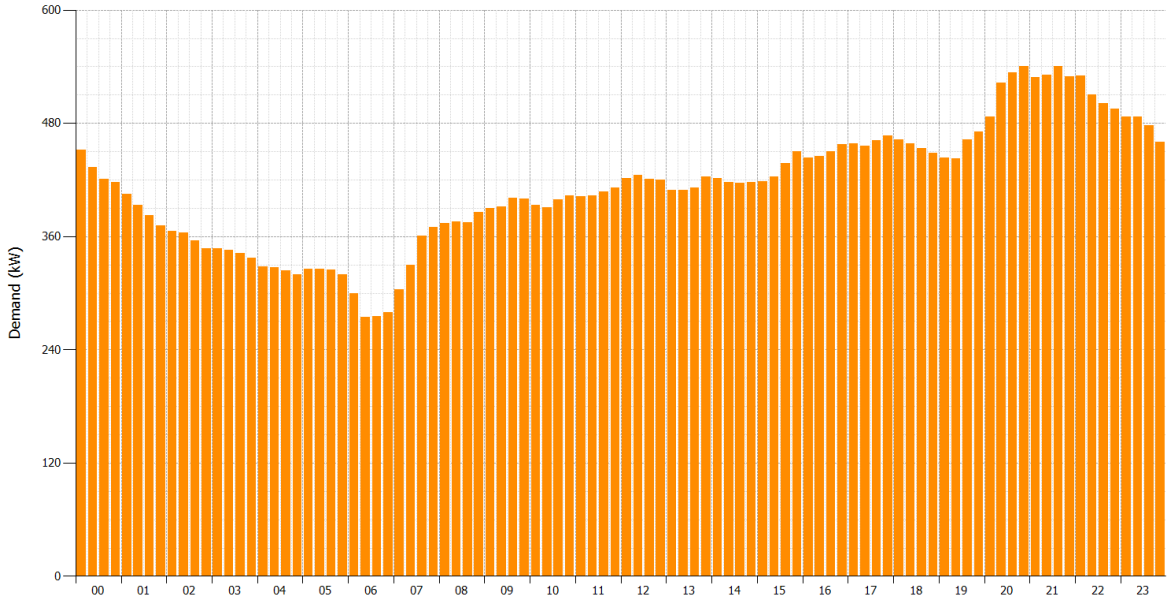

Figure 5-32: Actual Total Power Demand of the VP Residential Complex on July 25th for 24 hours

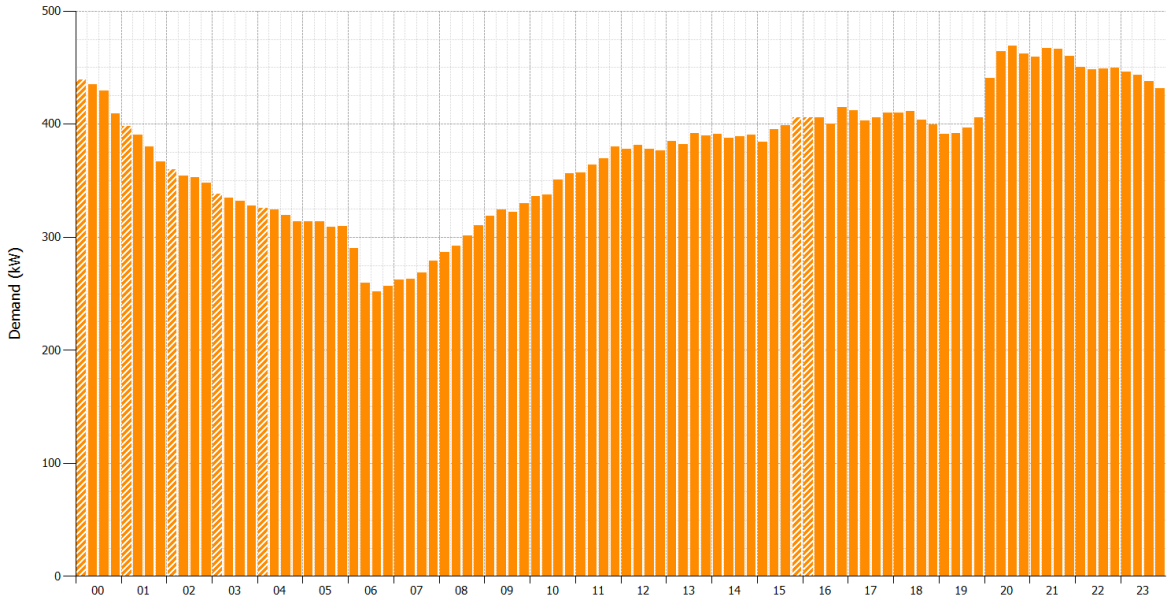

Figure 5-33: Actual Total Power Demand of the VP Residential Complex on July 30th for 24 hours

Electricity demand varies between 274.5kW and 540.3kW on July 25 and between 252kW and 470kW on July 31. The demand is higher in the evening when all the residents are home and using electric devices, as expected. During the week the demand is higher than that of the weekend. Looking at the total demands of the complex gives a less dynamic demand in comparison to single

home, which is good for achieving high capacity factor and less dynamic ramping requirements for the current power and cooling generation system.

It is assumed that a 400kW SOFC is used to meet most of the Verano Place community demand. A portion of the remaining demand will be provided by the ORC system and the rest will be met by the grid. As a result, different scenarios are considered for dispatching the integrated SOFC-ORC model including actual and bounded VP power demand as shown in Figure 5-34 and Figure 5-35 for a week day and weekend day, respectively.

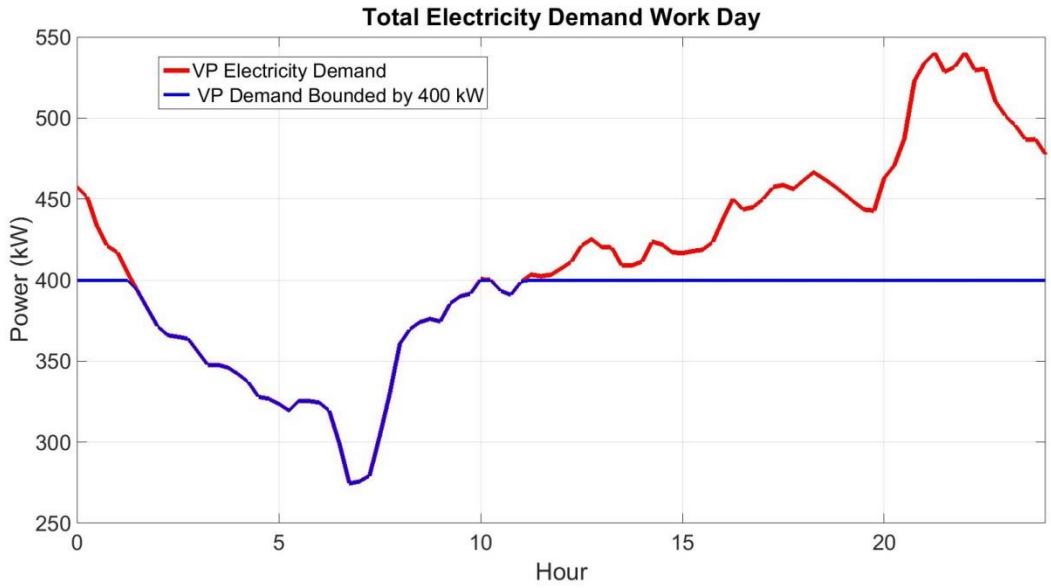

Figure 5-34: Total Electricity Demand and Bounded Electricity Demand by 400 kW for weekday

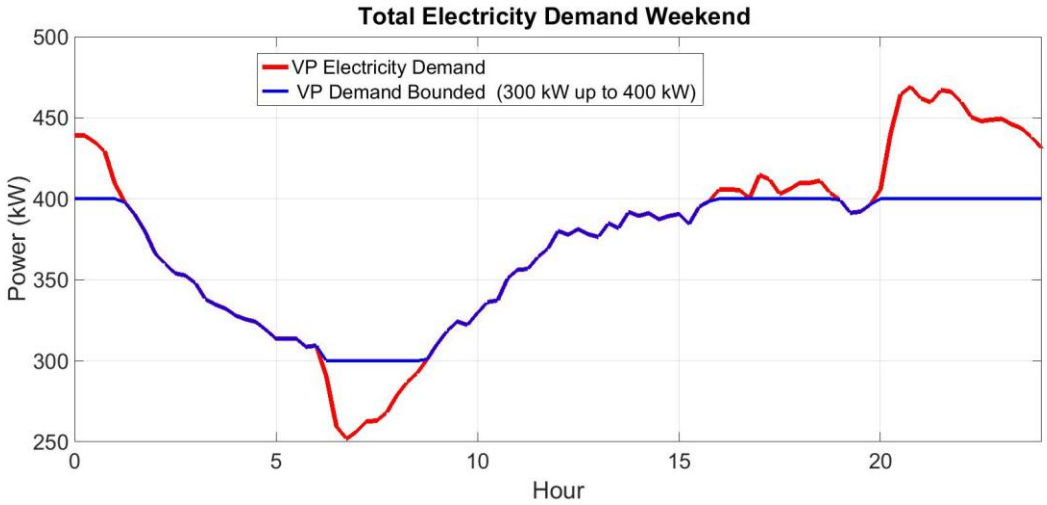

Figure 5-35: Total Electricity Demand and Bounded Electricity Demand by 400 kW for weekend

5.6. Integrated System Steady State Operation

The integrated system has been designed for a 400kW SOFC and a 25kW ORC system. Table 5-17 and Table 5-18 show the steady state operation condition of the SOFC system and ORC system.

Table 5-17: Steady State Operation Condition of the SOFC

Parameter	**Value**
Fuel Utilization	75[%]
Air Utilization	15[%]
Operating Voltage	0.79[V]
Current Density	0.34A/cm^2
Stack Efficiency	50[%]
Power Output	364[kW]
Exhaust Gas Temperature	592.2[K]
Exhaust Gas Mas Flow Rate	1.269[kg/s]

Table 5-18: Steady State Operation Condition of the SOFC

Parameter	Value
Evaporator Pressure	2212[kPa]
Evaporator Temp	400[K]
Superheat	22.7[K]
Condenser Pressure	264[kPa]
Condenser Temp	314[K]
ORC Flow Rate	1[kg/s]
Power Output	26.5[kW]
Efficiency	10[%]
Exhaust Gas Outlet Temperature	344[K]

5.6.1. Effect of Fuel Utilization on Steady State Operation

Figure 5-36 to Figure 5-42 show the effects of fuel utilization (FU) on steady state operation parameters. Figure 5-36 presents the effect of FU on total power output of the SOFC. Electrical power generated from the SOFC system reduces less significantly with the increase in fuel utilization factor at low FU values, whereas the generated electrical power decreases more rapidly at higher FU values due to a decrease in air utilization that is forced by higher operating temperatures due to increased heat production (electrochemical losses increase) at higher FU, which causes more blower work.

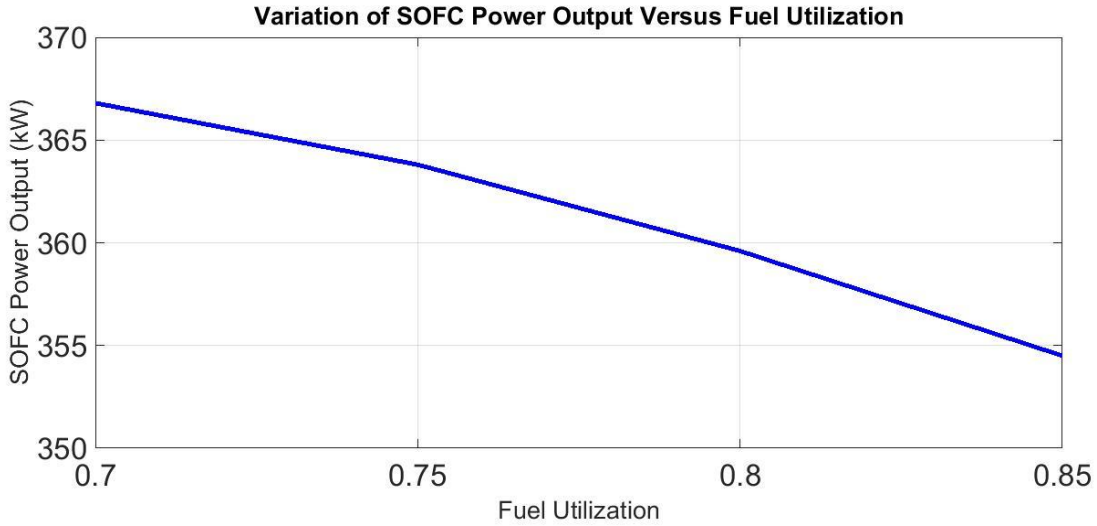

Figure 5-36: Effects of Fuel Utilization on SOFC Power Output

Figure 5-37 shows that increasing fuel utilization increases the efficiency of SOFC system due to decreasing the amount of fuel mass flow that is electrochemically oxidized versus combustion conversion in the anode tail-gas oxidizer (ATO) for use in the balance of plant. Efficiency increases from 43% to 49% by increasing FU from 0.7 to 0.85.

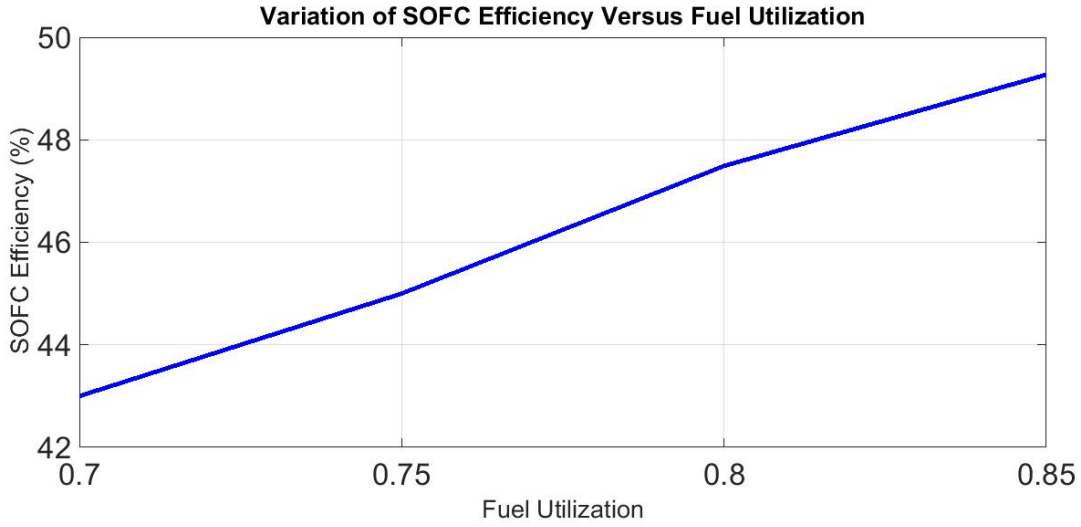

Figure 5-37: Effects of Fuel Utilization on SOFC Efficiency

Figure 5-38 and Figure 5-39 show the effects of FU on SOFC exhaust gas temperature and mass flow rate. Increasing FU causes a decrease in the amount of fuel leaving the anode compartments of the fuel cell stack. Because of this, less fuel is available in in the oxidizer to burn,

so that the exhaust gas temperature decreases. On the other hand, air utilization is decreased by increasing fuel utilization, and as a result more air leaves the cathode outlet and enters the oxidizer. This causes an increase in exhaust mass flow rate with increasing FU, as shown in Figure 5-39.

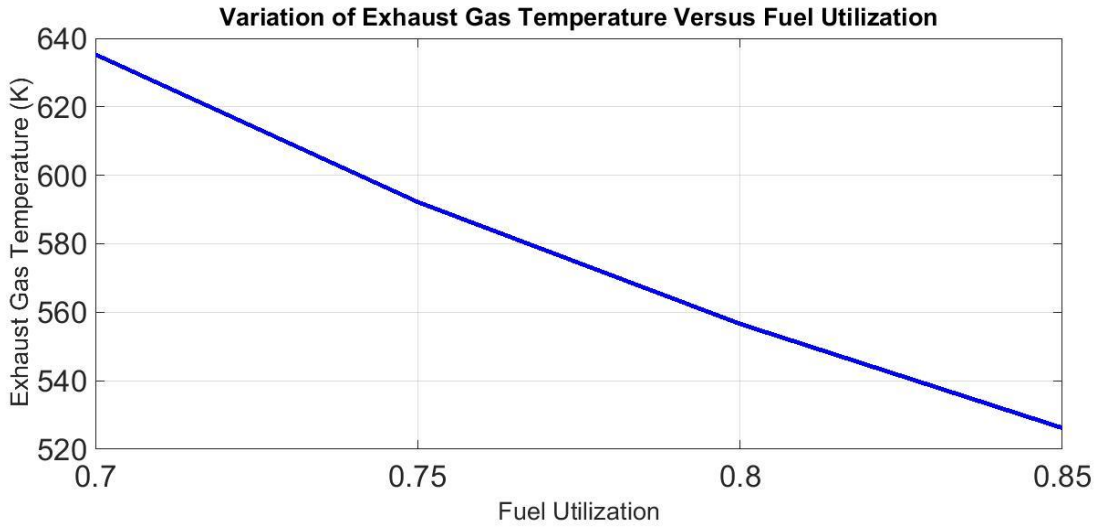

Figure 5-38: Effects of Fuel Utilization on SOFC Exhaust Gas Temperature

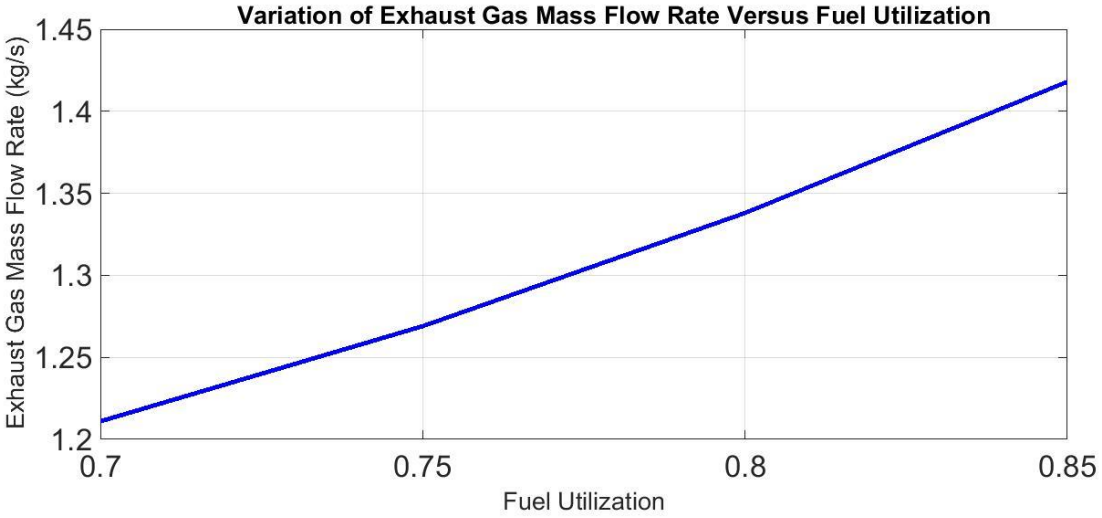

Figure 5-39: Effects of Fuel Utilization on SOFC Exhaust Gas Mass Flow Rate

By increasing the FU the potential for transferring heat to the ORC working fluid decreases, which causes less power to be produced in the ORC (see Figure 5-40). Figure 5-41 shows that the total power output decreases by increasing the FU of the SOFC. Total efficiency increases by increasing FU due to increased electrochemical production of power in the SOFC, which is more efficient than the heat-engine production of power in the ORC.

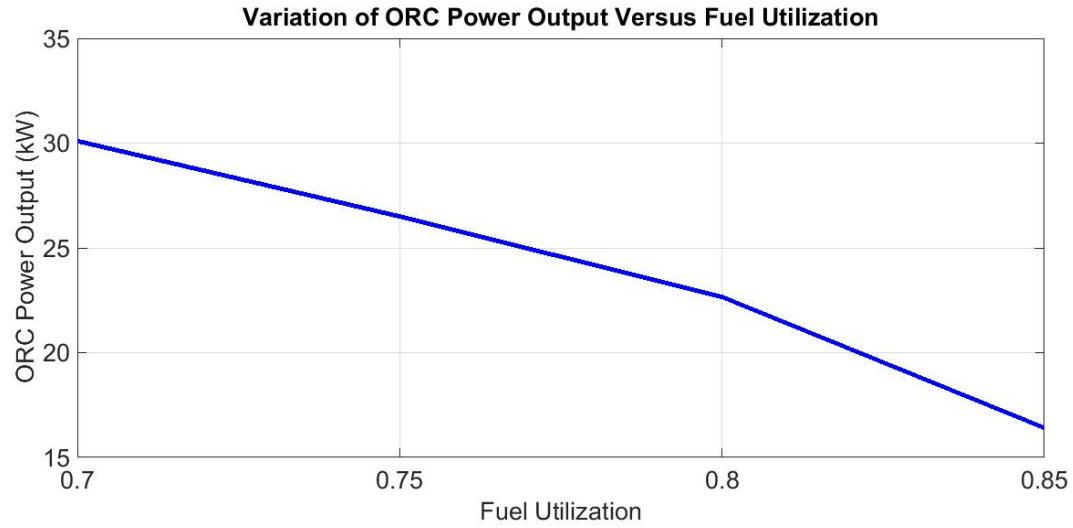

Figure 5-40: Effects of Fuel Utilization on ORC Power Output

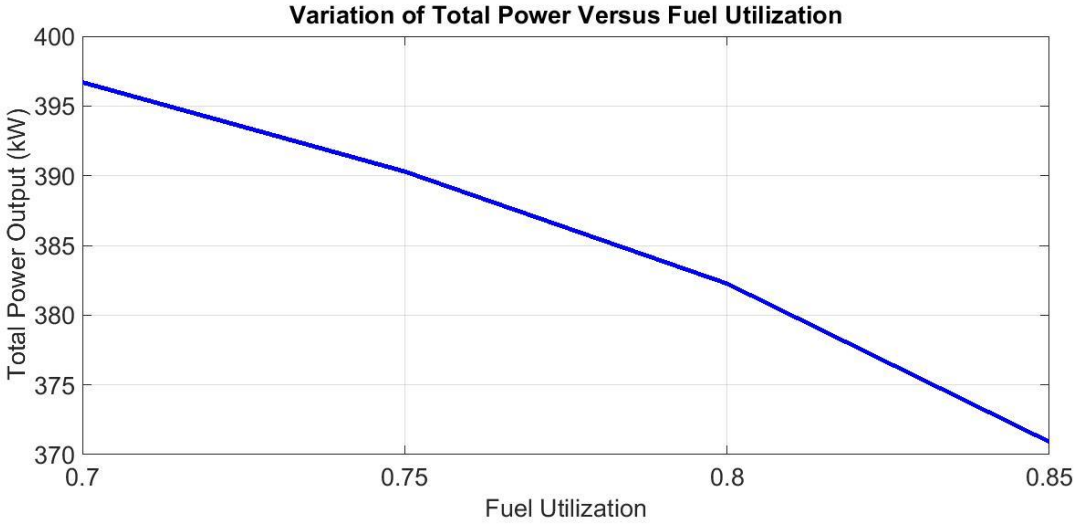

Figure 5-41: Effects of Fuel Utilization on Total Power Output

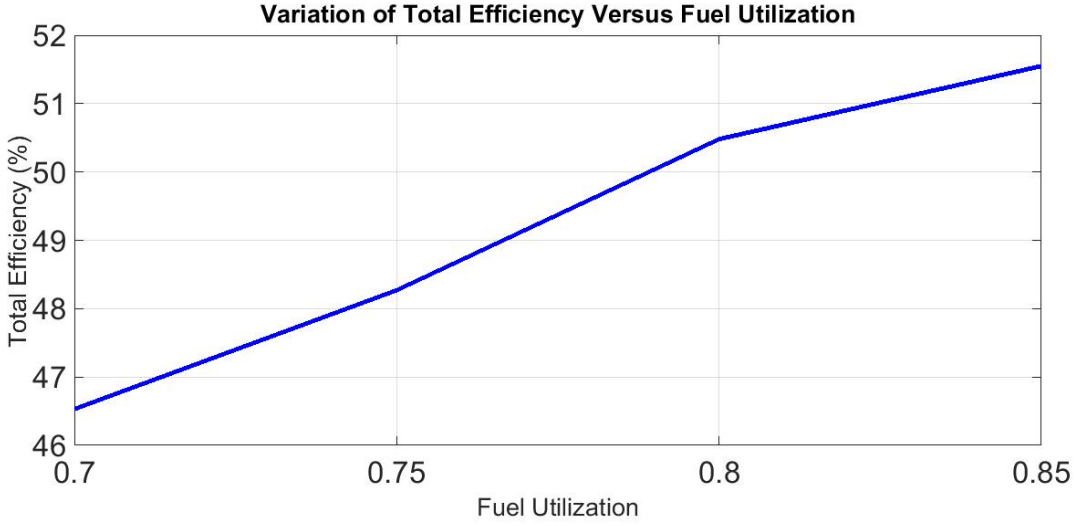

Figure 5-42: Effects of Fuel Utilization on Total Efficiency

5.7. Dynamic Operation

The results of dynamic operation for two different days of the week with highest demand (workday) and lowest demand (weekend) are presented in this section.

5.7.1. Workday Load Dynamic Operation

The electricity demand shown in Figure 5-32 is used as a desired demand applied to the spatially resolved dynamic SOFC model. Demand has been applied to the model in two scenarios: full load (Figure 5-43), and as a load bounded by 400kW (Figure 5-44). SOFC model results (Figure 5-43 and Figure 5-44) show that the SOFC stack generated output power follows the desired demand quite closely. The difference between the total output and desired demand is due to the dynamic blower electricity use.

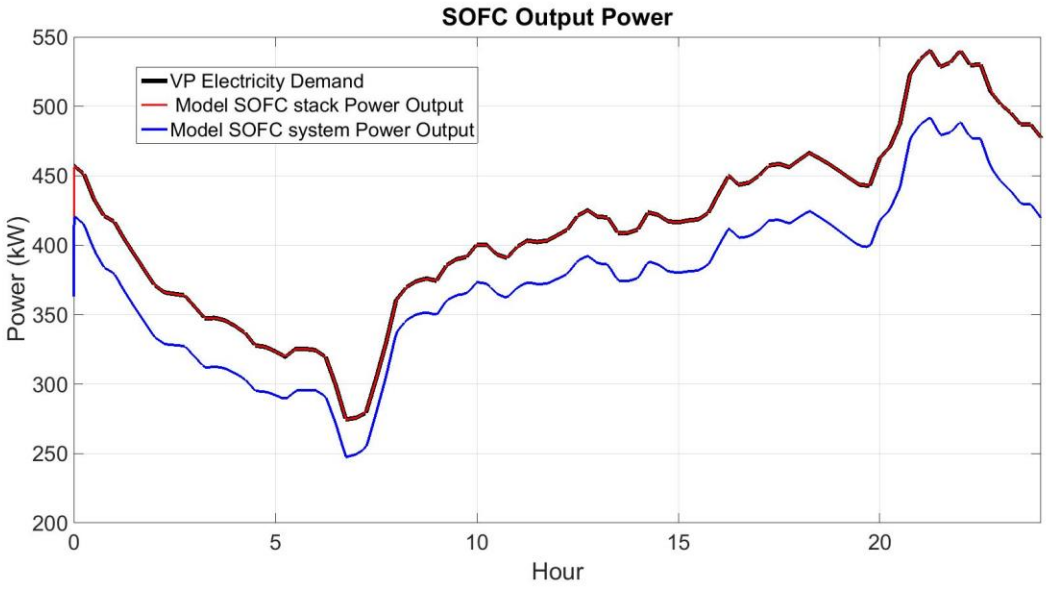

Figure 5-43: SOFC model stack and total power output following the residential electricity demand

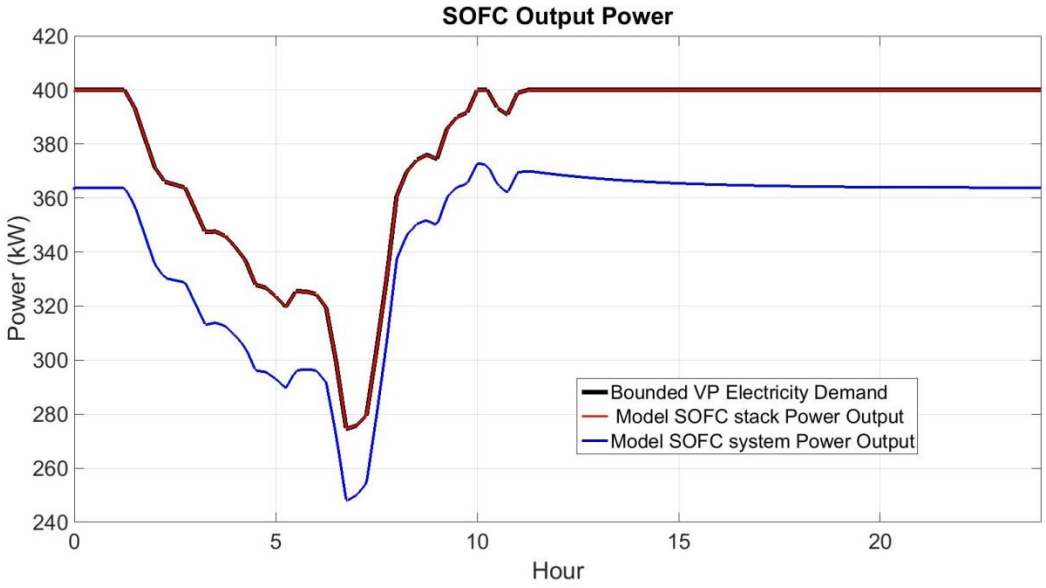

Figure 5-44: SOFC model stack and total power output following the bounded residential electricity

Figure 5-45 depicts the variation of electrical efficiency versus time. Electrical efficiency varies between 47% and 43% for the full load scenario and between 47% and 45% for the bounded load scenario. The average efficiency during dynamic operation is 45% and 46% for full load and bounded load scenarios, respectively. As expected, the highest efficiency occurs at the time of significant decrease in the power demand. There is a sharp decrease in the efficiency at full load during the time of running system at higher power than the design point.

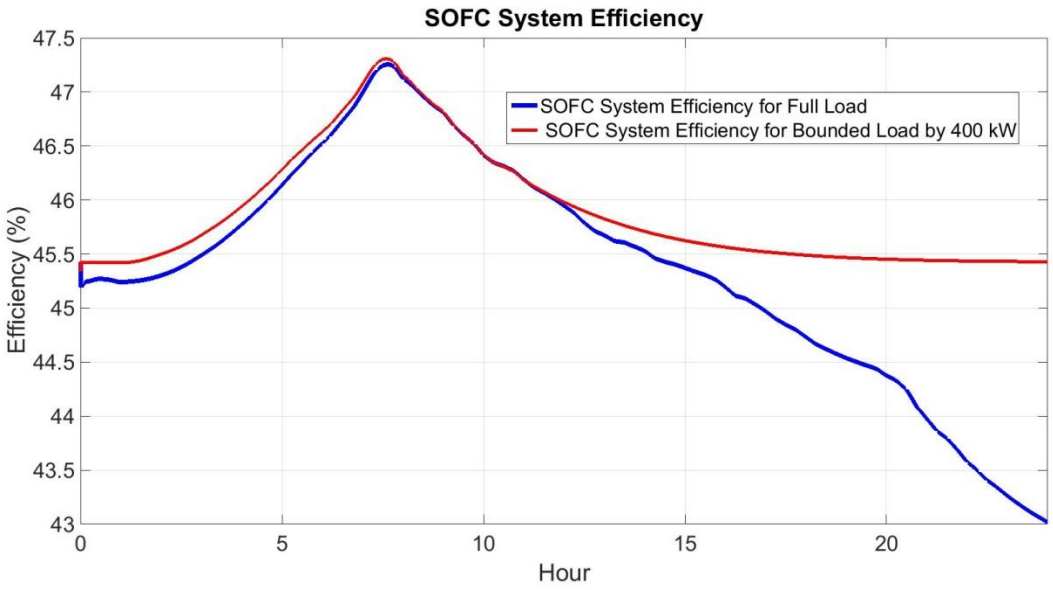

Figure 5-45: Variation of SOFC electrical efficiency versus time

Temperature and mass flow rate of the SOFC exhaust gas versus time are presented in Figure 5-46 and Figure 5-47, respectively. In the SOFC system, the oxidizer output is used for preheating fuel and air and then leaves the system as exhaust. This SOFC system exhaust has sufficient quality to be used in an ORC system. The exhaust mas flow rate changes between 1.51kg/s and 0.94kg/s for the full load scenario and between 1.26kg/s and 0.94kg/s for the bounded load scenario. The average rate is 1.26 and 1.2 for full and bounded load scenarios, respectively. At the point that the demand decreases, the mass flow rate decreases to provide less power. Exhaust gas temperature follows the same trend as the mass flow rate. The exhaust gas temperature changes between 651K and 551K for full load and between 619K and 555K for bounded load. The average temperature is 600K and 589K for full and bounded load, respectively

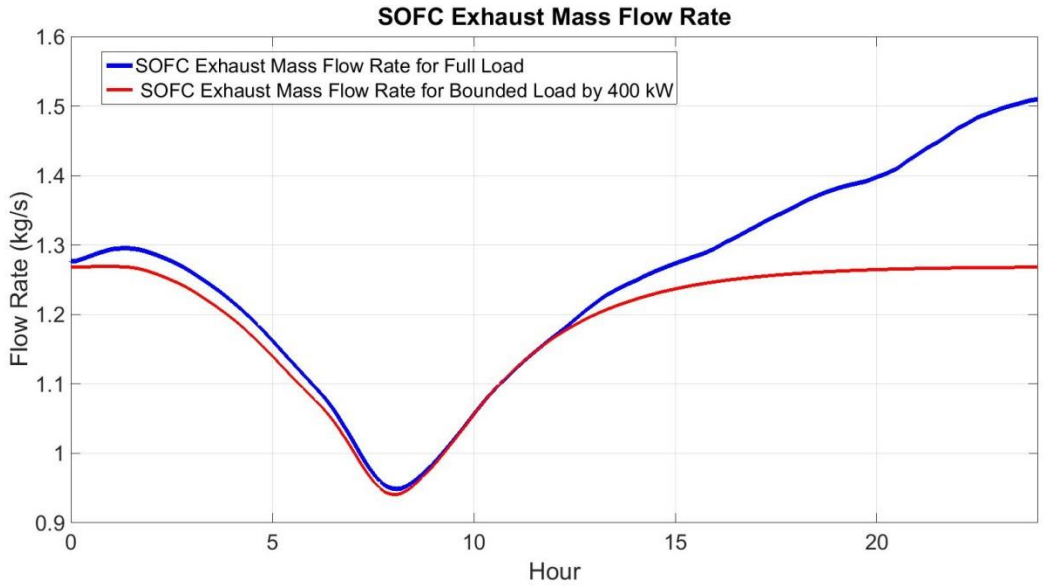

Figure 5-46: Exhaust gas mass flow rate of the SOFC system

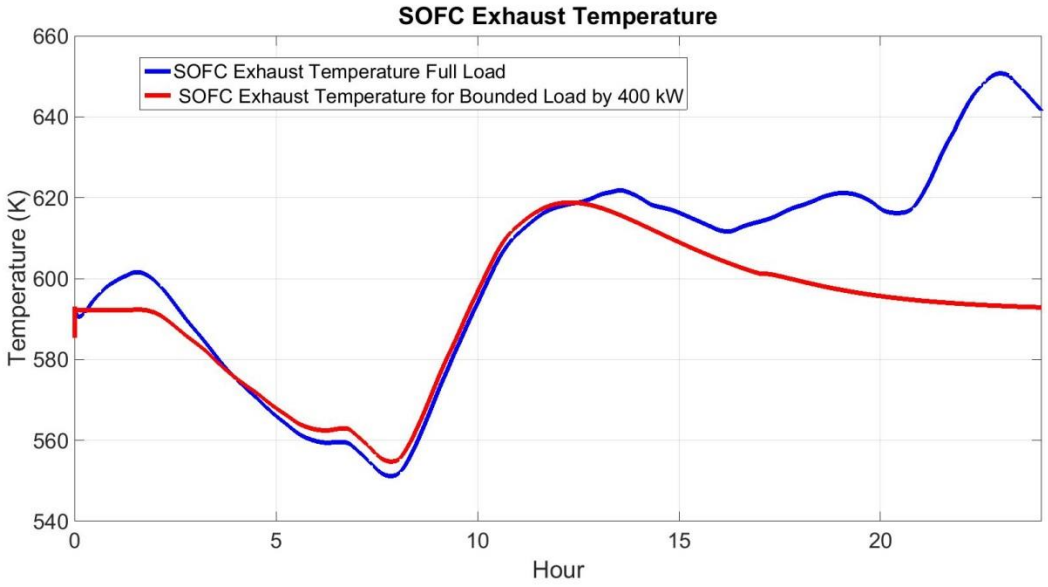

Figure 5-47: Exhaust gas temperature of the SOFC system

The captured SOFC exhaust gas (Figure 5-46 and Figure 5-47) is considered as the dynamic input of the ORC model. The obtained ORC output power based upon the dynamic exhaust gas flow and temperature input conditions is presented in Figure 5-48. When lower heat energy is available from the SOFC exhaust the ORC produces less power. The ORC power changes between 39kW and 16kW for the full load scenario and between 28kW and 17kW for bounded load scenario. The average power output is 26kW and 25kW for full and bounded load scenarios,

respectively. The ORC system can generate power which is around 7 percent of SOFC generated power.

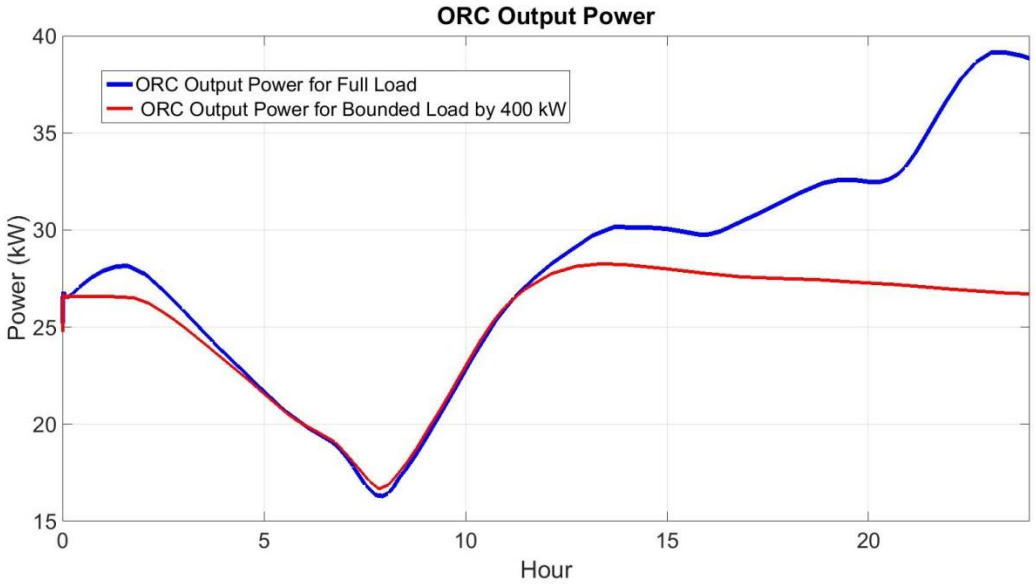

Figure 5-48: ORC Output power versus time

ORC mass flow rate is controlled by exhaust mass flow rate and exhaust temperature of the SOFC system, so that it follows quite the same trend as exhaust heat available for the ORC. Note that the ORC mass flow rate goes higher than the design point for steady state during the period when the VP apartment complex power demand is higher than the design steady state power demand (Figure 5-49). The ORC working fluid mass flow rate changes between 1.31kg/s and 0.68kg/s for full load scenario and between 1kg/s and 0.67kg/s for bounded load scenario. The average flow rate is 0.98kg/s and 0.94kg/s for full and bounded load, respectively. Superheat temperature at evaporator outlet was designed to be around 20K in steady state. In dynamic operation superheat temperature varies from 42K to 10K for full load scenario and from 34K and 12K for bounded load scenario with an average of 22K and 21K, respectively. During the time that higher heat energy is available system superheats the working fluid at evaporator outlet more than steady state design.

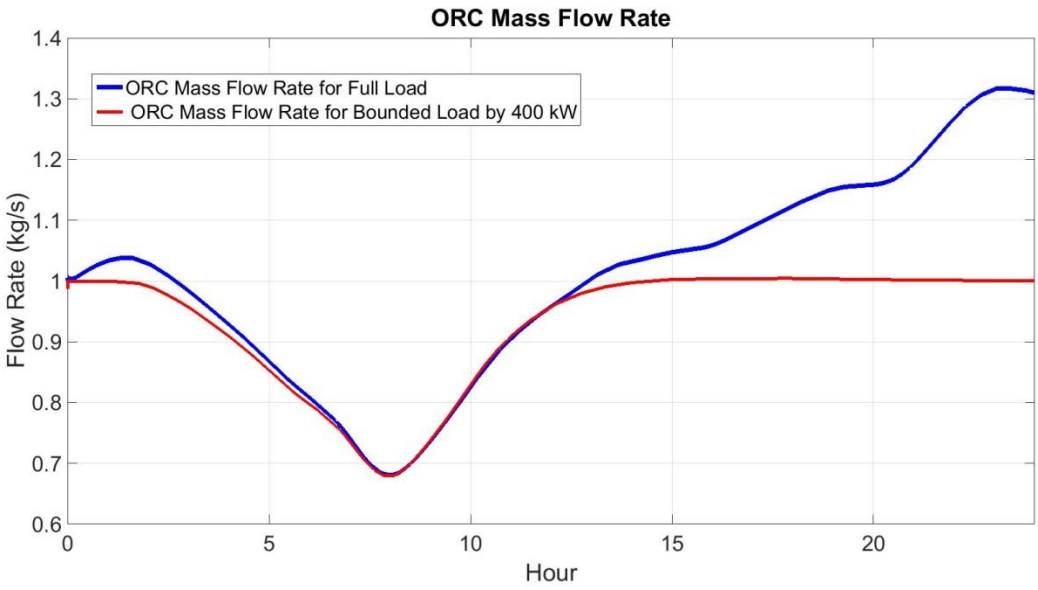

Figure 5-49: ORC Working Fluid Flow during the Dynamic Operation

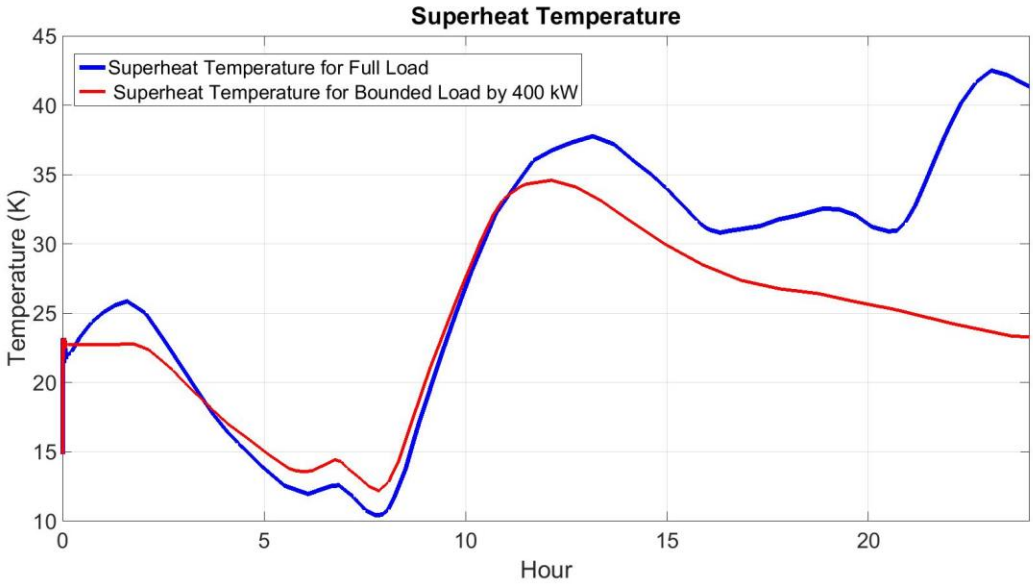

Figure 5-50: Superheat Temperature at Evaporator Outlet

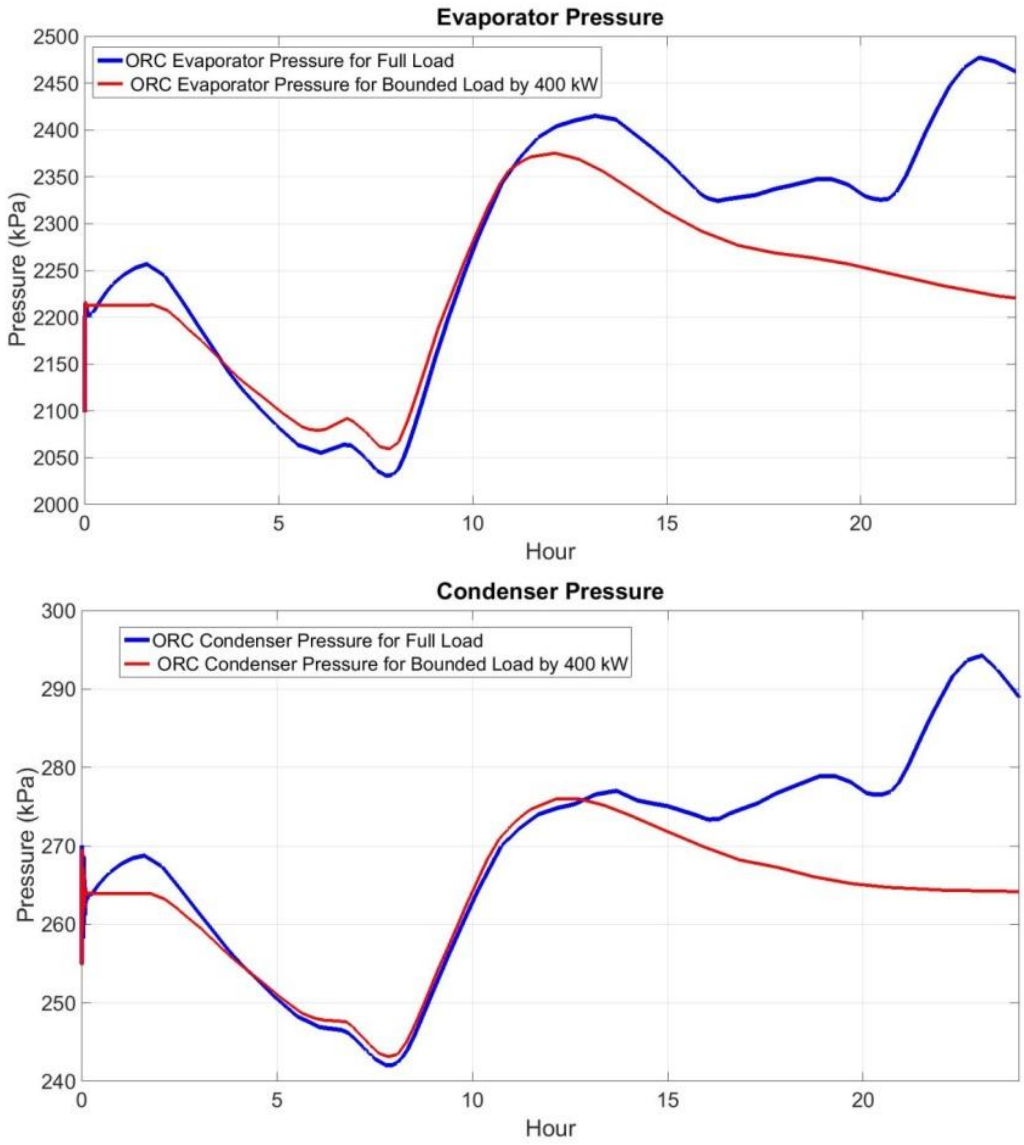

Figure 5-51: ORC Evaporator and Condenser Pressure versus Time

Figure 5-51 shows the pressure of evaporator and condenser during the dynamic operation. Pressures vary with the same sort of trends as those shown for the exhaust coming into the evaporator. Also, the pressure ratio stays the same during the operation.

The ORC efficiency during the dynamic operation stays the same as under steady state operation at around 10%. Due to the control approach used in ORC system, the manipulated parameters such as expander rotational speed and pump rotational speed are changed based upon SOFC exhaust gas temperature and mass flow rate (heat potential of SOFC exhaust gas). So, for

example in a case that SOFC exhaust gas mass flow rate and temperature are lower than steady state design point, the mass flow rate of ORC working fluid decreases and net generated power of ORC decreases as a result. In the other words, this relatively constant efficiency is due to the same dynamic behavior of heat energy available (SOFC exhaust gas) and net work produced in ORC. Figure 5-52 presents the evaporator and condenser wall temperature versus time.

Figure 5-53 shows the exhaust gas outlet temperature of ORC. Exhaust gas does not vary much during the entire dynamic operation time, remaining around 340 K.

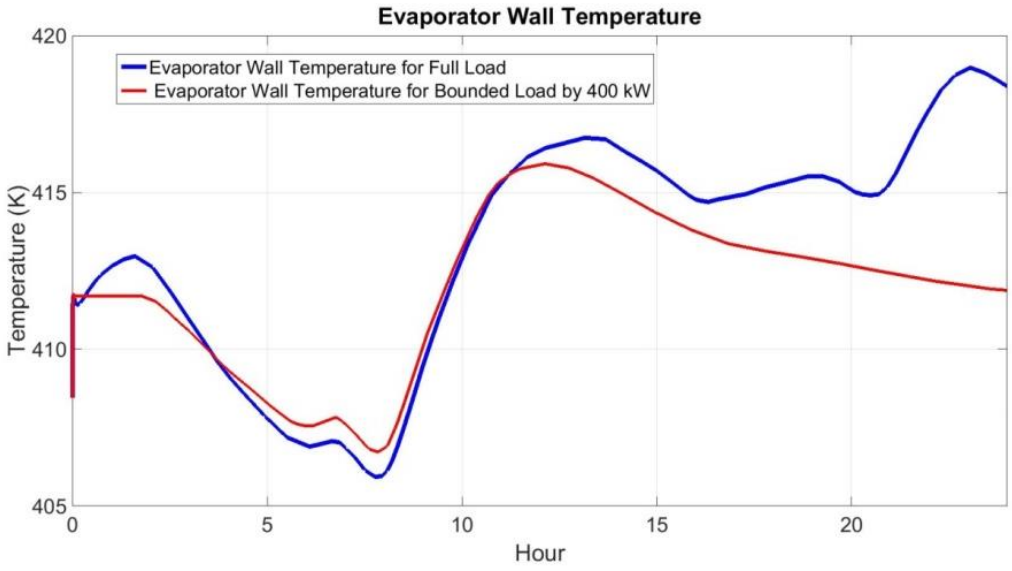

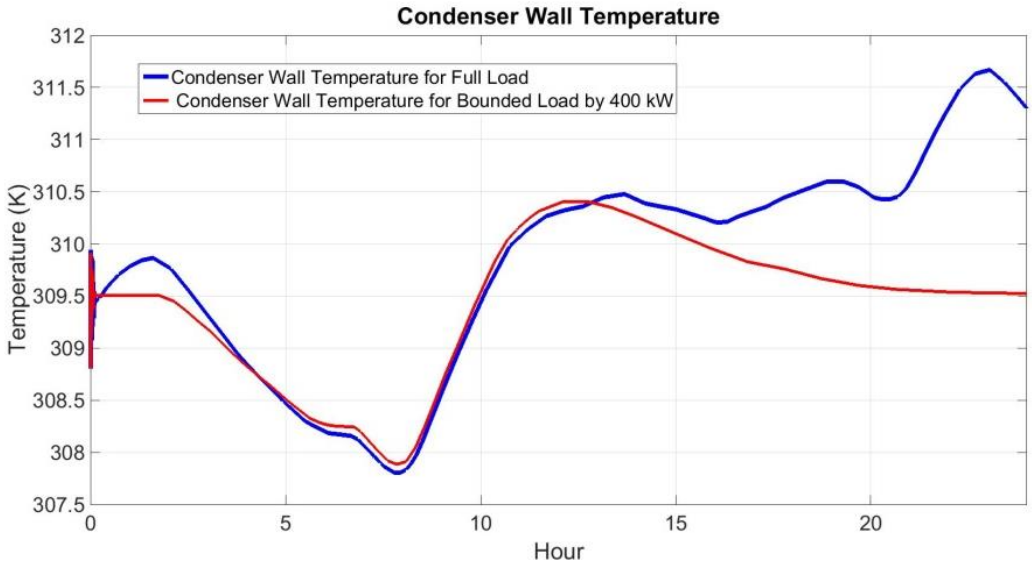

Figure 5-52: Evaporator and Condenser Wall Temperature versus Time

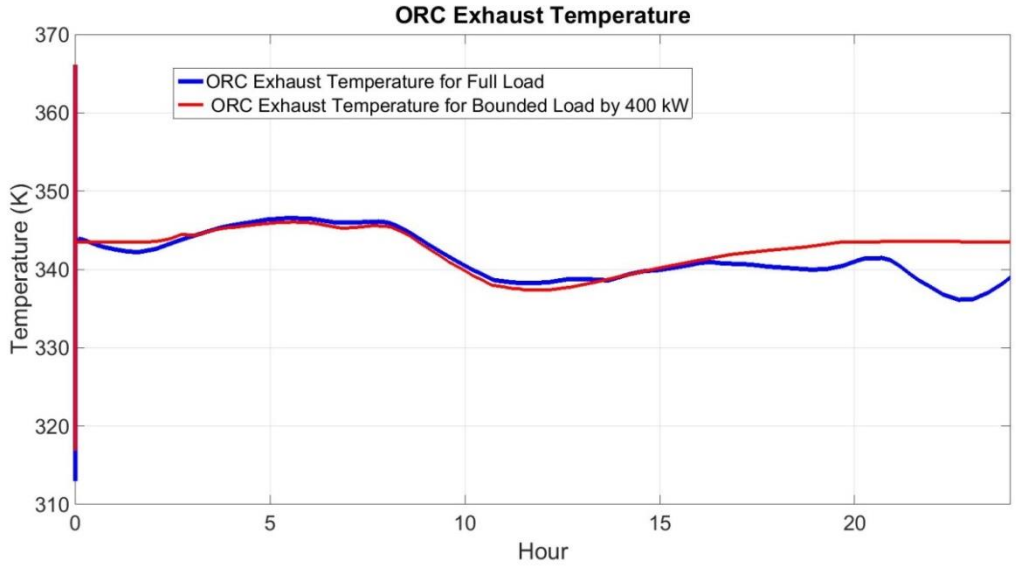

Figure 5-53: ORC Exhaust Gas Outlet Temperature

It had been found that the exhaust gas leaving the ORC evaporator was of insufficient quality to run the absorption chiller system to have combined generation of excess power in ORC and cooling in absorption chiller, so, another integrated system scenario could be pursued. This concept would meet dynamic cooling demands by sending the exhaust gas of SOFC goes through an absorption chiller to meet the cooling demand if there is any cooling demand. In both scenarios

(SOFC-ORC and SOFC-AC) the exhaust after ORC or absorption chiller is high enough to produce hot water.

The exhaust temperature of the SOFC generally goes higher than the design point of the absorption chiller of 280°C, and was able to boil enough water in both generators to provide cooling. The chiller was simulated based upon the lowest available temperature of one day; that temperature was held constant throughout the day giving a conservative estimate of the amount of cooling possible from the absorption chiller. Figure 5-54 presents the cooling output of the absorption chiller using the variable mass flow of the SOFC system from the working day (Figure 5-46) at a fixed temperature of 278°C. The very sharp increase in the first few seconds is due to the initialization and heating-up of the system. Cooling varies between 200kW to 242kW for the bounded scenario and between 200kW and 270kW for full load scenario (excluding the heating-up periods). During the times when higher amounts of hear are available the absorption chiller provides more cooling, as expected.

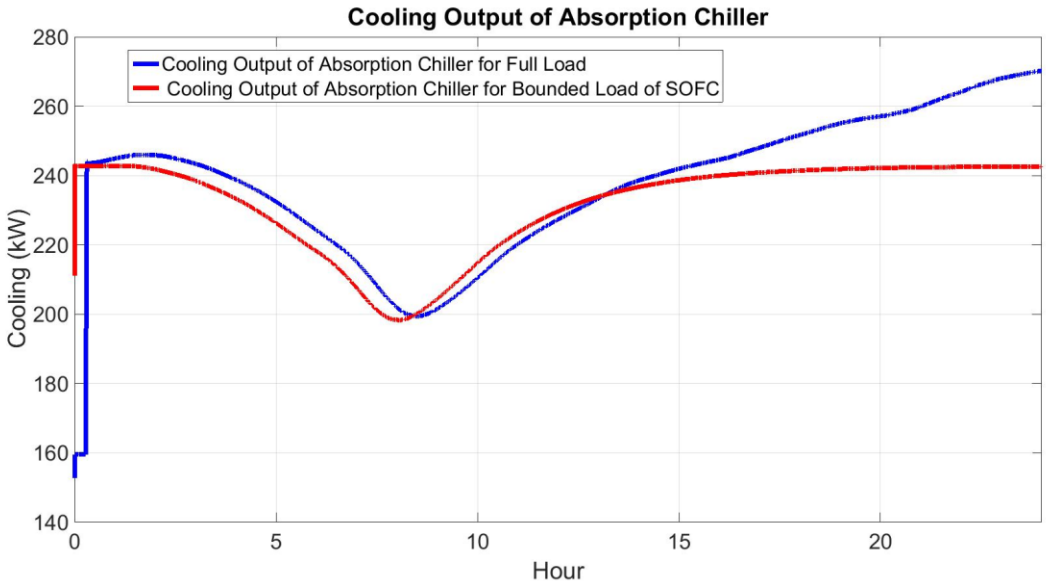

Figure 5-54: Absorption Chiller Cooling Output from SOFC Exhaust for Work Day

The COP calculated using Eq. (5-1) for the absorption chiller model is a function of the cooling generated and the heat recovered from the fuel cell exhaust within the chiller's generator and heat exchangers which recover heat for use in the second generator (a double-effect absorption chiller).

$$COP = \frac{\dot{Q}_{cooling}}{\dot{Q}_{gen1} + \dot{Q}_{HX}} \tag{5-1}$$

The cooling calculated is a function of the change in mass flow of the chilled water loop. Water enters the evaporator at 12.5°C and exits at 7°C.

$$\dot{Q}_{cooling} = \dot{m}_{chill} c_p \Delta T \tag{5-2}$$

Eq. 5-2 describes how the cooling is calculated where $\dot{M}_{chill}$ is the chilled water flow rate through the evaporator and c_p is the specific heat of water.

The COP does not vary as dramatically as the other parameters. This is due to the fact that the cooling potential decreases with decreasing in available heat in generator. At lower flow rates, the heat exchange is less effective, so less heat is being added to the cycle which affects the cooling output. Therefore, the COP, although dynamic, stays within a range of about 1.07 and 1.1, as shown in Figure 5-55.

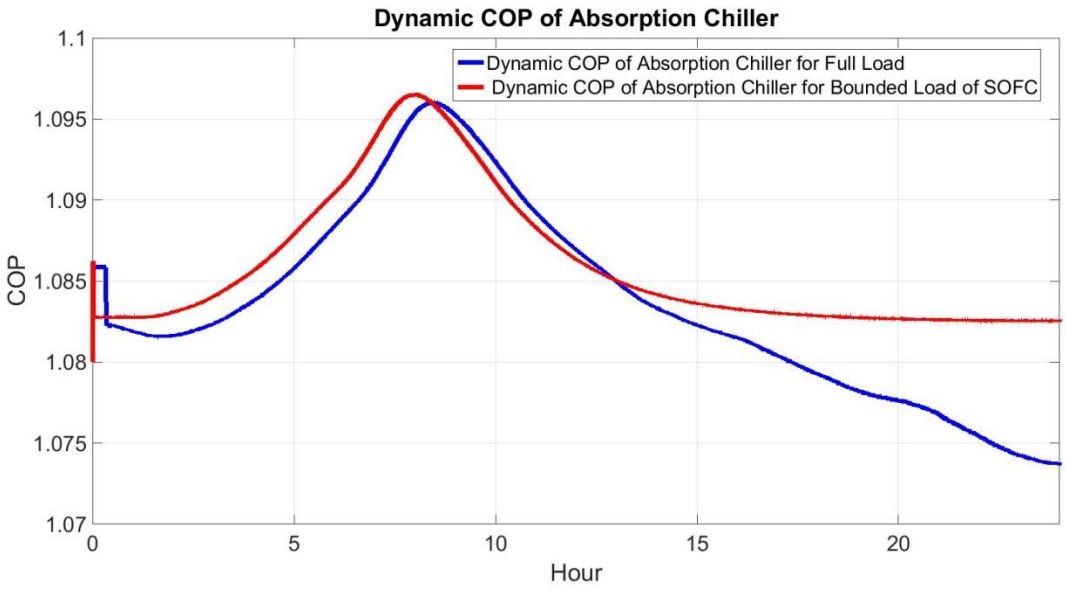

Figure 5-55: COP of AC as a Function of Time for SOFC Operation of a Work Day

The average COP for the day was 1.08 for full load scenario and 1.09 for bounded scenario, and the average cooling provided was 131kW for the full load scenario and 128kW for the bounded scenario.

Figure 5-56 shows the exhaust gas from the absorption chiller. Exhaust gas temperature follows the same trend as the SOFC exhaust coming in. The exhaust gas temperature changes between 123^{o}C and 143^{o}C for the full load scenario and between 122^{o}C and 135^{o}C for the bounded load scenario. The average temperature is 134^{o}C and 132^{o}C for the full and bounded load scenarios, respectively. The exhaust gas from the absorption chiller in these simulations has sufficient quality to be used to heat up water for community use.

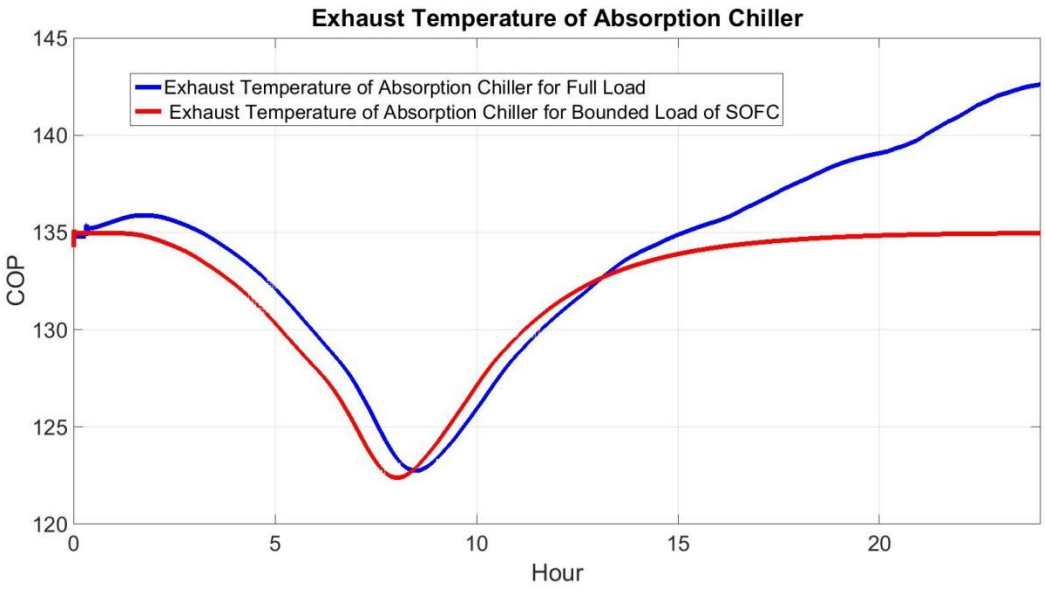

Figure 5-56: Exhaust Gas Temperature of Absorption Chiller for Working Day

5.7.2. Weekend Day Load Dynamic Operation

The Electricity demand shown in Figure 4.35 is used as a desired demand applied to the spatially resolved dynamic SOFC model. As was the case for the workday scenario, demand of weekend has been applied to the model in two scenarios: full load (Figure 5-57), and as a load bounded by 400 kW (Figure 5-58). SOFC model results (Figure 5-57 and Figure 5-58) show that the SOFC stack generated output power follows the desired demand quite closely.

Generally, all of the SOFC parameters for the weekend day scenarios follow the same logical trend as the weekday scenarios. The results for weekend day generally appear as scaled weekday results due to the similar, but scaled, demand dynamics.

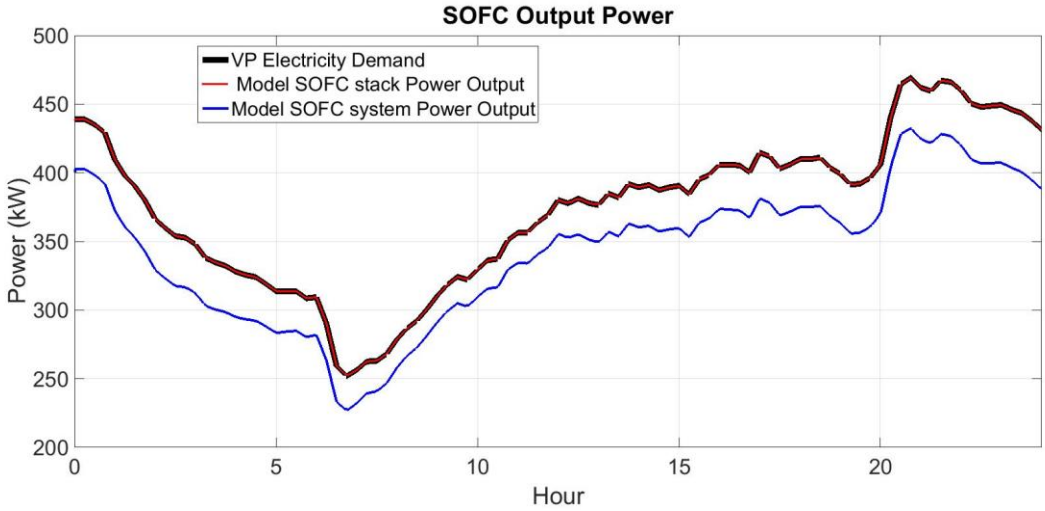

Figure 5-57: SOFC model stack and total power output following the residential electricity demand

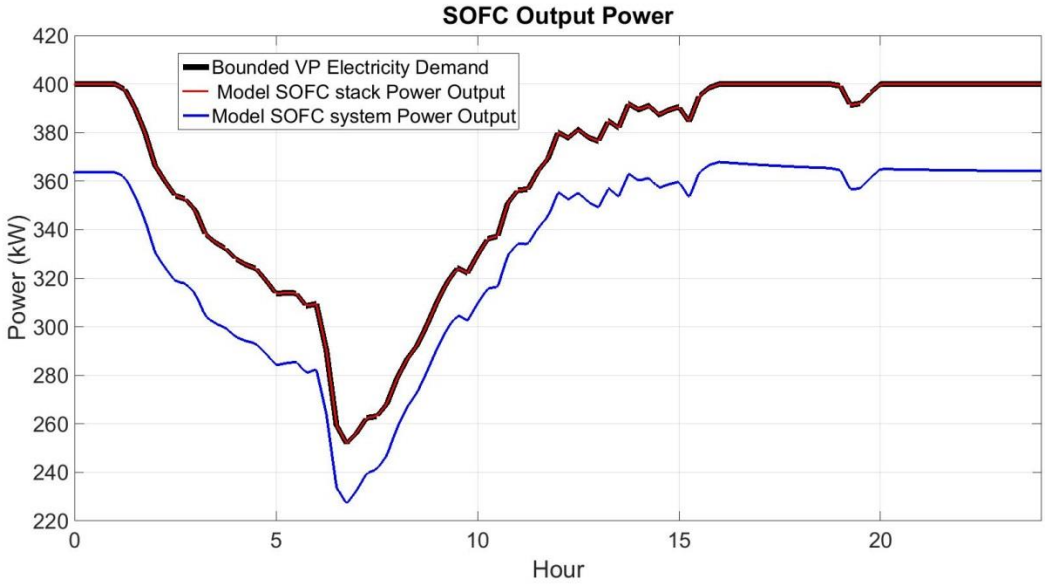

Figure 5-58: SOFC model stack and total power output following the bounded residential electricity

Electrical efficiency varies between 48% and 44% for the full load scenario and between 48% and 45% for the bounded load scenario. The average efficiency during dynamic operation is 46% and 49% for full load and bounded load scenarios, respectively. As expected, the highest efficiency occurs at the time of significant decrease in the power demand.

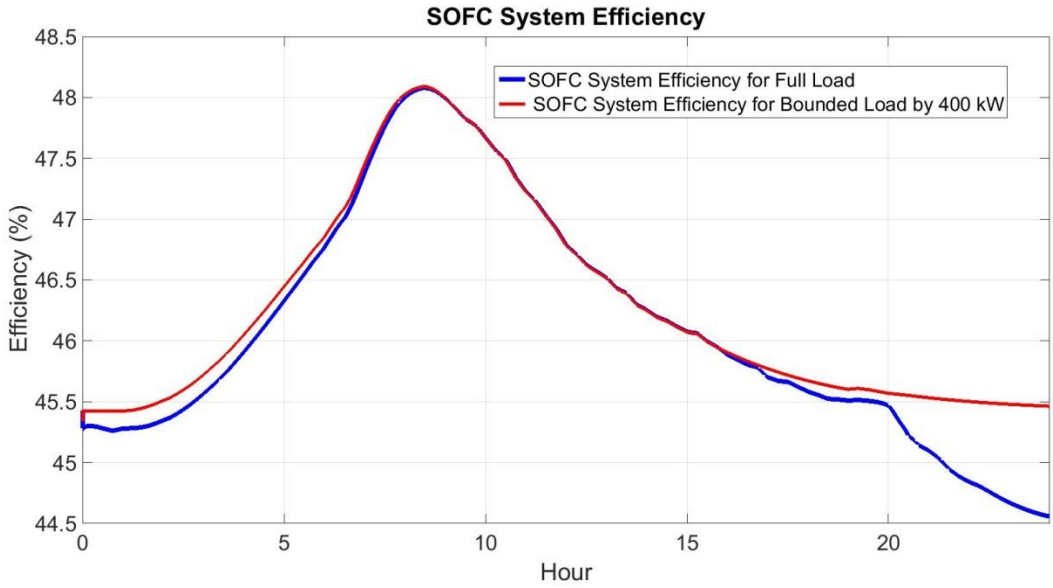

Figure 5-59: Variation of SOFC electrical efficiency versus time

Temperature and mass flow rate of the SOFC exhaust gas versus time are presented in Figure 5-60 and Figure 5-61, respectively. The exhaust mas flow rate changes between 1.4kg/s and 0.8kg/s for full load scenario and between 1.26kg/s and 0.8kg/s for the bounded load scenario. The average rate is 1.17 and 1.15 for the full and bounded load scenarios, respectively. The exhaust gas temperature changes between 624K and 545K for full load scenario and between 624K and 549K for the bounded load scenario. The average temperature is 594K and 591K for full and bounded load scenarios, respectively

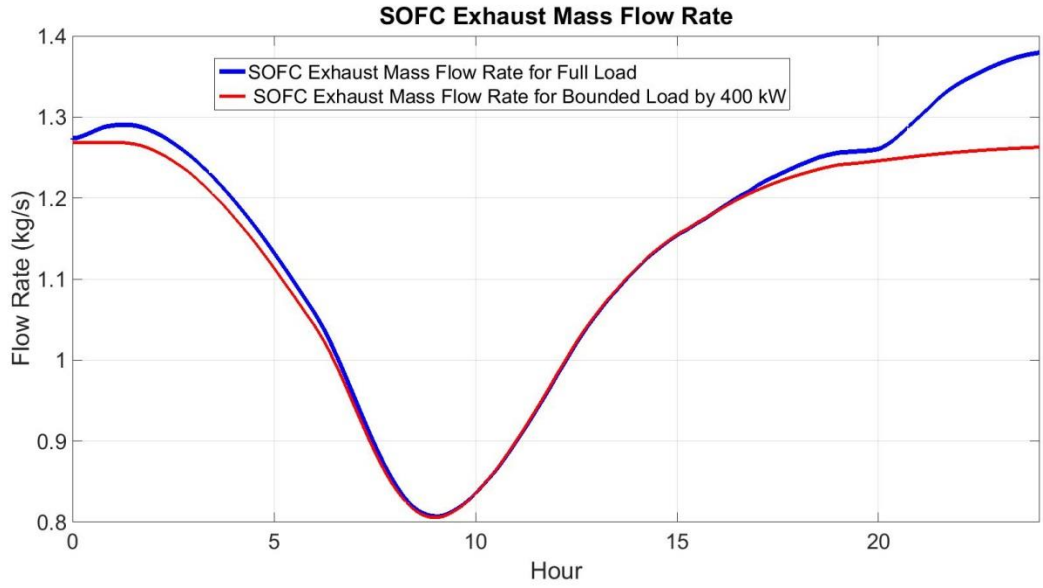

Figure 5-60: Exhaust Gas Mass Flow Rate of the SOFC System

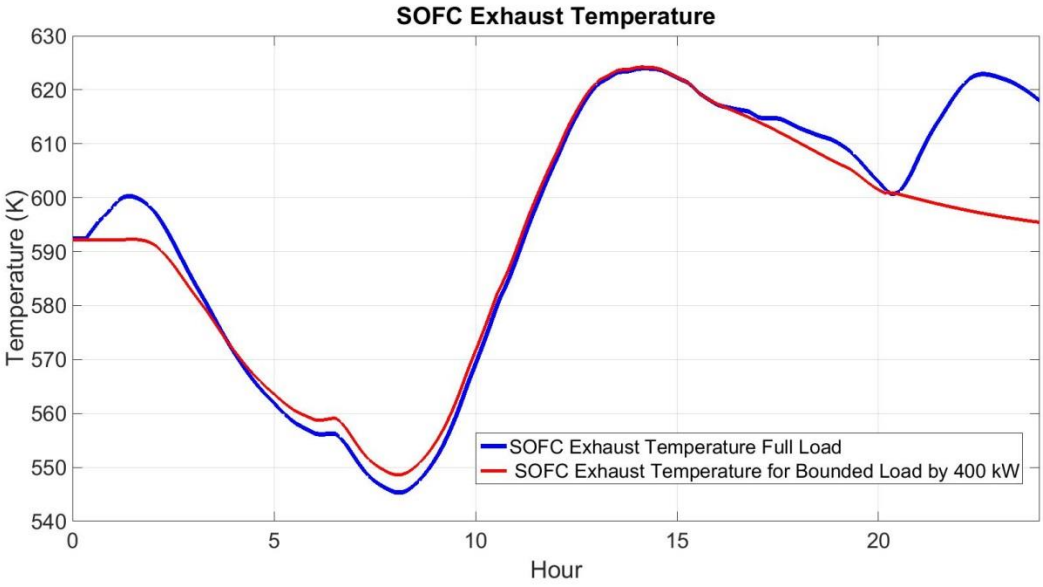

Figure 5-61: Exhaust Gas Temperature of the SOFC System

The captured SOFC exhaust gas (Figure 5-60 and Figure 5-61) is considered as the dynamic input of the ORC model. The obtained ORC output power based upon the dynamic exhaust gas flow and temperature input conditions is presented in Figure 5-62. The ORC power changes between 33kW and 12kW for the full load scenarios and between 24kW and 14kW for the bounded load scenarios. The average power output is 26kW and 23kW for full and bounded load scenarios, respectively.

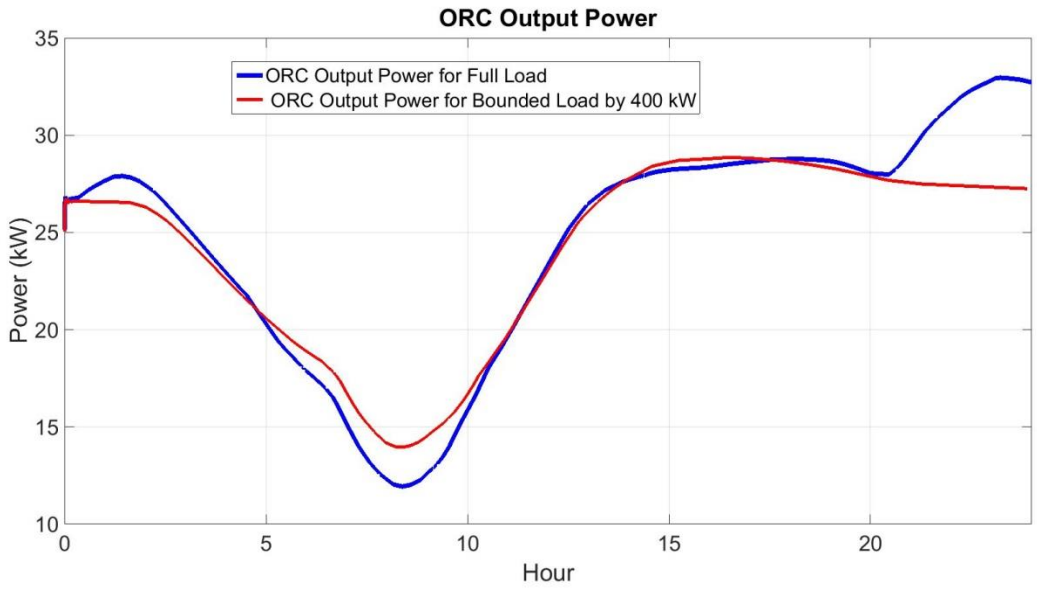

Figure 5-62: ORC Output Power versus Time

The ORC working fluid mass flow rate changes between 1.13kg/s and 0.6kg/s for the full load scenario and between 1kg/s and 0.6kg/s for the bounded load scenarios. The average flow rate is 0.95kg/s and 0.9kg/s for full and bounded load scenarios, respectively (Figure 5-63).

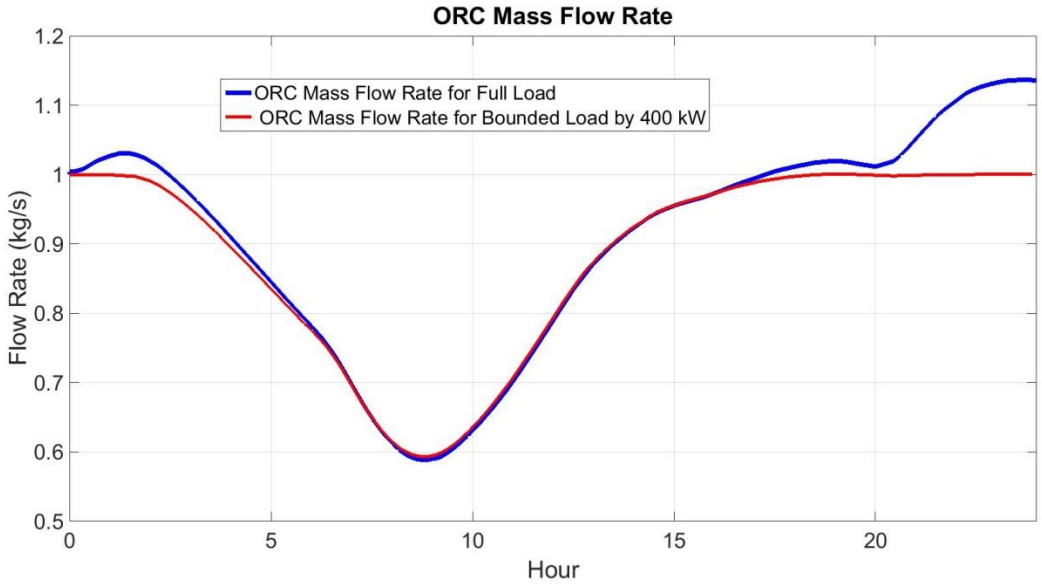

Figure 5-63: ORC Working Fluid Flow during the Dynamic Operation

In dynamic operation superheat temperature varies from 42K to 7.5K for the full load scenario and from 40K and 8K for the bounded load scenario with average of 25K and 21K, respectively.

During the time that higher heat energy is available system superheats the working fluid at evaporator outlet more than steady state design.

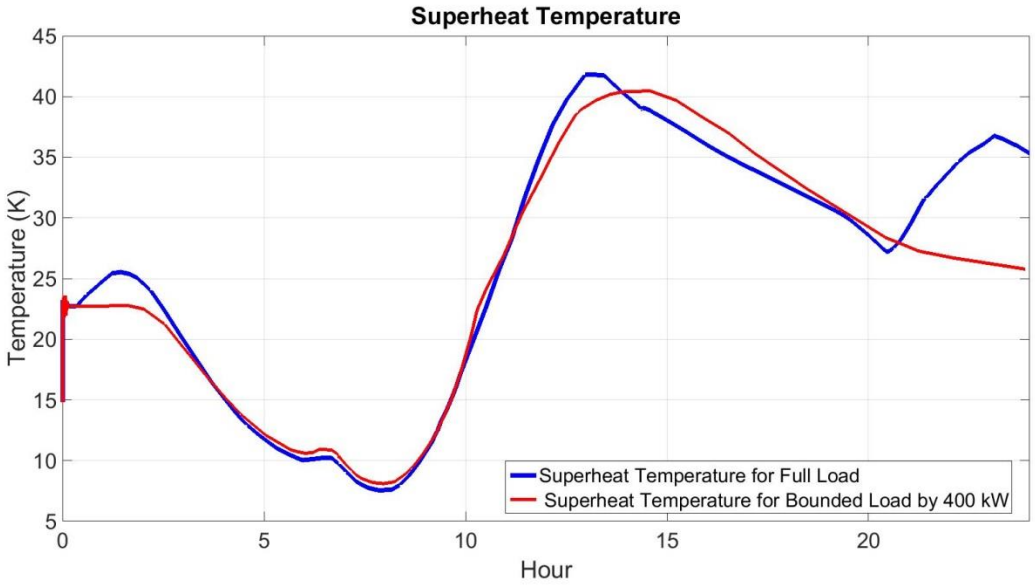

Figure 5-64: Superheat Temperature at Evaporator Outlet

Figure 5-65 shows the pressure of evaporator and condenser during the dynamic operation. The ORC efficiency during the operation stays the same as that produced under steady state operation at around 10%. Figure 5-66 presents the evaporator and condenser wall temperature versus time.

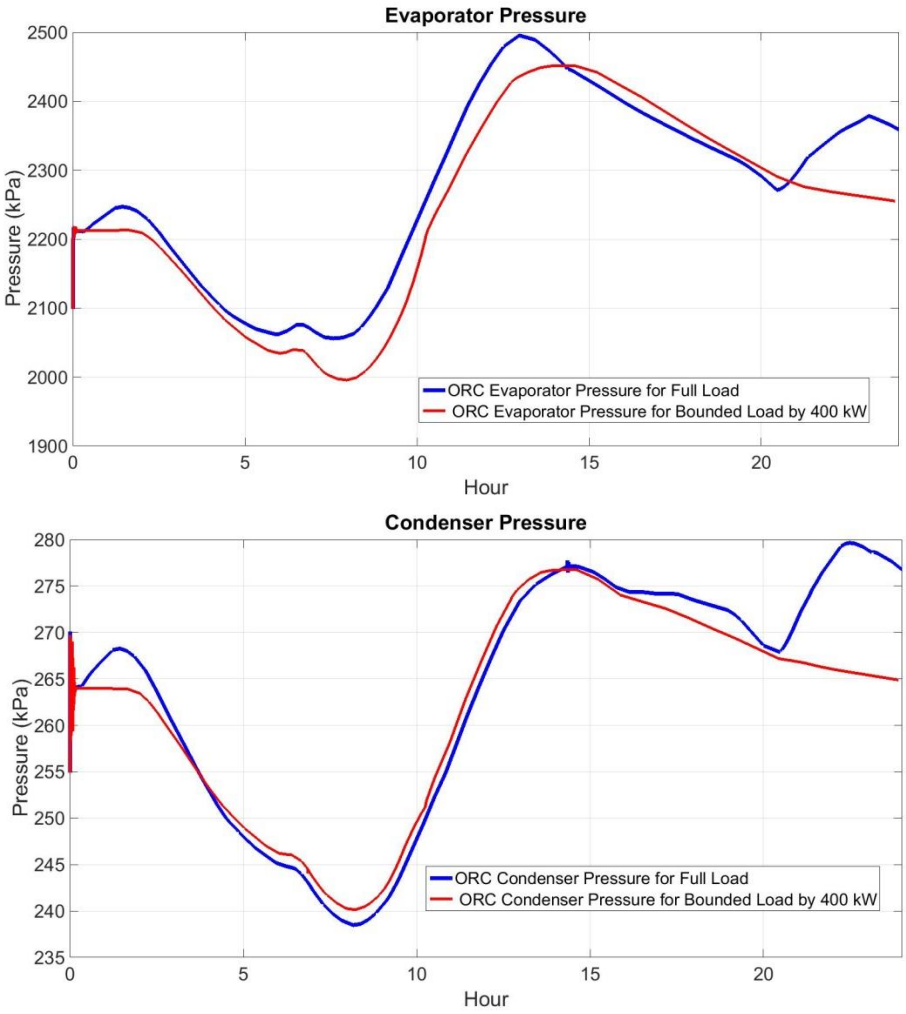

Figure 5-65: ORC Evaporator and Condenser Pressure versus Time

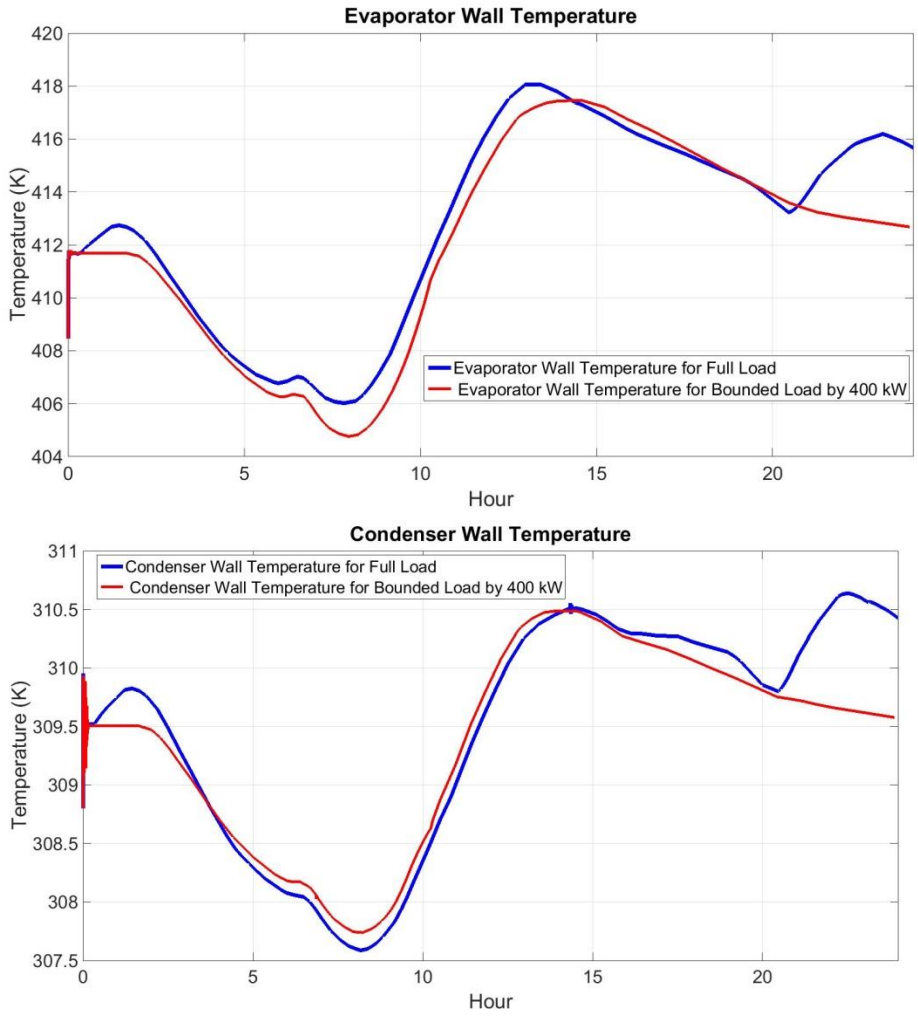

Figure 5-66: Evaporator and Condenser Wall Temperature versus Time

Figure 5-67 shows the exhaust gas outlet temperature of ORC. Exhaust gas does not vary much during the entire dynamic operation time, remaining around 340K.

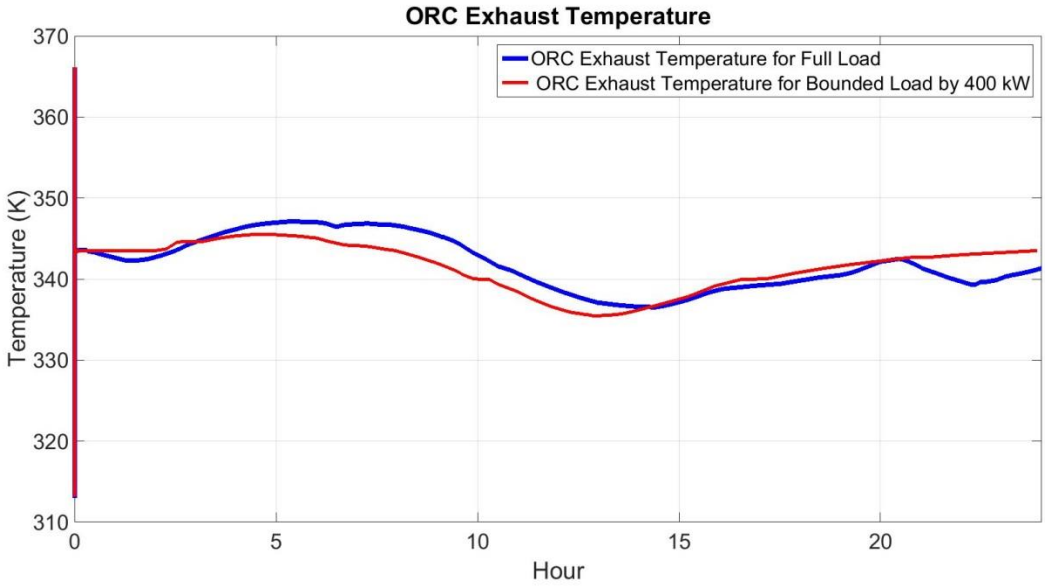

Figure 5-67: ORC Exhaust Gas Outlet Temperature

Figure 5-68 presents the cooling output of the absorption chiller using the variable mass flow of the SOFC system from the weekend day (Figure 5-60) at a fixed temperature of 272°C. The very sharp increase in the first few seconds is due to the initialization and heating up of the system. Cooling varies between 176kW to 240kW for the bounded scenario and between 175kW and 250kW for the full load scenario.

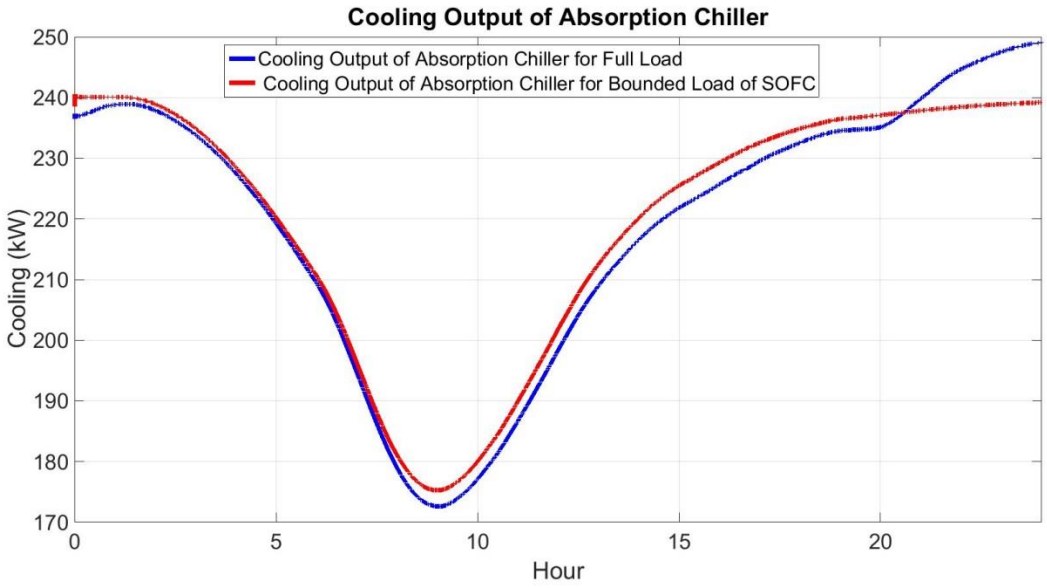

Figure 5-68: Absorption Chiller Cooling Output from SOFC Exhaust for Weekend

Figure 5-69 shows the cooling output of the absorption chiller. COP, although dynamic, stays within a range of about 1.07 and 1.1.

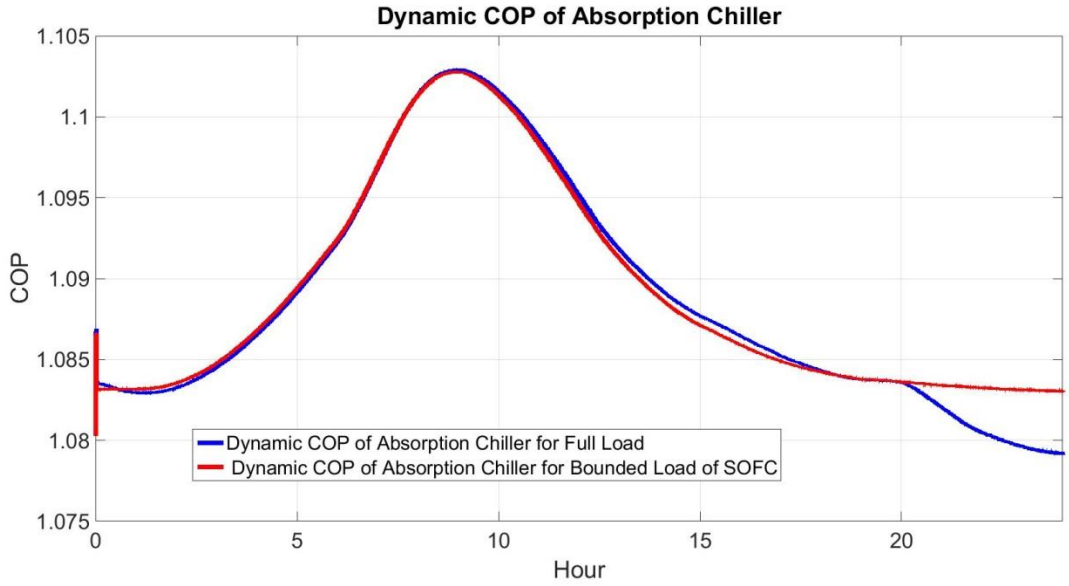

Figure 5-69: COP of AC as a Function of Time for SOFC Operation of a Work Day

The average COP for the day was 1.088 for full load scenario and 1.09 for the bounded scenario, and the average cooling provided were 121.1kW for the full load scenarios and 121.5kW for the bounded scenario.

Figure 5-70 shows the exhaust gas from the absorption chiller. Exhaust gas temperature follows the same trend as the SOFC exhaust coming in. The exhaust gas temperature changes between 115^{o}C and 136^{o}C for the full load scenarios and between 116^{o}C and 134^{o}C for the bounded load scenarios. The average temperature is 128^{o}C and 128.5^{o}C for the full and bounded load scenarios, respectively.

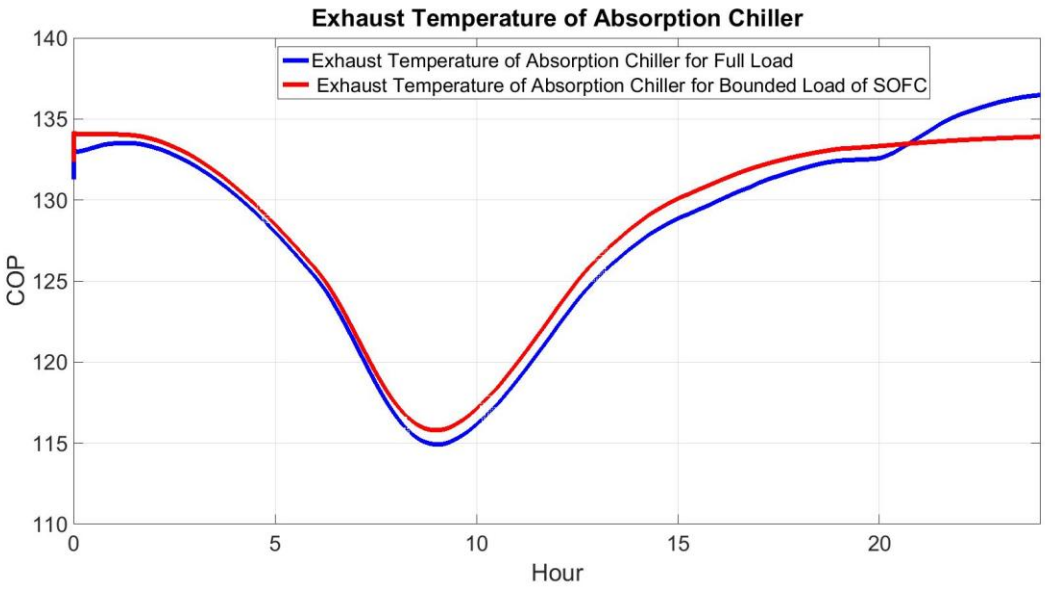

Figure 5-70: Exhaust Gas Temperature of Absorption Chiller for Working Day

6. SUMMARY, CONCLUSIONS & RECOMMENDATIONS

6.1. Summary

In this study a spatially resolved dynamic model was developed in Matlab/Simulink to study dynamic operating characteristics of an SOFC system based upon a previously developed National Fuel Cell Research Center (NFCRC) dynamic model. The modified SOFC system model was verified with data from two commercially available 2.5kW and 1.5kW SOFC systems from SOLIDpower.

A bulk dynamic model was developed for the ORC system to study the dynamic characteristics and the performance of an integrated SOFC-ORC co-generation system. The ORC dynamic model includes evaporator, condenser, expander, pump and reservoir. The ORC system model was sized and designed based upon the steady state exhaust output of a 400kW SOFC system. The ORC system model was verified with data from a literature study of dynamic operation of an ORC [53]. Two different scenarios with different distributions for exhaust gas mass flow rate and exhaust gas temperature were used to verify the developed dynamic model in this study. The percentage root mean square error (%RMSE) for power output was 1.41% and 1.49% for the two scenarios.

A previous NFCRC absorption chiller model developed in Matlab/Simulink was modified to study the dynamic characteristics and the performance of a combined SOFC-absorption chiller co-generation system.

Dynamic data from Verano Place complex located in Irvine California were used as an input to evaluate the dynamic operation of system model. Power demand had the same trend for each day. The demand was higher on week days and lower demand was observed on weekend days. Demand of Monday July 25th and Saturday July 30th, with the highest and lowest demand of the

week, were used for the simulations. Electricity demand varies between 275kW and 540kW on Monday and 252 kW and 470 kW on Saturday. The demand is higher in the evenings when all the residents are home and using electric devices, as expected. During the week the demand is higher than that of the weekend.

The integrated system was designed for a 400kW SOFC and 25kW ORC on steady state operation. Power output of the SOFC was 364kW with 50% stack efficiency. Exhaust gas temperature and mass flow rate were 592K and 1.27kg/s, respectively. ORC steady state power output was 26.5kW with 10% efficiency. By combining the SOFC with the ORC bottoming cycle 7% more power was produced.

Increasing fuel utilization from 75% to 85% decreases the fuel consumption by 15% and increases the SOFC system efficiency 8% and Total efficiency by 5%. Although higher fuel utilization decreases the amount of heat available for the bottoming cycle, the overall integrated system efficiency increases with increasing fuel utilization.

Two scenarios of workday and weekend day demand dynamics were studied for dynamic operation if the integrated SOFC-ORC system. Generally workdays had higher demand compared to weekend days. For each of the scenarios two conditions of full load and bounded load (limited to 400kW) have been evaluated. The bounded load demand scenario is less dynamic than the full load scenario. For work day SOFC average efficiency was found to be 45.3% and 45.7% for the full load and bounded load scenarios, respectively. Full load demand has higher average exhaust mass flow rate in comparison to bounded flow which is due to higher power demand. Higher power demand needs higher mass flow through the SOFC. The average exhaust temperature is 599.48K and 589.38K for the full and bounded load scenarios of the work day, respectively. The full load scenario has higher exhaust heat available, which means higher ability to produce power in the

bottoming ORC. As expected, the average ORC power output is 26kW and 25kW for the full and bounded load scenarios, respectively. In both the full and bounded load scenarios, the ORC efficiency stays the same as steady state around 10% which is due to the same dynamic behavior of heat energy available (SOFC exhaust gas) and net work produced in ORC.

The exhaust gas outlet temperature of the ORC stays quite the same during the operation time around 340K for all scenarios. This exhaust gas leaving the ORC evaporator was of insufficient quality to run the absorption chiller system to have combined generation of excess power in ORC and cooling in absorption chiller (integration of SOFC-ORC-AC), so, two different scenarios were considered: SOFC-ORC and SOFC-AC. In SOFC-AC integration the system would meet dynamic cooling demands by sending the exhaust gas of SOFC goes through an absorption chiller to meet the cooling demand. Otherwise, in SOFC-ORC integration system would produce excess power by sending the exhaust gas of SOFC goes through the ORC. In both scenarios (SOFC-ORC and SOFC-AC) the energy of exhaust gas after ORC or absorption chiller is sufficient to produce hot water.

In terms of comparison between workday and weekend day, the average SOFC efficiency is 45% for the work day simulated and 46% for weekend day simulated. Efficiency is higher for weekend day because at weekend day most of the time the demand is lower than design power and the system is working mostly at part load which means that the system is operating at lower current density where over potential losses are lower. The average exhaust mass flow rate is 1.26kg/s and 1.17kg/s for the weekend day scenario. The average exhaust gas temperature is 599K and 594K for workday and weekend day, respectively

The average ORC power output is 26.2kW and 25.6kW for workday and weekend day scenarios, respectively. The workday ORC power output is higher than the weekend day due to the availability of higher exhaust heat energy on the workday.

The absorption chiller was simulated based upon the lowest available temperature of one day; that temperature was held constant throughout the day giving a conservative estimate of the amount of cooling possible from the absorption chiller. The temperature is fixed at 278°C for workday and 272°C for weekend. The average cooling provided is 131kW for the workday and 121kW for the weekend day. The average COP stayed around 1.1 for both scenarios. The average exhaust gas temperature is 134°C for the workday and 128°C for the weekend day.

6.2. Conclusions

- **Highly dynamic residential demand can be well followed by the dynamic SOFC model.**

  To commercialize dynamic SOFC systems for application in real world, it is necessary not only to develop an accurate model which takes into account the physical behavior of a real system, but also to consider simulating real load profile. The developed model for SOFC system uses the real residential dynamic loads as an input to determine the system operating parameters such that the SOFC generated power follows the demand profile. Results show that the SOFC system can follow highly dynamic demands quite accurately with small deviations from the demand profile due to the auxiliary electricity consumption in balance of plant component.

- **Large-scale SOFC systems can be integrated with ORC and AC to produce extra power and cooling.**

  Results from SOFC model show that quality of exhaust gas leaving large scale SOFC systems operating dynamically, is sufficient to be used as a heat source for bottoming cycles e.g. ORC and AC. In this study, results show that the energy of exhaust gas of a 400kW SOFC is sufficient to run 25kW ORC system and producing an average of 125kW cooling. For small scale SOFC, it's not cost effective to have ORC bottoming cycle.

- **Future dynamic integrated SOFC-ORC-AC systems may well support clean power generation for Residential application.**

  It was found that an integrated SOFC-ORC-AC is a good option for future residential applications in terms of system performance and overall efficiency. By using the exhaust of SOFC as a heat source for the ORC, seven present more power was produced through the ORC. Also, cooling demand of residential complex was supplied by integrating with AC system. This combined system is a good match for the purpose of zero net energy building and renewable power generation due to the ability of producing both electricity and cooling simultaneously as well as the ability to be run by renewable sourced fuels.

6.3. Recommendations

The first recommendation is to dynamically model a hydrogen separation unit to be able to evaluate producing hydrogen in addition to cooling and extra power in the system. Pure hydrogen gas can also be generated in this system as an energy co-product through using the tri-generation concept of lower fuel utilization followed by hydrogen separation from the anode off-gas.

Hydrogen as an energy carrier can be stored for later use, or as fuel for transportation use in a fuel cell electric vehicle.

The second recommendation is related to modification of dynamic modeling of the system to make it capable of providing more insights into the physics, chemistry and electrochemistry of the components. One recommendation is to design more accurate control system for the SOFC system. Also, calculations related to heat-loss to the environment due to the high temperatures in the stack could be added to the model to make a more accurate system model for the SOFC. Another recommendation is to use a moving boundary model for simulating the dynamics of the condenser and evaporator of the ORC, instead of using a bulk model. Also, designing a control system for the ORC to control the power output, pressures and the superheat temperature could be considered. The absorption chiller model should be modified to produce cooling by getting both dynamic exhaust gas temperature and dynamic mass flow rate instead of fixing the temperature constant.

An important consideration for the validity of these system configurations are the economics of building and operating them. Future research should be considered to quantify the total capital costs along with operating and maintenance costs of such a system. The results of such an analysis are essential in order to characterize the viability of realizing these systems. Ultimately, a comparison of the above systems with comparable state-of-the-art systems would need to be completed in order to create a clear picture of the economic viability of this system.

Another consideration that is becoming increasingly important is the environmental impact of the system. Not only are emissions over the lifetime of the system important, but also the energy and materials required for its entire life cycle. A life cycle analysis on the environmental impacts of the system will help determine whether the system is capable of providing an improvement to the environment in a significant fashion compared to comparable state-of-the-art systems.

The last recommendation would be to verify the ORC system with experimental results. It would be valuable to connect two commercially available SOFC and ORC systems into an integrated system and to experimentally run the system for various dynamic load profiles to compare the experimental results with those from the simulation model.

Appendix A

Leibniz's rule for differentiation of integrals with time varying limits:

$$\frac{d}{dt}\int_{z_1}^{z_2} f(z,t)\,dz = f(z_2,t)\frac{dz_2}{dt} - f(z_1,t)\frac{dz_1}{dt} + \int_{z_1}^{z_2}\frac{\partial f(z,t)}{\partial t}\,dz \qquad \text{(A-1)}$$

Appendix B

B.1. Mass Conservation at Working Fluid Side:

The general differential mass balance is:

$$\frac{\partial \rho}{\partial t} + \nabla.(\rho \vec{v}) = 0 \tag{B-1}$$

$$\dot{m} = \rho A_{cs} v \tag{B-2}$$

In equations (B-1and B-2) ρ is the working fluid density, $\vec{v}$ is the working fluid velocity and A_{cs} is the cross sectional area of a tube in which working fluid flows.

By multiplying A_{cs} in to equation (B-1) and considering equation (B-2), equation (B-3) can be obtained as follow:

$$\frac{\partial(\rho A_{cs})}{\partial t} + \frac{\partial(\dot{m})}{\partial z} = 0 \tag{B-3}$$

Integrating from $z = 0$ to $z = L_c$ (condenser tube length), which are corresponding to the inlet and outlet boundaries respectively:

$$\int_0^{L_c} \frac{\partial(\rho A_{cs})}{\partial t} dz + \int_0^{L_c} \frac{\partial(\dot{m})}{\partial z} dz = 0 \tag{B-4}$$

Assuming a constant cross sectional area and applying Leibniz rule equation to the first term (see Appendix A) results in equation (B-5).

$$A_{cs} \frac{d}{dt} \int_0^{L_c} \rho \, dz + (\dot{m}_{out} - \dot{m}_{in}) = 0 \tag{B-5}$$

In equation (B-5) the first term on the left hand side describes the rate of working fluid mass change. The second and third terms are the mass flows through the outlet and inlet boundaries respectively.

Assuming an average density for working fluid and integrating the first term results in:

$$A_{cs}\frac{d}{dt}(\bar{\rho}L_c) + (\dot{m}_{out} - \dot{m}_{in}) = 0 \rightarrow$$
$$A_{cs}\dot{\bar{\rho}}L_c + (\dot{m}_{out} - \dot{m}_{in}) = 0 \quad \text{(B-6)}$$

The thermodynamic properties are calculated from (p, h) in the present analysis, where h is the average enthalpy. The choice of *p* as one of the state variables is obvious, due to the assumption of no pressure loss. Temperature and pressure cannot be selected as independents variable because in two phase flow they are dependent to each other. The second variable should be either internal energy or enthalpy. In fact (p, h) is better for control volume problems. The average enthalpy $\bar{h}$ is defined as:

$$\bar{h} = \frac{(h_{in} + h_{out})}{2} \quad \text{(B-7)}$$

In equation (B-7) h_{in} and h_{out} are working fluid inlet and outlet enthalpy respectively.

The working fluid mean density is approximated by $\bar{\rho} = \rho(P, \bar{h})$ and the working fluid mean temperature is calculated from the same states as $\bar{T}_r = T(P, \bar{h})$.

In equation (B-6), $\frac{d\bar{\rho}}{dt}$ is calculated using the chain rule:

$$A_{cs}L_c\left[\left(\frac{\partial\bar{\rho}}{\partial P}\Big|_{\bar{h}}\right)\frac{dP}{dt} + \left(\frac{\partial\bar{\rho}}{\partial\bar{h}}\Big|_{P}\right)\frac{d\bar{h}}{dt}\right] + (\dot{m}_{out} - \dot{m}_{in}) = 0 \rightarrow$$
$$\left[A_{cs}L_c\left(\frac{\partial\bar{\rho}}{\partial P}\Big|_{\bar{h}}\right)\right]\dot{\bar{P}} + \left[A_{cs}L_c\left(\frac{\partial\bar{\rho}}{\partial\bar{h}}\Big|_{P}\right)\right]\dot{\bar{h}} + (\dot{m}_{out} - \dot{m}_{in}) = 0 \quad \text{(B-8)}$$

B.2. Energy Conservation Equation at Working Fluid Side

The general differential energy balance can be obtained:

$$\frac{\partial(\rho A_{cs}h - A_{cs}P)}{\partial t} + \frac{\partial(\dot{m}h)}{\partial z} = p_i\alpha_i(T_w - \bar{T}_r) \quad \text{(B-9)}$$

In equation (B-9) p_i is the inner cross sectional perimeter of a tube in which working fluid flows, α_i is convection heat transfer coefficient between working fluid and tube and T_w is the condenser's tube wall temperature.

Integrating from $z = 0$ to $z = L_c$ (condenser tube length):

$$\int_0^{L_c} \frac{\partial(\rho A_{cs} h)}{\partial t} dz - \int_0^{L_c} \frac{\partial(A_{cs} P)}{\partial t} dz + \int_0^{L_c} \frac{\partial(\dot{m} h)}{\partial z} dz = \int_0^{L_c} p_i \alpha_i (T_w - \bar{T}_r) dz \tag{B-10}$$

Applying Leibniz's rule (see Appendix A) on the equation (B-10) first term and integrating other terms based on a constant cross sectional area and a constant heat transfer coefficient along the tube:

$$\begin{aligned} &A_{cs}\left[\frac{d}{dt}\int_0^{L_c} \rho h dz\right] - A_{cs}\int_0^{L_c} \frac{\partial(P)}{\partial t} dz + \int_0^{L_c} \frac{\partial(\dot{m} h)}{\partial z} dz = \int_0^{L_c} p_i \alpha_i (T_w - \bar{T}_r) dz \rightarrow \\ &A_{cs}\left[\frac{d}{dt}\int_0^{L_c} \rho h dz\right] - A_{cs} L_c \dot{P} + (\dot{m}_{out} h_{out} - \dot{m}_{in} h_{in}) = L_c p_i \alpha_i (T_w - \bar{T}_r) \end{aligned} \tag{B-11}$$

In equation (B-11), the first term is the rate of change of enthalpy in the control volume, the second term is a consequence of using enthalpy and not internal energy in the first term. The third and fourth terms account for the convective enthalpy through the boundaries, and the last term is the heat flow from the wall.

Assuming that working fluid mean enthalpy is $\bar{h} = \frac{(h_{in} + h_{out})}{2}$, working fluid mean density is $\bar{\rho} = \rho(P, \bar{h})$ and working fluid mean temperature is $\bar{T_r} = T(P, \bar{h})$ and integrating the first term of equation (B-11), it can be obtained:

$$\begin{aligned} &A_{cs} L_c \left[\frac{d}{dt}(\bar{\rho}\bar{h} L)\right] - A_{cs} L_c \dot{P} + (\dot{m}_{out} h_{out} - \dot{m}_{in} h_{in}) = L_c p_i \alpha_i (T_w - \bar{T}_r) \rightarrow \\ &A_{cs} L_c \left[\dot{\bar{\rho}}\bar{h} + \dot{\bar{h}}\bar{\rho}\right] - A_{cs} L_c \dot{P} + (\dot{m}_{out} h_{out} - \dot{m}_{in} h_{in}) = L_c p_i \alpha_i (T_w - \bar{T}_r) \rightarrow \end{aligned} \tag{B-12}$$

$$A_{cs}L_c\left[\left[\left(\frac{\partial\bar{\rho}}{\partial P}\Big|_{\bar{h}}\right)\frac{dP}{dt}+\left(\frac{\partial\bar{\rho}}{\partial\bar{h}}\Big|_{P}\right)\frac{d\bar{h}}{dt}\right]\bar{h}+\dot{\bar{h}}\bar{\rho}\right]-A_{cs}L_c\dot{P}+(\dot{m}_{out}h_{out}-\dot{m}_{in}h_{in})$$

$$=L_cp_i\alpha_i(T_w-\bar{T}_r)\rightarrow$$

$$A_{cs}L_c\left[\left[\left(\frac{\partial\bar{\rho}}{\partial P}\Big|_{\bar{h}}\right)\dot{P}+\left(\frac{\partial\bar{\rho}}{\partial\bar{h}}\Big|_{P}\right)\dot{\bar{h}}\right]\bar{h}+\dot{\bar{h}}\bar{\rho}\right]-A_{cs}L_c\dot{P}+(\dot{m}_{out}h_{out}-\dot{m}_{in}h_{in})$$

$$=L_cp_i\alpha_i(T_w-\bar{T}_r)\rightarrow$$

$$A_{cs}L_c\left[\left(\frac{\partial\bar{\rho}}{\partial P}\Big|_{\bar{h}}\right)\bar{h}-1\right]\dot{P}+A_{cs}L_c\left[\left(\frac{\partial\bar{\rho}}{\partial\bar{h}}\Big|_{P}\right)\bar{h}+\bar{\rho}\right]\dot{\bar{h}}+(\dot{m}_{out}h_{out}-\dot{m}_{in}h_{in})=$$

$$L_cp_i\alpha_i(T_w-\bar{T}_r)$$

B.3. Energy Conservation at Wall Side

The energy balance for the wall region is derived using a control volume analysis similar to the energy balance analysis for the flow region. A simplified differential energy balance for the wall is given in equation (1-40):

$$C_{p_w}\rho_wA_w\frac{\partial T_w}{\partial t}=p_i\alpha_i(\bar{T}_r-T_w)+p_o\alpha_o(\bar{T}_a-T_w) \tag{B-13}$$

In equation (B-13), C_{p_w} is specific heat capacity of tube wall, ρ_w is density of tube wall, A_w is the annulus cross sectional area of tube wall, p_o is the outer cross sectional perimeter of a tube in which working fluid flows and α_o is convection heat transfer coefficient between exterior air stream and tube wall.

Integrating from $z=0$ to $z=L_c$ (condenser tube length):

$$\int_0^{L_c}C_{p_w}\rho_wA_w\frac{\partial T_w}{\partial t}dz=\int_0^{L_c}p_i\alpha_i(\bar{T}_r-T_w)dz+\int_0^{L_c}p_o\alpha_o(\bar{T}_a-T_w)dz\rightarrow$$

$$C_{p_w}\rho_wA_wL_c\frac{\partial T_w}{\partial t}=L_cp_i\alpha_i(\bar{T}_r-T_w)+L_cp_o\alpha_o(\bar{T}_a-T_w)\rightarrow \tag{B-14}$$

$$C_{p_w}\rho_w A_w \frac{\partial T_w}{\partial t} = p_i\alpha_i(\bar{T}_r - T_w) + p_o\alpha_o(\bar{T}_a - T_w)$$

In equation (B-14), the left hand side term accounts for the rate of change in internal energy. The right hand side terms account for the heat transfer from the inside and the outside of the wall.

Reference

[1] Energy Information Administration. International Energy Outlook 2009.

[2] U.S. Environmental Protection Agency. Inventory of U.S. Greenhouse Gas Emissions and Sinks: 1990–2007. 2009.

[3] Meyer L, Tsatsaronis G, Buchgeister J, Schebek L. Exergo-environmental analysis for evaluation of the environmental impact of energy conversion systems. Energy 2009; 34:75-89.

[4] F. Pavley and F. Nunez, California Assembly Bill No. 32-Global Warming Solutions Act of 2006, vol. 5, no. 32. State of California, 2006, pp. 38500–38599.

[5] International Energy Agency. Combined Heat and Power: Evaluating the Benefits of Greater Global Investment. 2008.

[6] Tom K. Combined heating and power and emissions trading: options for policy makers. International Energy Agency, July 2008.

[7] Wu, D. W., and R. Z. Wang. "Combined cooling, heating and power: a review." progress in energy and combustion science 32.5 (2006): 459-495.

[8] Singhal SC, Kendall K. High temperature solid oxide fuel cells: fundamentals design and applications. Oxford: Elsevier; 2003.

[9] Larminie, James, Andrew Dicks, and Maurice S. McDonald. Fuel cell systems explained. Vol. 2. Chichester, UK: J. Wiley, 2003.

[10] Laosiripojana, Navadol, et al. "Reviews on solid oxide fuel cell technology." Engineering Journal 13.1 (2009).

[11] Singhal SC. Advances in solid oxide fuel cell technology. Solid State Ionics 2000; 135:305–13.

[12] Stambouli A. Boudghene, Traversa E. Solid oxide fuel cells (SOFCs): a review of an environmentally clean and efficient source of energy. Renewable and Sustainable Energy Reviews 2002; 6:433–55.

[13] Wachsman, Eric D, Singhal, Subhash C. Solid Oxide Fuel Cell Commercialization, Research, and Challenges, the Electrochemical Society Interface, Fall 2009.

[14] Salim, R. I., et al. "Modeling and Temperature Analysis of the Nexa 1.2 kW Fuel Cell System." Journal of Fuel Cell Science and Technology 12.6 (2015): 061006.

[15] Quoilin, Sylvain, Vincent Lemort, and Jean Lebrun. "Experimental study and modeling of an Organic Rankine Cycle using scroll expander." *Applied energy* 87.4 (2010): 1260-1268.

[16] Quoilin, Sylvain. Sustainable energy conversion through the use of organic Rankine cycles for waste heat recovery and solar applications. Diss. University of Liège, Liège, Belgium, 2011.

[17] S. M. Martz, "Modeling and integration of the installation of a combined cooling, heat, and power system with high temperature fuel cell and absorption chiller," 2011.

[18] Saito M, Yoshida H, Iwamoto Y, Ueda A. An analysis of a micro cogeneration system composed of solid oxide fuel cell, micro-turbine, and h_2o/libr absorption refrigerator. Journal of Thermal Science and Technology 2007; 2(2):168–179.

[19] Chan SH, Ho HK, Tian Y. modeling of simple hybrid solid oxide fuel cell and gas turbine power plant. J Power Sources 2002; 109:111-20.

[20] Yi, Yaofan, Ashok D. Rao, Jacob Brouwer, and G. Scott Samuelsen. "Analysis and optimization of a solid oxide fuel cell and intercooled gas turbine (SOFC–ICGT) hybrid cycle." Journal of Power Sources 132, no. 1 (2004): 77-85.

[21] Zhang XW, Li J, Li GJ, Feng ZP. Cycle analysis of an integrated solid oxide fuel cell and recuperative gas turbine with an air reheating system. J Power Sources 2007; 164:752-60.

[22] Burbank W, Witmer D, Holcomb F. Model of a novel pressurized solid oxide fuel cell gas turbine hybrid engine. J Power Sources 2009; 193:656-64.

[23] Haseli Y, Dincer I, Naterer GF. Thermodynamic modeling of a gas turbine cycle combined with a solid oxide fuel cell. Int J Hydrogen Energy 2008; 33:5811-22.

[24] Bao C, Shi YX, Li C, Cai NS, Su QQ. Multi-level simulation platform of SOFC-GT hybrid generation system. Int J Hydrogen Energy 2010; 35:2894-9.

[25] Bao C, Cai NS, Croiset E. A multi-level simulation platform of natural gas internal reforming solid oxide fuel cellegas turbine hybrid generation system e part II. Balancing units model library and system simulation. J Power Sources 2011; 196:8424-34.

[26] Hirschenhofer JH, Stauler DB, Engleman RR, Klett MG. Fuel cell handbook.4th ed. Parsons Corporation Reading P.A. for U.S. Department of Energy; 1998.

[27] F.Mueller, R.Gaynor, A.F. Auld, J.Brouwer, F.jabbari, G.S. Samuelsen.Synergistic integration of a gas turbine and solid oxide fuel cell for improved transient capability. Journal of Power Sources 176 (1) (2008) 229-239.

[28] Akkaya AV, Sahin B. A study on performance of solid oxide fuel cell-organic Rankine cycle combined system. Int J Energy Res 2009; 33:553-64.

[29] Al-Sulaiman FA, Dincer I, Hamdullahpur F. Energy analysis of a trigeneration plant based on solid oxide fuel cell and organic Rankine cycle. Int J Hydrogen Energy 2010; 35: 5104-13.

[30] Ghirardo F, Santin M, Traverso A, Massardo A. Heat recovery options for onboard fuel cell systems. Int J Hydrogen Energy 2011; 36:8134-42.

[31] Al-Sulaiman FA, Hamdullahpur F, Dincer I. Efficiency and environmental impact assessments of a trigeneration plant using sofc and orc. Proceedings of the Global Conference on Global Warming, Istanbul, Turkey, 2009; 11.

[32] Al-SulaimanFahad A, Dincer Ibrahim, HamdullahpurFeridun. Exergy analysis of an integrated solid oxide fuel cell and organic Rankine cycle for cooling, heating and power production. J Power Sour 2010; 195(8):2346–54.

[33] Al-Sulaiman Fahad A, Hamdullahpur Feridun, Dincer Ibrahim. Greenhouse gas emission and exergy assessments of an integrated organic Rankine cycle with a biomass combustor for combined cooling, heating, and power production.Appl Thermal Eng 2011; 31(4):439–46.

[34] Pierobon L, Rokni M, Larsen U, Haglind F. Thermodynamic analysis of an integrated gasification solid oxide fuel cell plant combined with an organic Rankine cycle. Renew Energy 2013; 60:226-34.

[35] Al-Sulaiman Fahad A, Hamdullahpur Feridun, Dincer Ibrahim. Performance comparison of three trigeneration systems using organic Rankine cycles. Energy 2011; 36:5741–54.

[36] Margalef, Pere, and Scott Samuelsen. "Integration of a molten carbonate fuel cell with a direct exhaust absorption chiller." Journal of Power Sources 195.17 (2010): 5674-5685.M.

[37] Silveira, José Luz, Elisangela Martins Leal, and Luiz F. Ragonha. "Analysis of a molten carbonate fuel cell: cogeneration to produce electricity and cold water." Energy 26.10 (2001): 891-904.

[38] Leal, Elisângela M., and José Luz Silveira. "Study of fuel cell co-generation systems applied to a dairy industry." Journal of Power Sources 106.1 (2002): 102-108.

[39] Elmer, Theo, et al. "Assessment of a novel solid oxide fuel cell tri-generation system for building applications." Energy Conversion and Management 124 (2016): 29-41.

[40] Liu, Y., and K. C. Leong. "Numerical study of an internal-reforming solid oxide fuel cell and adsorption chiller co-generation system." Journal of power sources 159.1 (2006): 501-508.

[41] Yu, Zeting, et al. "Analysis of total energy system based on solid oxide fuel cell for combined cooling and power applications." International Journal of Hydrogen Energy 35.7 (2010): 2703-2707.

[42] Zink, Florian, Yixin Lu, and Laura Schaefer. "A solid oxide fuel cell system for buildings." Energy Conversion and Management 48.3 (2007): 809-818.

[43] Yu, Zeting, Jitian Han, and Xianqi Cao. "Investigation on performance of an integrated solid oxide fuel cell and absorption chiller tri-generation system." International Journal of Hydrogen Energy 36.19 (2011): 12561-12573.

[44] Brouwer, Jack, and R. Bekemohammadi. "Tri-Generation of Hydrogen, Heat and Power From a High Temperature Fuel Cell." AIChE Annual Meeting. 2012.

[45] Becker WL, Braun RJ, Penev N, Melaina M. Design and techno-economic performance analysis of a 1 MW solid oxide fuel cell polygeneration system for combined production of heat, hydrogen, and power. Journal of Power Sources 2012; 200:34-44.

[46] Perdikaris N, Panopoulos KD, Hofmann PH, Spyrakis S, Kakaras E. Design and exergetic analysis of a novel carbon free tri-generation system for hydrogen, power and heat production from natural gas,

based on combined solid oxide fuel and electrolyzer cells. Journal of Hydrogen Energy 2010; 35:2446-56.

[47] Margalef P. On the polygeneration of electricity, heat and hydrogen with high temperature fuel cells, PhD dissertation, University of California, Irvine. 2010.

[48] McLarty, Dustin Fogle. Fuel cell gas turbine hybrid design, control, and performance. University of California, Irvine, 2010.

[49] McLarty, Dustin, Jack Brouwer, and Scott Samuelsen. "A spatially resolved physical model for transient system analysis of high temperature fuel cells." international journal of hydrogen energy 38.19 (2013): 7935-7946.

[50] Rasmussen, Bryan P., and Andrew G. Alleyne. Dynamic modeling and advanced control of air conditioning and refrigeration systems. Air Conditioning and Refrigeration Center. College of Engineering. University of Illinois at Urbana-Champaign., 2006.

[51] Shengjun, Zhang, Wang Huaixin, and Guo Tao. "Performance comparison and parametric optimization of subcritical Organic Rankine Cycle (ORC) and transcritical power cycle system for low-temperature geothermal power generation." *Applied energy* 88.8 (2011): 2740-2754.

[52] Cavallini, A., et al. "Heat transfer and pressure drop during condensation of refrigerants inside horizontal enhanced tubes." International Journal of Refrigeration 23.1 (2000): 4-25.

[53] Zhang, Jianhua, et al. "Modeling and constrained multivariable predictive control for ORC (Organic Rankine Cycle) based waste heat energy conversion systems." Energy 66 (2014): 128-138.

[54] Zhang, Jianhua, et al. "Dynamic modeling and multivariable control of organic Rankine cycles in waste heat utilizing processes." Computers & Mathematics with Applications 64.5 (2012): 908-921.

[55] Quoilin, Sylvain, et al. "Dynamic modeling and optimal control strategy of waste heat recovery Organic Rankine Cycles." Applied energy 88.6 (2011): 2183-2190.

[56] Yazaki Energy, Inc. Dual-Exhaust and Gas Fired Chiller-Heater KE Model [Product Technical Specifications]. 2003.

[57] SOLIDpower “Installation Requirements: BlueGEN” http://www.SOLIDpower.com/fileadmin/user_upload/pages/Logos_materialien/SOLIDpower_BlueGEN_Brochure_UK_web.pdf

[58] SOLIDpower “Installation Requirements: Engen-2500” http://www.SOLIDpower.com/wp-content/uploads/2014/03/Installation_requirements_Engen2500_eng.pdf